

## REPORT DOCUMENTATION PAGE

Form Approved  
OMB No. 0704-0188

Public reporting burden for this collection of information is estimated to average 1 hour per response, including the time for reviewing instructions, searching existing data sources, gathering and maintaining the data needed, and completing and reviewing the collection of information. Send comments regarding this burden estimate or any other aspect of this collection of information, including suggestions for reducing this burden, to Washington Headquarters Services, Directorate for Information Operations and Reports, 1215 Jefferson Davis Highway, Suite 1204, Arlington, VA 22202-4302, and to the Office of Management and Budget, Paperwork Reduction Project (0704-0188), Washington, DC 20503.

1. AGENCY USE ONLY (Leave blank)	2. REPORT DATE	3. REPORT TYPE AND DATES COVERED Penal 1 Oct 91 - 31 Dec 94	
4. TITLE AND SUBTITLE "Picosecond Phase Conjugation: New Applications, Devices, and Materials".		5. FUNDING NUMBERS <u>F49620-92-5-0022</u>	
6. AUTHOR(S) Professor Jack Feinberg		61102F 2301/AS	
7. PERFORMING ORGANIZATION NAME(S) AND ADDRESS(ES) University of Southern California Department of Physics and Astronomy Los Angeles, CA 90089-0484		8. PERFORMING ORGANIZATION REPORT NUMBER AFOSR-IR-93-0238	
9. SPONSORING/MONITORING AGENCY NAME(S) AND ADDRESS(ES) Dr. Howard Schlossberg AFOSR/NE 110 Duncan Avenue Suite B115 Bolling AFB DC 20332-0001		10. SPONSORING/MONITORING AGENCY REPORT NUMBER <u>F49620-92-5-0022</u>	
11. SUPPLEMENTARY NOTES		DTIC SELECTED APR 14 1995 G	
12a. DISTRIBUTION/AVAILABILITY STATEMENT Approved for Public Release: Distribution Unlimited		12b. DISTRIBUTION CODE	
13. ABSTRACT (Maximum 200 words) In this project we investigated four main areas: 1) Temporal shaping of picosecond laser pulses using beam coupling in a photorefractive crystal. We showed both theoretically and experimentally that one can add or subtract picosecond light pulses onto existing light pulses to create arbitrary temporal waveforms. 2) The Physics of the photorefractive effect in barium titanate crystals. We showed that photovoltaic currents play an important role in the formation of photorefractive gratings in barium titanate. We also derived a theory to explain the curved beam paths observed in photorefractive phase conjugators. 3) Frequency doubling of infrared light in glass. We proved decisively that second-harmonic generation in optically prepared glass is caused by a dc electric field imprisoned in the glass. We mapped the spatial profile of this dc field to a resolution of one micron. 4) Injecting diode laser arrays using phase conjugation. We demonstrated that injecting a broad-area diode laser with light causes the laser array to emit a spatially and spectrally narrow output beam. We use a double phase conjugator to guide light from an injecting laser into the lasing regions of the laser array.			
14. SUBJECT TERMS DTIC QUALITY INSPECTED 5 Laser, Picosecond, Frequency Doubling, Injection Locking			15. NUMBER OF PAGES
			16. PRICE CODE
17. SECURITY CLASSIFICATION OF REPORT Unclassified	18. SECURITY CLASSIFICATION OF THIS PAGE Unclassified	19. SECURITY CLASSIFICATION OF ABSTRACT Unclassified	20. LIMITATION OF ABSTRACT U

## Final Report

submitted to the  
Air Force Office of Scientific Research  
Bolling AFB, Building 410,  
Washington, D.C. 20332-6448

ATTN.: Dr. Howard Schlossberg

**19950413 069**

1) Date submitted: March 15, 1995

2) Title: PICOSECOND PHASE CONJUGATION: NEW APPLICATIONS,  
DEVICES, AND MATERIALS

3) Principal Investigator: JACK FEINBERG  
Office: (213) 740-1134, Fax: (213) 740-6653

4) Time period covered: October 1, 1991 - December 31, 1994.

5) Institution Name: University of Southern California, Los Angeles, CA 90089-  
0484

6) Federal agency identifying award number: F49620-92-J-0022

PICOSECOND PHASE CONJUGATION:  
NEW APPLICATIONS, DEVICES, AND MATERIALS

Jack Feinberg  
Department of Physics  
University of Southern California  
Los Angeles, California 90089-0484  
(213) 740-1134

Accession For	
NTIS	CRA&I <input checked="" type="checkbox"/>
DTIC	TAB <input type="checkbox"/>
Unannounced <input type="checkbox"/>	
Justification _____	
By _____	
Distribution / _____	
Availability Codes	
Dist	Avail and/or Special
A-1	

**A) Summary of Overall Progress:**

**FIRST YEAR:**

In the first year of this AFOSR grant we submitted 6 papers. These projects span a wide variety of topics, as described below:

1) X. S. Yao and J. Feinberg, "Temporal shaping of optical pulses using beam coupling in a photorefractive crystal," *Optics Letters* 18, 622-624 (1993).

This is one of three papers describing our successful experiments to use a photorefractive crystal to alter the temporal shape of picosecond light pulses. Such shaped pulses may be used for launching solitons into long-range communication fibers. Under our previous AFOSR contract, we published a theory predicting that pulses can be shaped in time by mixing them with other pulses in a photorefractive crystal. Our present experiments demonstrate such temporal beam shaping. We selectively carve holes or add peaks onto the pedestal of a picosecond pulse, where the holes and the peaks have a temporal width of a few picoseconds, as shown in Figure 1 below.

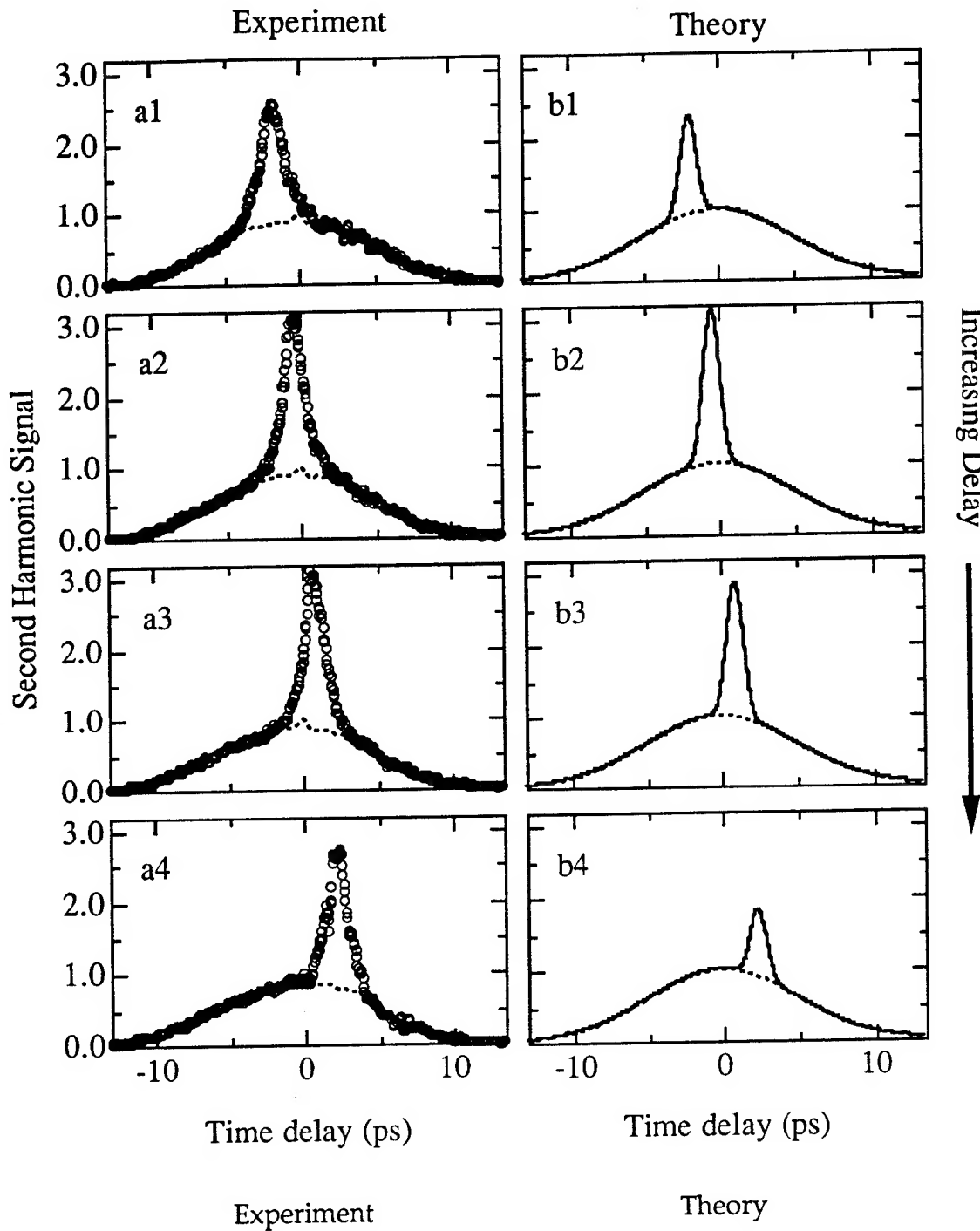


Figure 1: A picosecond peak is "grafted" onto a longer pulse using two-wave mixing in a photorefractive crystal of barium titanate. Left plots (a1-a4): measured shapes; Right plots (b1-b4): predicted shapes. The relative delay between the two interacting light beams is changed between each of the four rows, and this shifts the position of the peak by a few picoseconds.

2) X. S. Yao and J. Feinberg, "Photorefractive pulse coupling in the frequency domain," *Optics Letters* 18, 104-106 (1993).

In our previous AFOSR contract, we presented a detailed theory predicting how pulses can be shaped in time by mixing them with other pulses in a photorefractive crystal. The experiments on temporally shaped pulses shown in Figure 1 above show qualitative agreement between theory and experiment, but a more accurate comparison can be performed in the frequency domain. When optical pulses couple in a photorefractive crystal their frequency spectra is altered. This affects their temporal shape, but sometimes only in subtle ways that are difficult to measure. Here we measure the frequency spectrum of light pulses directly, both before and after coupling in a photorefractive crystal, and compare our measurements with theory. Figure 2 shows that the agreement between experiment and theory is quite good. (The roll-off of the data in the wings is caused by the finite size of the photorefractive crystal).

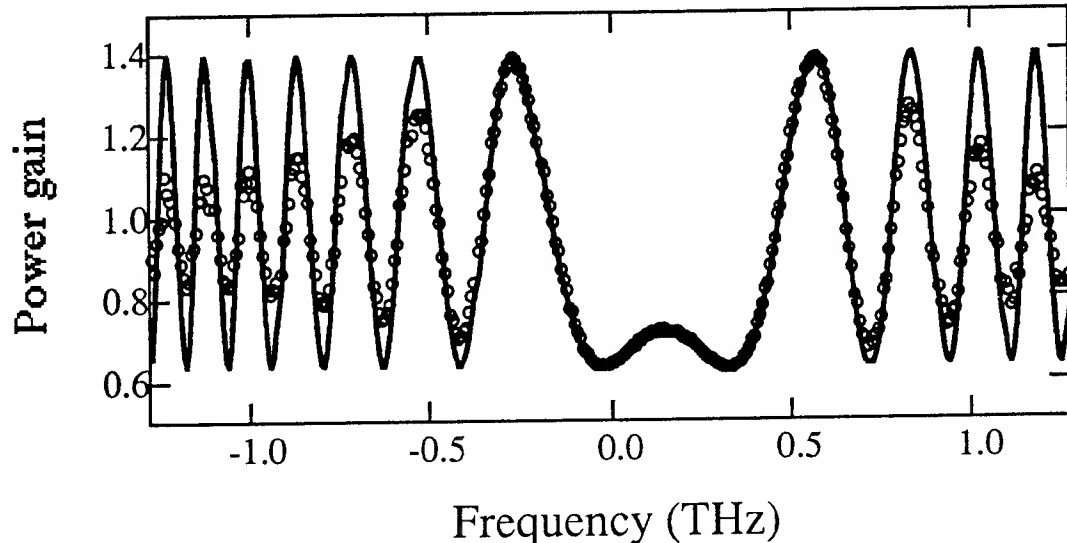


Figure 2: Gain vs. frequency for a picosecond light pulse that has coupled with another picosecond light pulse in a photorefractive crystal.

Our experiments also show that the light diffracted from a photorefractive grating suffers a phase shift that depends quadratically on the delay time between the pulses interacting in the photorefractive crystal. This result is a direct confirmation that the average power gain of the input light beam is

proportional to the magnitude squared of the second-order field correlation function, as we had previously predicted. A rival theory, which predicted that the average power gain of the signal beam is proportional to the fourth-order field correlation function, cannot provide any phase information and so cannot predict the observed dependence of the phase shift on the relative delay time.

- 3) X. S. Yao and J. Feinberg, "Simple in-line method to measure the dispersion of an optical system," *Applied Physics Letters* 62, 811-813 (1993).

In the course of our work on shaping pulses, we invented a simple and accurate method to measure the dispersion of an arbitrary optical system. Such measurements are critical for designing and aligning femtosecond laser systems. Our method uses the final laser beam itself to diagnose the optical system, and thereby ensures that the final beam traverses the exact same path as the diagnostic beam. We interfere the light beam with a separate light beam inside a spectrometer. The resulting spectrum yields the quadratic and cubic dispersion terms of the optical system. We demonstrate this technique on an optical system formed by a pair of gratings.

- 4) V. V. Eliseev, A. A. Zozulya, G. D. Bacher, and J. Feinberg, "Self-bending of light beams in photorefractive phase conjugators," *Journal of the Optical Society of America-B* 9, 398-404 (1992).

This paper describes the details of self-pumped phase conjugation in photorefractive crystals. A single beam input into a photorefractive crystal will produce a host of new, stimulated beams, including a phase-conjugate beam. In a continuation of work begun in our previous AFOSR contract, we show why these stimulated light beams appear to follow *curved* paths inside the crystal. These apparently curved paths are formed by a series of straight-line segments, with beams propagating in both directions along these segments. These line segments arise from the amplification of scattered light inside the crystal. As they form, these line segments create new interaction regions which generate new line segments, thereby making the final light path appear curved. We present a detailed theory of this effect, including predictions for the coupling strength required for these curved light paths to form. We also show

photographic evidence that the curved beam paths are composed of a series of straight-line segments.

- 5) R. S. Cudney, R. M. Pierce, G. D. Bacher, D. Mahgerefteh, and J. Feinberg, "Intensity dependence of the photogalvanic effect in barium titanate," *Journal of the Optical Society of America-B* 9, 1704-1713 (1992).

Even a uniform beam of light causes charges to migrate in a preferred direction in some photorefractive crystals, such as barium titanate. This charge migration causes a measurable current, called the photogalvanic current. This paper explains in detail how the photogalvanic current alters the gain available for light beams in photorefractive crystals. Studying the photogalvanic current is somewhat complicated due to our discovery that in addition to the expected uniform current in the crystal, there is also a spatially varying current in the crystal caused by spatial variations of the incident light pattern. This spatially-varying current competes, with and, in general, dominates the spatially-uniform current. This spatially-varying term has been ignored in the past, and has led previous researchers to predict the wrong sign for the photogalvanic current. In fact, it is the spatially-varying current that controls charge transport in barium titanate crystals.

- 6) V. Dominic and J. Feinberg, "Growth rate of second-harmonic generation in glass," *Optics Letters* 17, 1761-1763 (1992).

One can obtain blue light from existing laser diodes by frequency doubling their infrared light beam in an inorganic crystal, such as lithium triborate. However, such frequency-doubling crystals are expensive. Wouldn't it be nice to replace the expensive crystal by an inexpensive glass fiber? Because the core of an optical fiber is macroscopically centrosymmetric, two-wave sum frequency generation (and in particular second-harmonic generation) is not expected to occur in an optical fiber. However, in 1987 Österberg and Margulis reported rather efficient (5%) second-harmonic generation of 1.064  $\mu\text{m}$  light inside a germanium-doped optical fiber that had been illuminated by intense infrared light for many hours.<sup>1</sup> Stolen and Tom<sup>2</sup> showed that by injecting both

infrared and green light into the fiber, the preparation time of the fiber could be shortened from many hours to just a few minutes.

In this paper we study the growth rate of the light-induced second-order nonlinearity in germanium-doped optical fiber preforms. The purpose of this work is to understand the physical mechanism responsible for the light-induced changes in the glass. We seed the glass with both infrared light and green light (Nd:YAG and doubled Nd:YAG) to create the second-order nonlinearity, and measure its formation rate while varying the intensity of either the fundamental or second-harmonic seeding beams. We find that the formation rate varies as a power law of the intensities, but with an exponent larger than predicted by recent models.<sup>3</sup> In particular, we find that the rate coefficient increases with the intensity of the infrared seeding beam as  $I_{\omega}^{8-12}$ , and with the intensity of the green seeding beams as  $I_{2\omega}^{2.5-3.5}$ . Our results imply that the defect responsible for the optical nonlinearity of the glass is 4 infrared photons (4 eV) deep, and that the nonlinearity is due to the competition of different multiphoton ionization pathways.

- [1] U. Österberg and W. Margulis, Opt. Lett. **11**, 516 (1986); Opt. Lett. **12**, 57 (1987).
- [2] R. H. Stolen and H. W. K. Tom, Opt. Lett. **12**, 585 (1987).
- [3] E. M. Dianov, P. G. Kazansky, and D. Yu Stepanov, Sov. J. Quantum Electron. **19**, 575 (1989); E. M. Dianov, P. G. Kazansky, and D. Yu Stepanov, Sov. Lightwave Commun. **1**, 247 (1991).

#### SECOND YEAR:

In the second year of this project we continued our work on picosecond phase conjugation and branched out into two new areas: phase conjugation of laser diodes and the physics of second harmonic generation in glass. It was a productive year; we submitted or published additional papers as follows:

- 7) V. Dominic and J. Feinberg, "Spatial shape of the dc electric field produced by intense light in glass," Optics Letters **18**, 784-786 (1993).

The photorefractive effect can occur not only in crystals (such as BaTiO<sub>3</sub>) but in glasses as well. A light beam and its second harmonic can create a semi-permanent dc electric field inside glass. This dc electric field, of magnitude  $10^{+6}$  V/m, is responsible for the production of second-harmonic light in the glass. In

this paper we map out the transverse spatial shape of this photoinduced dc field inside a bulk sample of germanium-doped fused silica glass.

There has been a considerable effort since 1987 to understand how an apparently centrosymmetric material like glass can act as a frequency doubler. We now know that the incident light creates a dc electric field inside the glass, breaking its inversion symmetry. This photoinduced dc electric field acts through the symmetry-allowed third-order susceptibility  $\bar{\chi}^{(3)}$  of the glass to produce the required second-order nonlinearity  $\bar{\chi}^{(2)}$ ,

$$\bar{\chi}^{(2)}(-2\omega; \omega, \omega) = 3 \bar{\chi}^{(3)}(-2\omega; \omega, \omega, 0) \cdot \bar{E}_{dc} \quad (1)$$

where  $\bar{E}_{dc}$  is the photoinduced dc electric field.

Here we report a measurement of the transverse spatial shape of the photoinduced dc electric field. We use the polarization properties of  $\bar{\chi}^{(2)}$  to carefully map the spatial shape of the dc electric field  $\bar{E}_{dc}$ . We guess a final charge distribution:

$$\rho(x, y) = (\rho_0 y / w) \exp[-(x^2 + y^2)/w^2], \quad (2)$$

which is the vertical derivative of a cylindrically symmetric Gaussian function of width  $w$ . The charge density  $\rho_0$  is unspecified. We choose the parameter  $w=4.5$   $\mu\text{m}$  to match our data. Figure 1 shows the dc electric field  $\bar{E}_{dc}$  caused by such a charge distribution. Figure 2 shows transverse maps of the predicted and measured signal strengths using the proposed field shape. Although the finite size of our probing limits our resolution, our spatial map clearly shows the symmetry of the dc field. This dc field shape can predict the results of six different experiments. In all of these experiments we find excellent agreement between our predictions and our measurements.

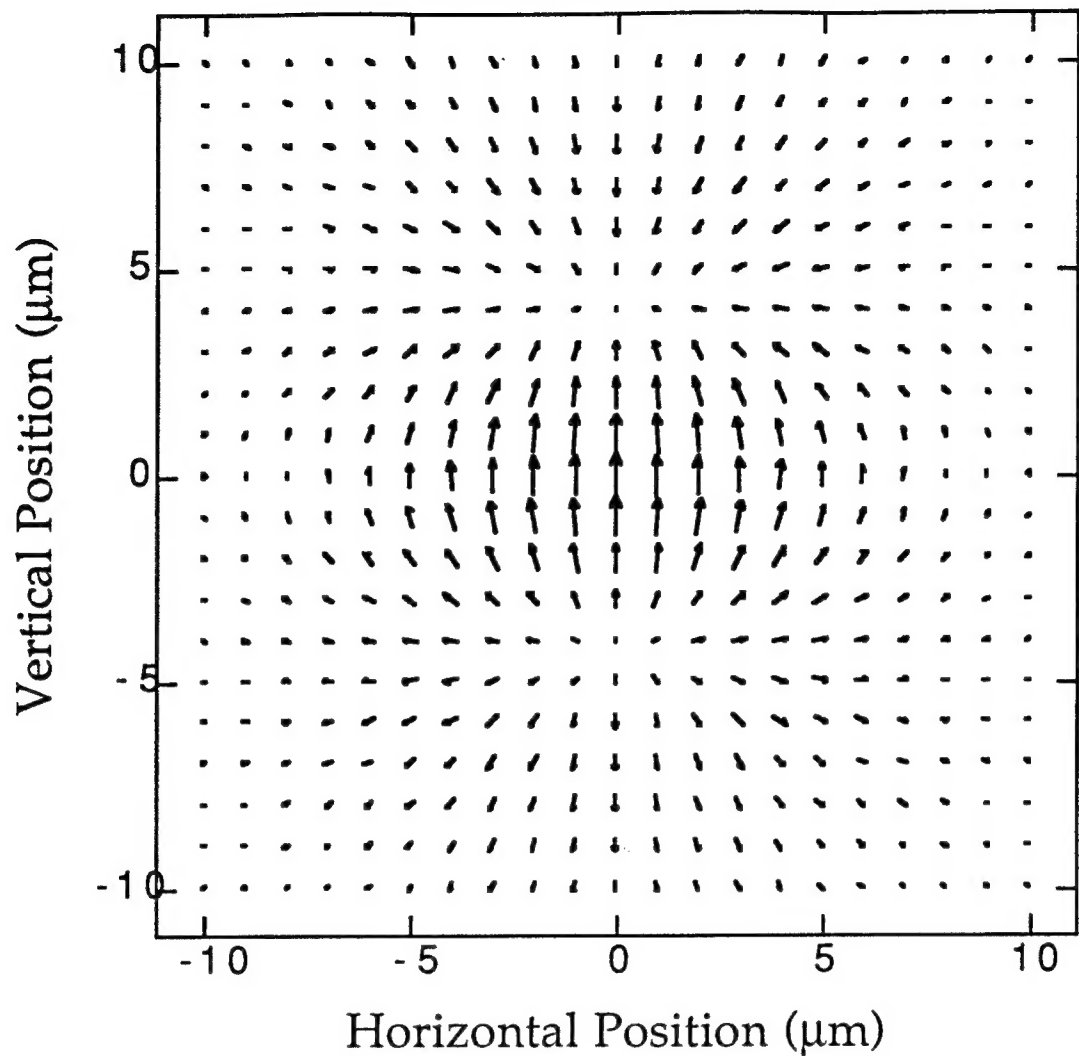


Figure 3. The dc electric field produced from the charge distribution given by Eq. (2) above. With this dc field shape we successfully predicted the results of six experiments.

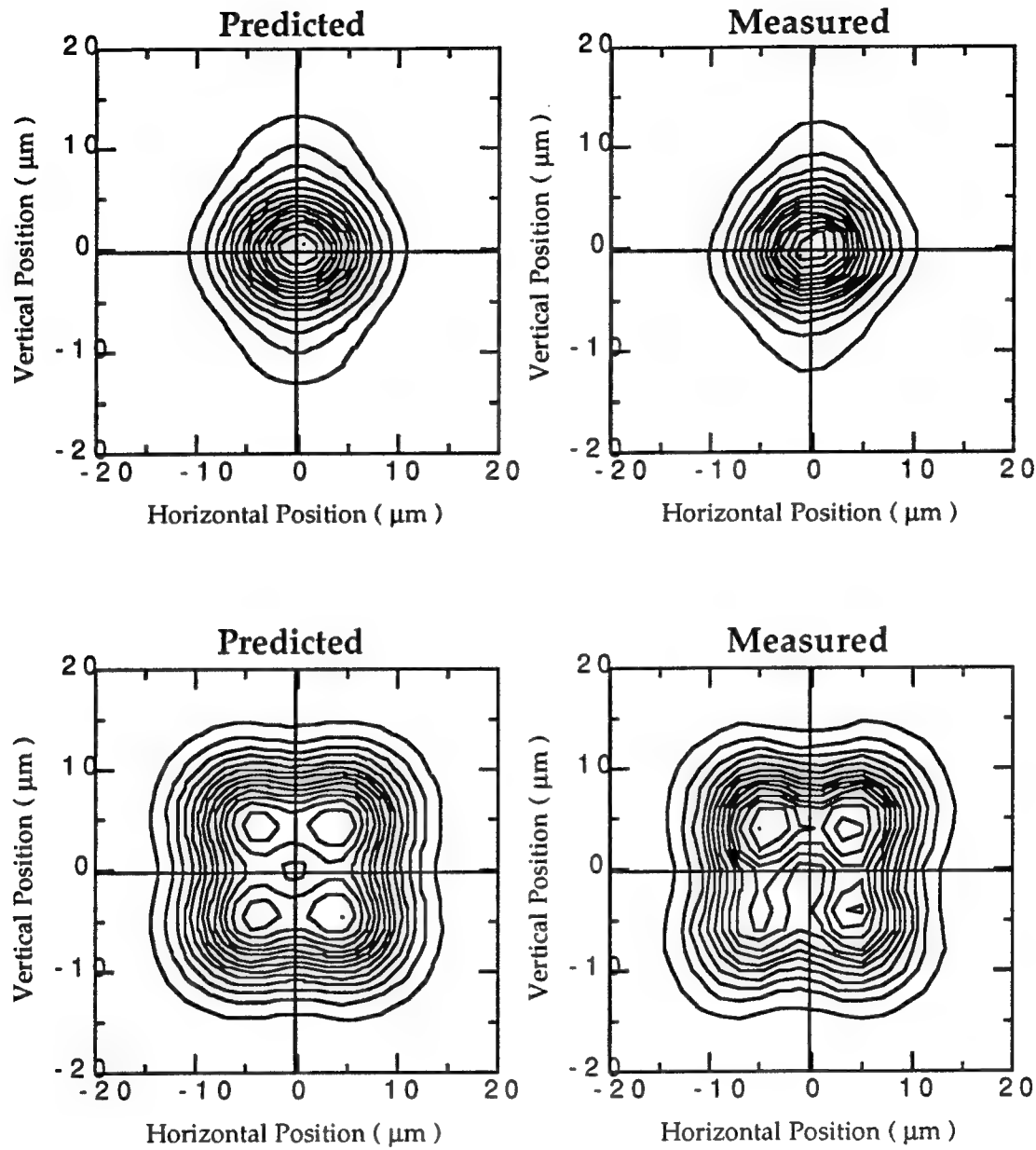


Figure 4. Comparison between the predicted and the measured dependence of the signal on the probe beam position. The glass sample was a Ge-doped optical fiber preform. The probe and the analyzer polarizations are oriented either vertically (top) or horizontally (bottom).

8) S. MacCormack and J. Feinberg, "High-brightness output from a laser-diode array coupled to a phase-conjugating mirror," *Optics Letters* 18, 211-213 (1993).

Although laser diode arrays can produce impressive amounts of optical power, they usually simultaneously operate on many transverse modes, which makes their far-field pattern a mess. Their poor beam quality makes laser diode arrays ill suited for many applications, such as launching intense light into single-mode waveguides or pumping mini- laser systems.

Here we couple a laser diode array to an external, photorefractive phase conjugator, and thereby force the array to operate on a single transverse mode. Even while running close to its maximum rated output power, this device now puts out a near diffraction-limited beam.

We obtain single-lobed, near diffraction limited output from a 20-element laser diode array coupled to an apertured, photorefractive phase conjugator. At low driving currents the output beam is diffraction limited and contains 75% of the total output power emanating from the array, as shown in Figure 3 below. At high driving current a  $1.5 \times$  diffraction-limited lobe contains 490 mW, or 54% of the output power.

Subsequent analysis of the frequency spectrum of the locked array revealed a rich assortment of array modes. This result implies that previous theories on the behavior of lasers locked to external phase conjugators are incorrect. In fact, the correct description of the device now appears to be that of a Fabry Perot cavity with gain that is injected by external light. The injected beam rattles back and forth between the two mirrors, extracting gain, and then exits at an angle opposite to the injecting beam.

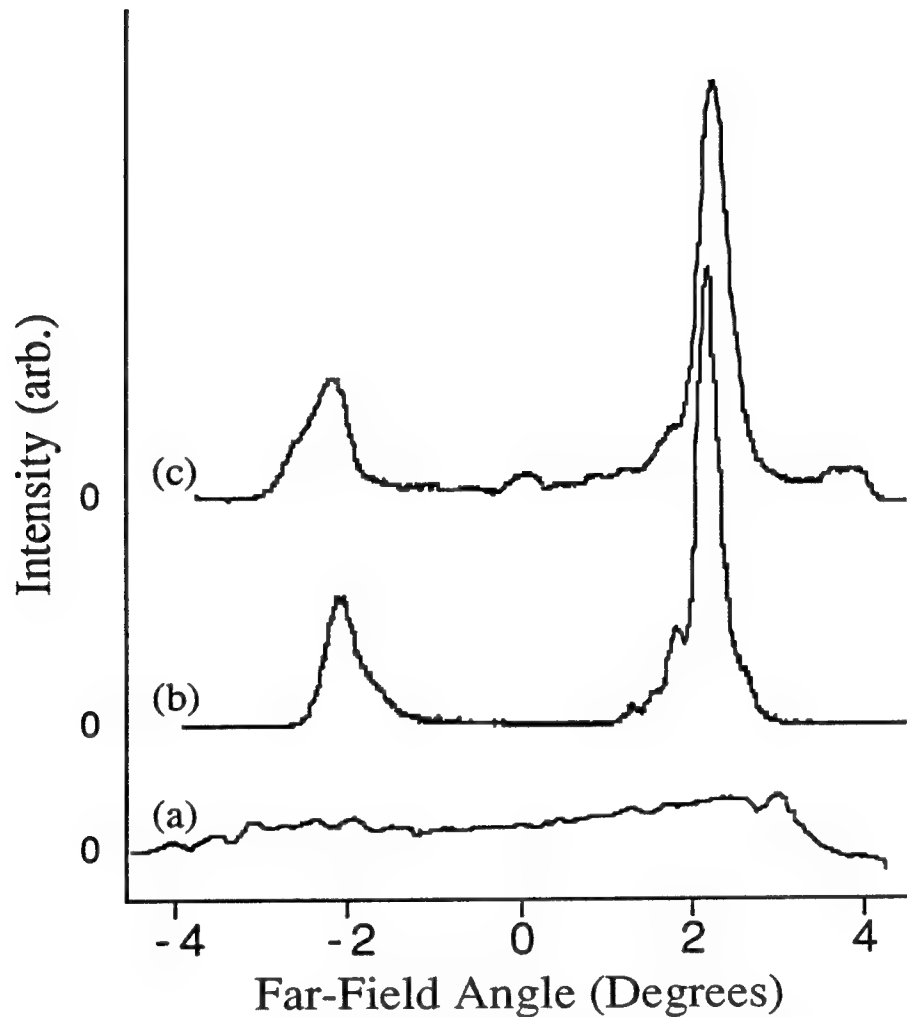


Figure 5. Output of a laser diode array while (a) free running, or (b) with phase-conjugate feedback, or (c) with phase-conjugate feedback and higher array driving current. (Curves (b) and (c) are displaced vertically for clarity.) When the laser is free running its output beam spews out over a wide angular range, as seen in trace (a). However, when the conjugator feeds back a small portion of the laser's light, the output beam narrows to make the sharp output peak seen at  $+2^\circ$ . The smaller peak at  $-2^\circ$  is the light going into the phase conjugator.

### THIRD YEAR

We continued our investigations into frequency doubling in glass. We also pursued our experiments to obtain high-power coherent laser diode arrays, as shown in the following papers.

- 9) V. Dominic and J. Feinberg, "Light-induced second-harmonic generation in glass via multiphoton ionization," *Physical Review Letters* 71, 3446-3449 (1993).

In our previous paper in JOSA-B we showed a new method for mapping out the dc electric field created in glass when the glass is illuminated by intense light at both green and infrared wavelengths. In this paper we improved our spatial resolution and so provide exquisitely detailed maps of the dc field locked inside the glass. We map the two components of this electric field separately, and so build a complete spatial map of the dc field. An example of the data is shown in Fig. 6 below.

We also calculate the probability that the incident light beams can eject electrons from their trapped sites in the glass under a variety of input light polarizations. We then performed these experiments and show that these calculated photogalvanic current can explain the various measured dc field patterns.

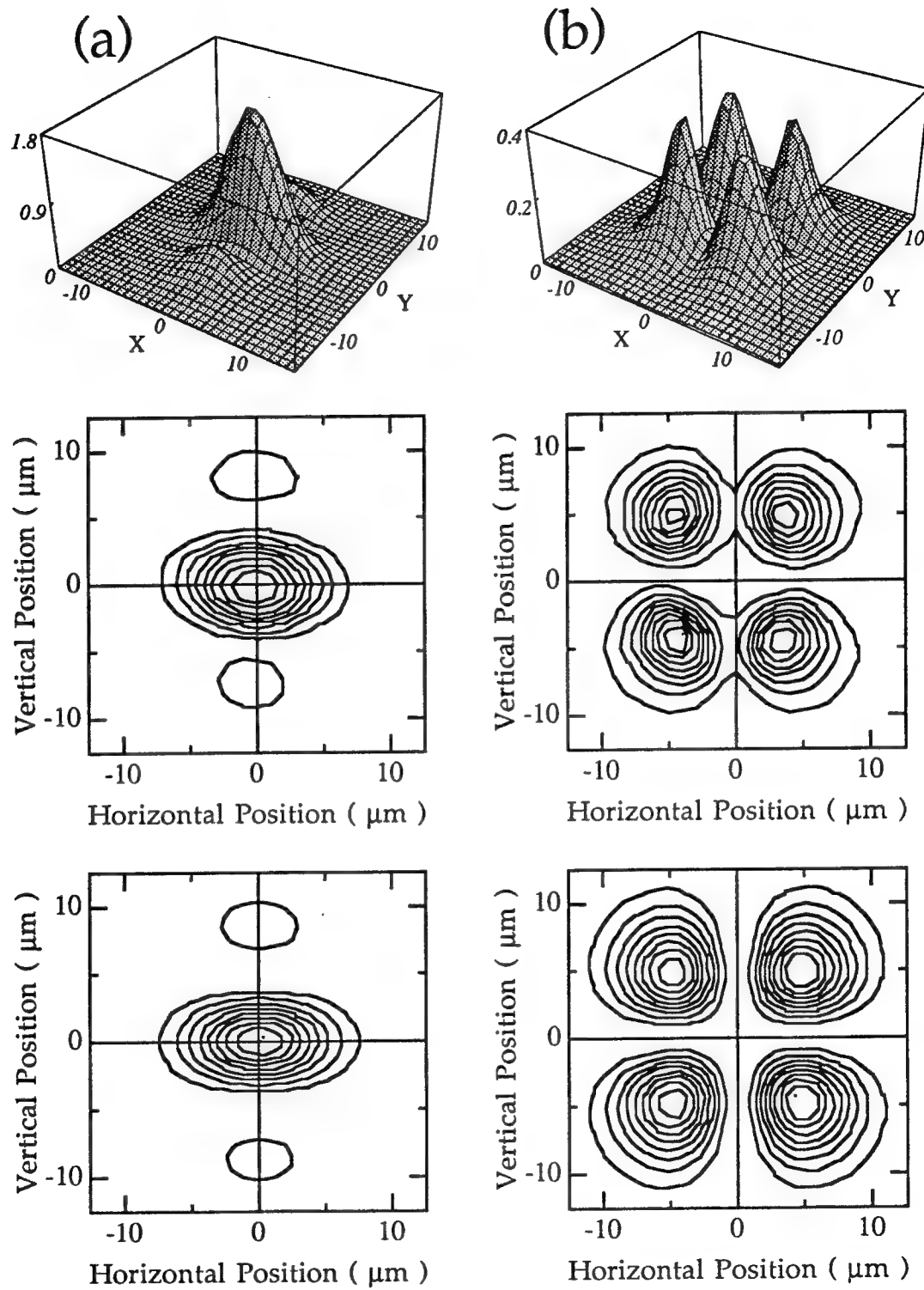


Figure 6. Strength of the second-harmonic signal versus transverse position. The top two rows are the experimental data displayed in two formats. The bottom row is calculated from a charge distribution that is the spatial derivative of a Gaussian along the  $y$  direction.

10) V. Dominic, Patrick Lambelet, and J. Feinberg, "Measurement of the phase of second-harmonic generation in SK5 glass," *Optics Letters* **20**, 444-446 (1995)

Here we measure the phase  $\theta$  between the green light that induces second-harmonic generation in glass and the green light produced by the glass itself. We find that the phase shift is  $90^\circ \pm 7^\circ$ . At first this seems a surprising result, because a small vector added in quadrature to an existing vector changes only the vector's phase but not its amplitude, to first order. However, as we will show in a subsequent publication, the finite time response of the glass enables the green light to grow in strength.

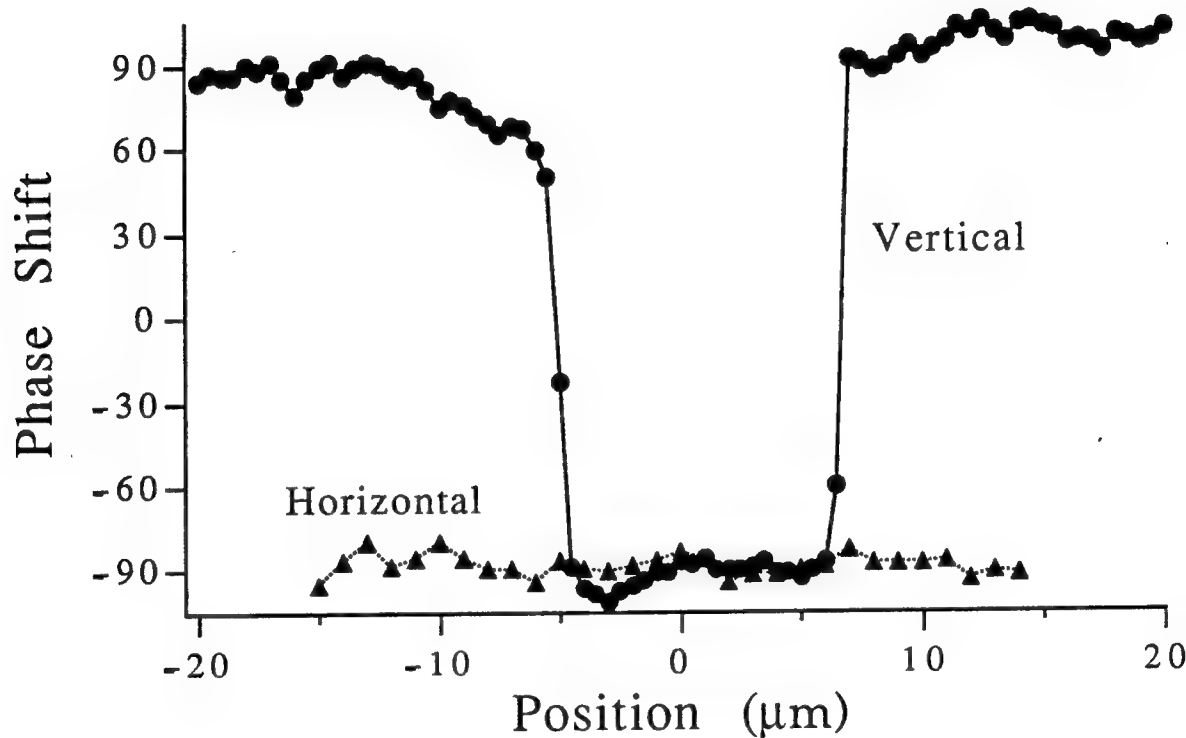


Figure 7. Measured phase shift  $\theta$  versus the probing beam position near the center (position = 0) of the seeded spot. For horizontal scans (dashed line) the phase shift is independent of the position. However, for vertical scans (solid line), the phase shift experiences  $180^\circ$  jumps on the outskirts of the seeding light beams, where the dc dipole electric field reverses sign.

In this paper we also show that the phase  $\theta$  of the generated green light undergoes an abrupt transition at the edges of the light-seeded regions of the glass sample, as seen in Fig. 6. This discontinuity is caused by the reversal in the direction of the dc electric dipole field at the top and bottom of the dipole field, as can be seen by inspecting the dc dipole field in Figure 3 above. This measurement confirms that there is indeed a dc electric field locked inside the glass, and lays to rest competing theories of second-harmonic generation in glass.

11) S. MacCormack and J. Feinberg, "Injection locking a laser-diode array with a phase-conjugate beam," *Optics Letters* **19**, 120-122 (1994).

We show that it is possible to make a broad-area laser emit a coherent and spatially clean light beam by injecting the laser with light from another semiconductor laser. The trick is to use a mutually-pumped phase conjugator to connect the two lasers. The conjugator automatically directs light from the injecting laser precisely to the lasing region of the slave laser. The slave laser then becomes single frequency and emits into a nearly diffraction limited beam. We are presently scaling up these injecting experiments to arrays of broad area lasers (laser bars) having substantially higher power.

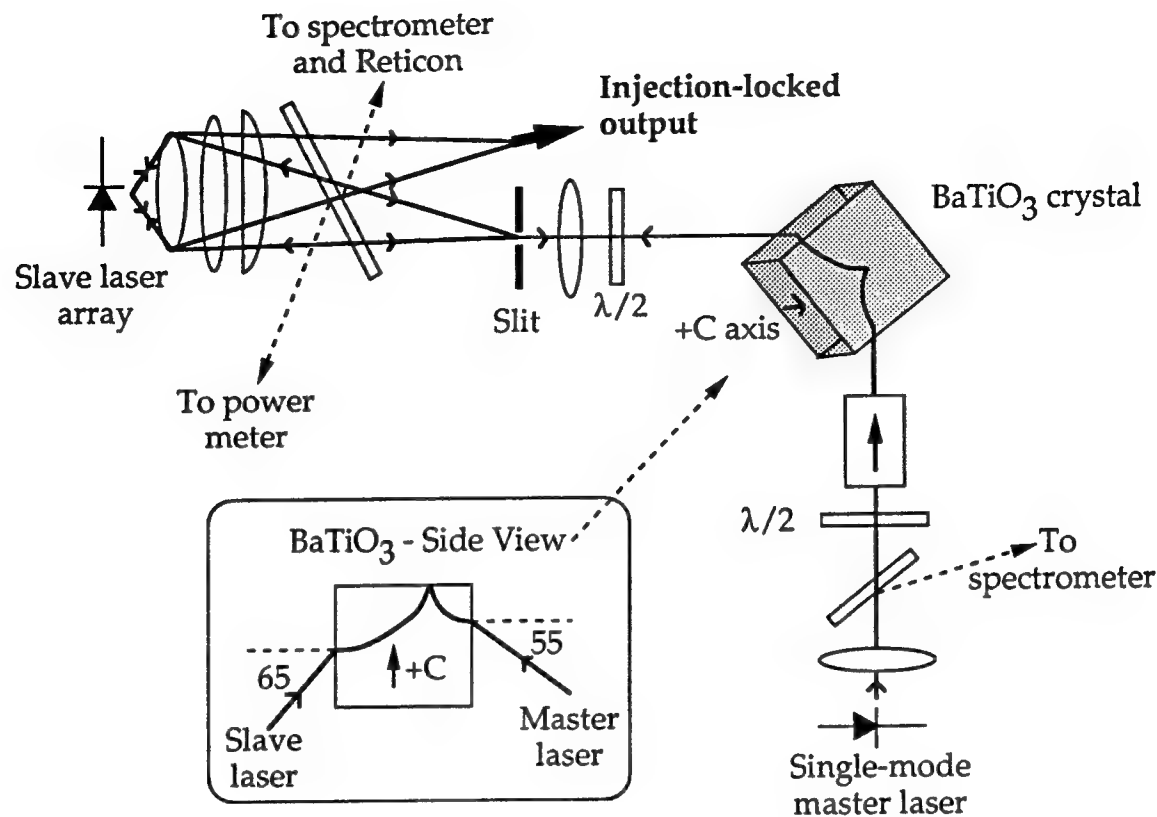


Figure 8. Optical set up for injecting light from a single-mode master laser into a slave laser array. The BaTiO<sub>3</sub> crystal acts as a mutually pumped phase conjugator to direct the injecting laser beam precisely into the lasing regions of the slave laser array.

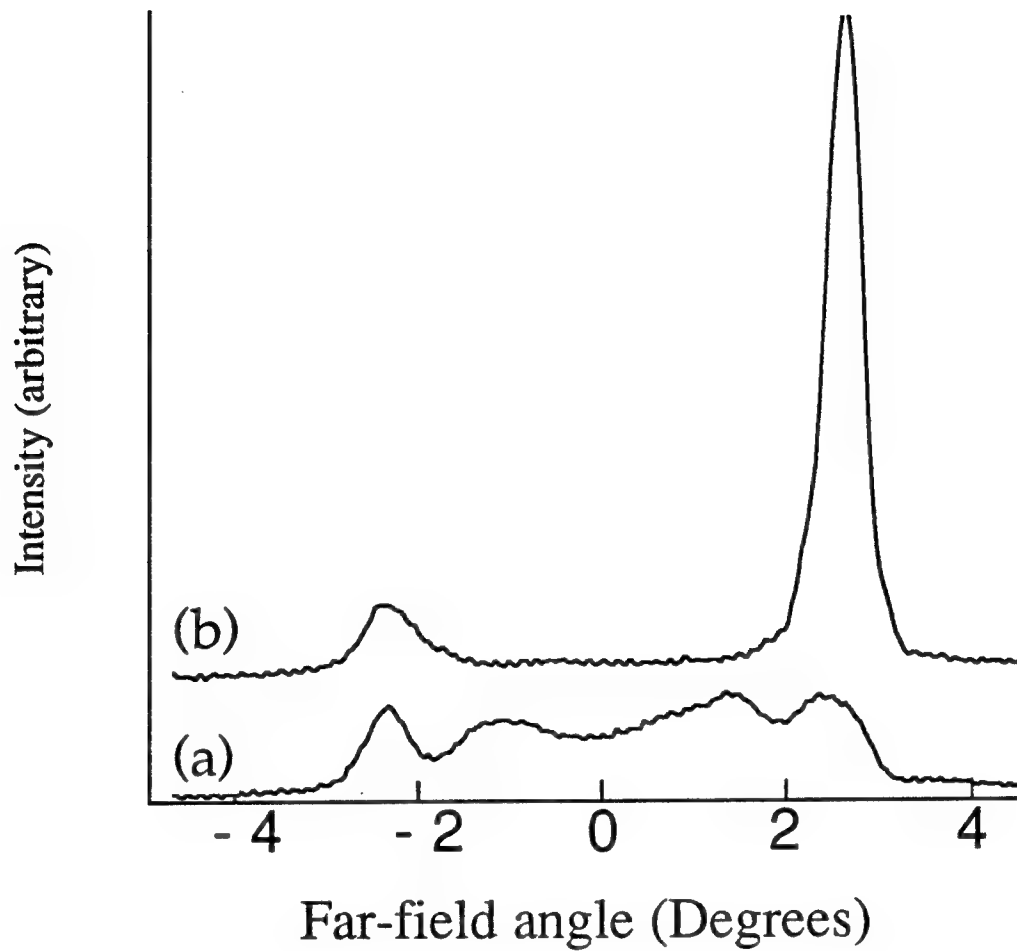


Figure 9. Far field light patterns from the slave laser. In trace (a) the slave laser is free running, and it emits a wide swath of light. In trace (b) the slave is injected with light from the master laser, and the slave laser now emits a narrow, intense output beam.

**C) Current Problems or Unusual Developments:**

None.

**D) Changes from Original Proposal:**

None.

# Injection locking a laser-diode array with a phase-conjugate beam

Stuart MacCormack and Jack Feinberg

Departments of Physics and Electrical Engineering, University of Southern California, Los Angeles, California 90089-0484

M. H. Garrett

Centre de Recherche en Optoélectroniques, Sandoz-Huningue S.A., Avenue de Bâle, Huningue 68330, France

Received July 16, 1993

We use a mutually pumped phase conjugator to guide the output beam of a single-mode laser diode into the active region of a high-power laser-diode array. This injected beam locks the frequency of the array, causing it to emit a single, 1.45 times diffraction-limited, continuous-wave output beam containing 85% of the array's total output power. Phase-conjugate injection dramatically improves the coupling into the laser array, so that less than a milliwatt of injected power is sufficient to lock all the array's 450-mW output to the frequency of the master laser.

Injecting light from a single-mode laser into a laser-diode array can narrow the array's output spectrum and produce a nearly diffraction-limited output beam.<sup>1</sup> Over a narrow range of wavelengths and injection angles, the laser array becomes a slave to the master laser's injecting beam; it simply becomes a waveguide with optical gain and amplifies the injected beam at the expense of the array's own free-running modes. However, this occurs only if the master laser beam's frequency, position, and incident angle are just right,<sup>2</sup> and these constraints place great demands on the master laser beam's frequency stability, shape, and alignment. Here we demonstrate an injection-locking scheme that overcomes these problems: we use a mutually pumped phase conjugator to aim the master laser beam precisely into the gain region of the laser array.

A mutually pumped phase conjugator couples two optical beams and directs each beam down the throat of the other.<sup>3,4</sup> The two incident light beams typically have slightly different frequencies and so are not coherent with each other. The conjugator transfers spatial and phase information from one beam to the other, so that the two beams leave the device as phase-conjugate replicas of each other. We use a photorefractive crystal of barium titanate as our mutually pumped phase conjugator. The ~1-s response time of this conjugator automatically adjusts to gradual changes in either the position or the angle of incidence of the two input beams. Using a mutually pumped phase conjugator to direct the laser beams eases the problem of beam alignment and shape by a factor of ~1000, from one of micrometers and millidegrees into one of millimeters and degrees.

Figure 1 shows our experimental setup. The slave laser is an off-the-shelf, 1-W laser-diode array (SDL 2462-P1) mounted on a temperature-controlled heat sink and operated at a wavelength of ~800 nm. We conservatively operate the laser at a current of 1.0 A (equal to 2.1 times the threshold current), where it produces a continuous-wave, free-running output power of 450 mW. (We operate the laser below its

maximum rated output power to suppress oscillation on its free-running modes. Alternatively, we could reduce the slave laser's output coupler reflectivity and thereby increase the self-oscillation threshold.) A high-numerical-aperture lens collects the horizontally polarized output beam and directs it toward a cylindrical and spherical lens pair. This lens combination generates a pseudo twin-lobed far-field pattern with a width of ~10 mm. One lobe is incident upon an adjustable slit placed in the far field. Light transmitted through the slit is weakly focused by a spherical lens into an approximately 1 mm × 1 mm spot on one *a* face of the BaTiO<sub>3</sub> crystal. Its external angle of incidence is 65° to the crystal face normal. Our blue-colored BaTiO<sub>3</sub> crystal (named Bleu) measures 6.1 mm × 6.6 mm × 5.9 mm and is mounted with its *c* axis in the vertical plane. (Blue BaTiO<sub>3</sub> has an enhanced photorefractive response at near-infrared wavelengths compared with the usual pale-

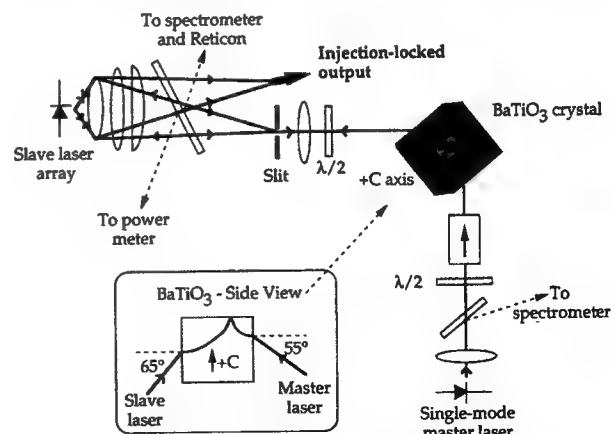


Fig. 1. Experimental setup. The combination of a Faraday polarizer and a  $\lambda/2$  plate isolates the single-mode master laser. The slit selects one lobe of the array slave laser. Both the master and slave laser beams enter the BaTiO<sub>3</sub> crystal and fan toward its top face. (The crystal's *+c* axis faces up, normal to the plane of this figure.) The inset shows a side view of the BaTiO<sub>3</sub> crystal and the bird-wing pattern made by the laser beams.

yellow  $\text{BaTiO}_3$ .<sup>5</sup>) We use a half-wave plate to make the array's output polarization parallel to its direction of spatial coherence, which is perpendicular to the plane of the laser gain region.<sup>6,7</sup>

The master laser is a 100-mW, temperature-tuned, single-mode laser (SDL 5412-H1). We temperature tune this master laser's frequency to lie anywhere within the slave laser's 2-nm-wide, free-running output spectrum. Its polarized output is collected by a high-numerical-aperture lens and directed through a half-wave plate and a Faraday isolator to make it an extraordinary ray at the barium titanate crystal. (The Faraday isolator prevents light from the slave laser from feeding back into the master laser and causing frequency instabilities. Good optical isolation is especially important here since a fraction of the array's output is converted into the phase-conjugate replica of the master laser's beam.) We direct ~8 mW of output from the master laser into the  $\text{BaTiO}_3$  crystal face opposite the  $a$  face entered by the slave laser and positioned closer to the crystal's positive  $c$  face than to the slave laser's input beam. This injected beam makes an external angle of 55° to the crystal face normal. We use asymmetric beam positions because the narrow-frequency, master laser beam fans more strongly in the crystal than does the broad-bandwidth, slave laser beam. We perform beam power, frequency, and shape measurements on reflections from optical flats placed in the paths of the master and slave laser beams. We analyze the optical beams' frequencies with a Spex 0.75-m double-grating spectrometer and a Newport SR-200 spectrum analyzer (finesse >10,000). We monitor the beams' shapes with a 512-element scanning linear photodiode array placed in the far field.

Within a few seconds after the master and the slave laser beams illuminate the crystal, the beams bend and join to form an asymmetric bird-wing mutually pumped phase conjugator.<sup>4</sup> The conjugator directs the master laser beam into the phase-conjugate replica of the slave laser beam. This injected beam now has the same spatial and phase profile as one of the preferred transverse array modes of the free-running array and so has the optimum angle and profile for injection locking the array.<sup>8</sup> Once the array is injection locked, the array switches to emit predominantly a single lobe that appears at an angle equal to but opposite that of the injected beam.

As shown in Fig. 2, this strong output lobe is accompanied by a weaker secondary lobe that continues to illuminate the bird-wing conjugator. These two lobes compete and reach a stable steady state. For example, if the power directed into the conjugator decreases as a result of greater locking efficiency, then the conjugator becomes less efficient. This decreases the power injected into the array, which in turn decreases the power directed into the output lobe, thereby restoring the equilibrium. We found that directing too much master laser power (>30 mW) into the conjugator can make the injection locking too efficient, so that all the array's output suddenly switches into the output lobe at the expense of the secondary lobe. With no light now coming from the

array to the conjugator, the conjugator turns off, and locking ceases.

Once the array is injection locked, the angular width of the output lobe changes according to the width of the far-field aperture. We adjust this aperture to optimize the power in the array's output lobe while still keeping its divergence near the 0.29° diffraction limit of the array's 200- $\mu\text{m}$ -wide emitting region. For example, with the adjustable aperture set to produce an output beam divergence of 1.5 times the diffraction limit, the output beam has an elliptical Gaussian profile and contains 85% of the array's total output (384 mW). The remaining output power is in the secondary lobe, with practically no emission outside these two locked lobes. When the array is locked, the angular position of the main lobe remains constant, even with small perturbations to the far-field aperture width, ambient temperature, or position of the master laser beam. The stability of the locked far-field lobe intensity is good. Over periods of hours, we measure peak-to-peak fluctuations of less than 10% in the main lobe intensity. These intensity fluctuations arise predominantly from the 20% fluctuations in the conjugator's transmissivity. We observe no steering of the far-field lobe with small changes in the master laser's drive current.

The free-running array lases on many longitudinal modes simultaneously. However, the injection-locked array operates only at the master laser's single wavelength. (Frequency pulling and changes in the far-field profile were previously observed for two arrays coupled by a mutually pumped phase conjugator.<sup>9</sup>) No other output frequencies are present to within the 20-dB sensitivity of our spectrometer. Figure 3 shows that the bandwidths of the master and slave laser outputs are identical to within the 750-MHz resolution of our spectrum analyzer. Overlapping the master and slave laser outputs on a CCD camera produces stable high-visibility interference fringes, implying that the two lasers are locked and coherent with each other. (We have shown previously that the bird-wing conjugator performs well even with mutually coherent input beams.<sup>10</sup>) In our experiments, we

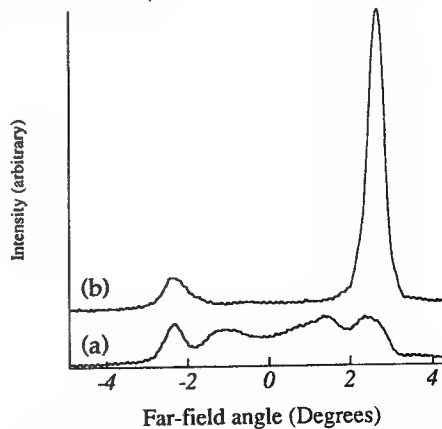


Fig. 2. Far-field spatial pattern of the diode array (a) when free running and (b) when injection locked. The FWHM of the main lobe in (b) is 0.38°, which is 1.45 times the diffraction limit (a Strehl ratio of 0.37). The total output power for each case is 450 mW.

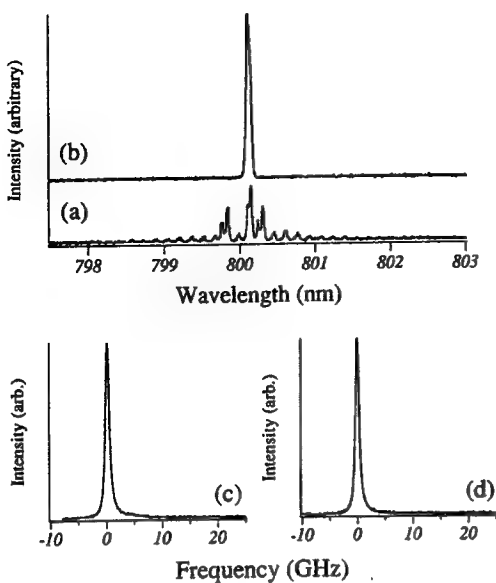


Fig. 3. Diode-array spectra measured with a 1.4-m spectrometer when (a) free running and (b) locked. Once the array is locked, (c) and (d) show the high-resolution spectra of the slave and master laser output beams, respectively; their frequency bandwidth is narrower than the 750-MHz resolution of our spectrum analyzer.

observe no contribution to the light injected into the array from any backscattering gratings in the  $\text{BaTiO}_3$  crystal.

Consider the injection-locking process as the amplification of a signal beam in a Fabry-Perot amplifier.<sup>11</sup> We can then judge the effectiveness of different geometries by comparing the values of their small-signal gain,  $G$ , defined as the ratio of the power contained in the locked lobe to the injected power, for operation in the unsaturated regime. For conventional injection-locking geometries,  $G$  typically ranges from 19 to 23 dB.<sup>12,13</sup> However, we are not operating in the unsaturated regime. As discussed above, increasing the power incident upon the crystal from the master laser does not necessarily increase the power injected into the array. Nevertheless, even when operating in a saturated regime, we obtain a locked output of  $>380$  mW for an injected signal of 0.50 mW, corresponding to a saturated gain of 29 dB. Below this injection level the spatial shape of the output lobe deteriorates.

In our experiments the small-signal gain  $G$  is large because our injected signal is the phase-conjugate replica of one of the natural modes of the slave laser array. Consequently, it is efficiently coupled into the slave laser waveguide and has an ideal overlap with the gain profile of the laser. This leads to efficient gain extraction and to saturation of the amplification even with small injected power. If we permit a somewhat degraded output beam shape and compute the locking efficiency using the total output power of the slave array (i.e., both the output and the secondary lobes), then we can boast of a frequency-locked output of 450 mW for an injected power of 0.27 mW, which corresponds to a gain of 32 dB.

At steady state our bird-wing conjugator typically transforms  $\sim 5\%$  of each incident beam into a phase-conjugator replica of the other beam. For example, in the setup shown in Fig. 1 the power from the master laser incident upon the  $\text{BaTiO}_3$  crystal was 8.2 mW, while the power deflected by the conjugator toward the slave laser was 0.50 mW, which gives a phase-conjugate transmission of 6%. A transmissivity as large as 35% has been observed for mutually pumped phase conjugators in the near infrared,<sup>14</sup> but we were unable to achieve such large values in our experiments.

We have shown that a phase-conjugate injection beam significantly improves the ease of alignment and the efficiency of locking a laser-diode array. The ability of a small injected power to lock a laser array becomes important for locking higher-power laser diodes or locking multiple laser arrays. In these cases, the success of injection locking will depend on the power available from the single-mode master laser. With conventional injection locking the currently available 100-mW single-mode lasers could lock a maximum of  $\sim 10$  W of slave laser output. However, with phase-conjugate injection locking the same 100-mW laser has the potential for locking slave laser arrays of as much as 100 W.

We gratefully acknowledge support by grant F49620-92-J-0022 from the U.S. Air Force Office of Scientific Research.

## References

1. L. Goldberg and J. F. Weller, *Appl. Phys. Lett.* **46**, 236 (1985).
2. M. K. Chun, L. Goldberg, and J. F. Weller, *Opt. Lett.* **14**, 272 (1989).
3. B. Fischer and S. Sternklar, *Appl. Phys. Lett.* **51**, 74 (1987).
4. M. D. Ewbank, *Opt. Lett.* **13**, 47 (1988).
5. G. W. Ross, P. Hribek, R. W. Eason, M. H. Garrett, and D. Rytz, in *Conference on Lasers and Electro-Optics*, Vol. 11 of 1993 OSA Technical Digest Series (Optical Society of America, Washington, D.C., 1993), paper CFC4.
6. S. MacCormack and J. Feinberg, *Opt. Lett.* **18**, 211 (1993).
7. M. Cronin-Golomb, Tufts University, Medford, Mass. 02155 (personal communication, 1991).
8. H. Adachihara, O. Hess, R. Indik, and J. V. Moloney, *J. Opt. Soc. Am. B* **10**, 496 (1993).
9. M. Segev, S. Weiss, and B. Fischer, *Appl. Phys. Lett.* **50**, 1397 (1987).
10. S. C. De La Cruz, S. MacCormack, and J. Feinberg, in *Conference on Lasers and Electro-Optics*, Vol. 11 of 1993 OSA Technical Digest Series (Optical Society of America, Washington, D.C., 1993), paper CThS54.
11. G. L. Abbas, S. Yang, V. W. S. Chan, and J. G. Fujimoto, *Opt. Lett.* **12**, 605 (1987).
12. L. Goldberg and J. F. Weller, *Appl. Phys. Lett.* **53**, 1900 (1988).
13. L. Goldberg and J. F. Weller, *Electron. Lett.* **22**, 858 (1986).
14. G. W. Ross and R. W. Eason, *Opt. Lett.* **18**, 571 (1993).

# Measurement of the phase of second-harmonic generation in SK5 glass

Vince Dominic,\* Patrick Lambelet, and Jack Feinberg

Departments of Physics and Electrical Engineering, University of Southern California,  
University Park, Los Angeles, California 90089-0484

Received September 16, 1994

Focusing an intense laser beam and its second harmonic into a SK5 glass slab transforms the glass into a frequency doubler. We present a new method to measure the optical phase between the second-harmonic beam that transformed the glass and the second-harmonic beam subsequently generated by the glass. We find this phase shift to be  $\Delta\theta = -90^\circ \pm 7^\circ$ . A spatial map of this phase confirms that the internal dc electric field locked inside the glass resembles a dipole electric field.

Frequency doubling in glass should be forbidden, because glass has macroscopic inversion symmetry. However, in 1986 Österberg and Margulis<sup>1</sup> observed frequency doubling in a glass optical fiber after illuminating the fiber with intense infrared light for several hours. A year later Stolen and Tom<sup>2</sup> showed that launching some frequency-doubled green light into a fiber along with the infrared light dramatically increased the speed of the process, from 10 h to 5 min. It is now understood that the incident fundamental and frequency-doubled light beams cause a dc electric field to build up in the glass and that this semipermanent dc electric field not only breaks the inversion symmetry of the glass but also permits periodic phase matching of the frequency-doubling process.<sup>3-5</sup>

Here we measure the relative phase shift  $\Delta\theta$  between the frequency-doubled green beam used to seed the glass and the frequency-doubled green beam generated inside the glass. Why is this phase shift worth measuring? Because it provides a check on the validity of current theories of second-harmonic generation in glass. Recent experiments<sup>6-8</sup> have measured these two green beams to be out of phase by  $90^\circ$ , which, at first glance, is precisely the wrong value for this process to be able to bootstrap up and grow in strength. (Adding a small vector at  $90^\circ$  to an existing vector only rotates the vector's direction but does not increase its magnitude.) We find that, in fact, the phase  $\Delta\theta$  is near  $-90^\circ$  in our Schott SK5 glass sample. However, even with  $\Delta\theta = -90^\circ$ , the seeding process's finite time response can permit exponential growth of the dc electric field with time.<sup>9-11</sup>

We present a new technique to measure the phase shift between the seeding and the glass-generated green light beams. Our technique is similar to the methods discussed in Refs. 6-8, except that, as shown in Fig. 1, we use three frequency-doubling elements to avoid perturbing the original seeding beam, namely: (i) a doubling crystal [lithium triborate (LBO)] located before the glass sample, which makes the original green seeding beam, (ii) the glass sample, which creates the green signal beam, and (iii) another doubling crystal [potassium titanyl phosphate (KTP)] located after the glass sample, which provides a green reference beam. In order to determine the relative phase of beams (i) and (ii), we

measure two separate interference patterns, namely, (a) that between beams (i) and (iii) and (b) that between beams (ii) and (iii). The phase shift  $\Delta\theta$  between the green seed (i) and the green signal (ii) is then obtained from the relative displacement of the two interference patterns (a) and (b).

Notice that, instead of attenuating the seeding green beam, we simply block it and replace it with the infrared seeding beam, which we then double in a KTP crystal after the infrared light has passed through the glass sample. Any phase shift imparted by the green-blocking filter to the infrared beam then appears on both the SK5-generated and the KTP-generated second-harmonic beams and so is automatically canceled.

We use a mode-locked (76-MHz repetition rate) and Q-switched (1-kHz pulse rate) Nd:YAG laser (Coherent Antares). Some of the infrared ( $\lambda = 1.064 \mu\text{m}$ ) light from the laser is frequency doubled in a LBO crystal that is noncritically phase matched, so that the green and the infrared beams follow the same optical path, as shown in Fig. 1. The polarization of the infrared and the green seeding beams is vertical, and we adjust their powers to 3 W and 2 mW, respectively. At the focus these powers correspond to  $4 \times 10^{11}$  and  $4 \times 10^8 \text{ W/cm}^2$  of peak power for the infrared and the green beams, respectively. We seed a virgin location in our Schott SK5 sample for 10 min. We then acquire interference pattern (a) be-

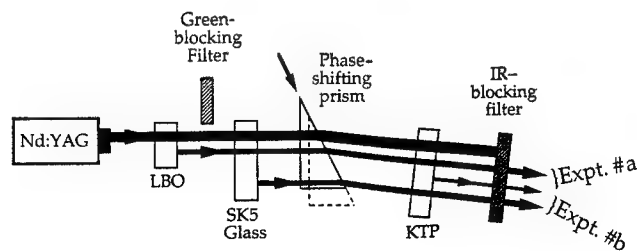


Fig. 1. Second-harmonic light generated in the KTP crystal interferes with that generated in either (a) the LBO crystal (green-block filter removed) or (b) the seeded SK5 glass sample (green-block filter present). Translating the glass prism shifts the phase of the green beam (from either LBO or SK5) compared to that of the green beam from the KTP crystal. The direction of the prism's arrow corresponds to the positive axis of Fig. 2.

tween the green beams generated in the LBO and KTP crystals by translating a prism and sampling the intensity pattern as it sweeps past our apertured detector. (For the beam power and exposure time used, the green generated by the SK5 sample is too weak to affect this interference pattern; the ratio of the glass-produced green and the LBO-produced green is less than  $10^{-3}$ .) We then block the green seeding beam from the LBO crystal with a green-blocking-infrared-passing filter. We measure interference pattern (b) of the green beams generated by the glass sample and by the KTP crystal, as shown in Fig. 2. (We are careful always to return the prism to its original position and eliminate backlash.) Because the green beam generated in the KTP crystal is common to both interference patterns (a) and (b), comparing these two interference patterns reveals the phase shift between the LBO-generated green (the seeding beam) and the SK5-generated green (the glass signal beam). We measured this phase shift twelve times and found an average phase shift  $\Delta\theta = -90^\circ \pm 7^\circ$ , where the minus means that the glass-produced green beam is in advance of the seeding green beam (as previously observed by Koch and Moore<sup>7</sup>).

Our technique is insensitive to nonlinear-optical phase shifts caused by self-phase modulation and cross-phase modulation so long as the infrared power is the same for both fringe-shift measurements. This is because any self-phase modulation of the infrared beam or cross-phase modulation of the infrared on the green beam will be common to both interference patterns (a) and (b) and so will cancel. Unfortunately, when we insert our green-blocking filter to eliminate the LBO-generated green and acquire interference pattern (b) we unavoidably decrease the infrared power by 10%. To check the importance of this effect, we seeded the glass sample and then measured the phase shift with different powers for the infrared reading beam. We observed a slight phase-shift dependence of  $2^\circ/W$ , which imparted a negligible error ( $<1^\circ$  of phase shift) to our experiments.

Recent theories of second-harmonic generation in glass make different predictions for how the phase shift  $\Delta\theta$  measured here will vary with the transverse position of the probing beam.<sup>12,13</sup> Therefore we varied the position of the probing beam to construct a spatial map of the phase shift  $\Delta\theta$ , as follows. First we seeded one spot in the glass sample, using  $\hat{y}$ -polarized green and infrared beams. We then probed at different locations, using a single  $\hat{y}$ -polarized infrared probing beam and translating the sample perpendicular to the direction of the probing beam. Figure 3 shows that the measured phase shift remained  $\Delta\theta = -90^\circ$  in the center of the seeded spot and along a horizontal scan through the center but underwent an abrupt step of  $180^\circ$  as we scanned in the vertical direction. This dependence of  $\Delta\theta$  on the position of the probing beam is precisely that expected if the electric field locked in the crystal (and causing the glass's frequency doubling) comes from the dipole field shown in Fig. 4.<sup>12</sup> Imagine probing this transverse dc field pattern near its center, where the dc electric field is directed up ( $+y$  direction). In

this central region the  $y$  component of this dipole dc electric field points up everywhere; however, if the probing beam is moved sufficiently above or below the edges of the dipole, the  $y$  component abruptly switches sign and points down. Switching the sign of the dc electric field imparts an extra  $180^\circ$  phase shift to the green beam generated in the glass sample [as we show in Eq. (2) below] and so causes the abrupt phase jumps seen in the data of Fig. 3. In contrast, translating the probe beam horizontally along the center-line scans a  $y$  component of the dc field that

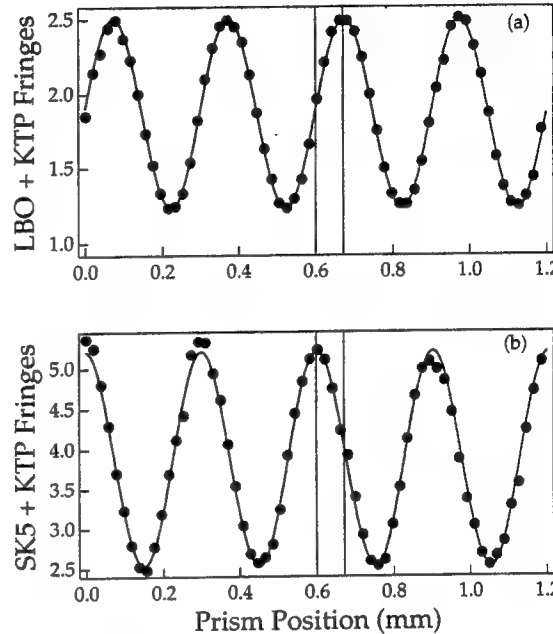


Fig. 2. (a) By translating a phase-shifting glass prism, we map out the interference pattern between the green beams from the LBO and KTP crystals. (b) We then block the green seeding beam (from the LBO crystal) and measure the interference pattern between the green beams from the SK5 glass sample and the KTP crystal. The phase shift between these two patterns gives the desired phase shift  $\Delta\theta$  between the seeding and the generated green beams in the SK5 glass sample.

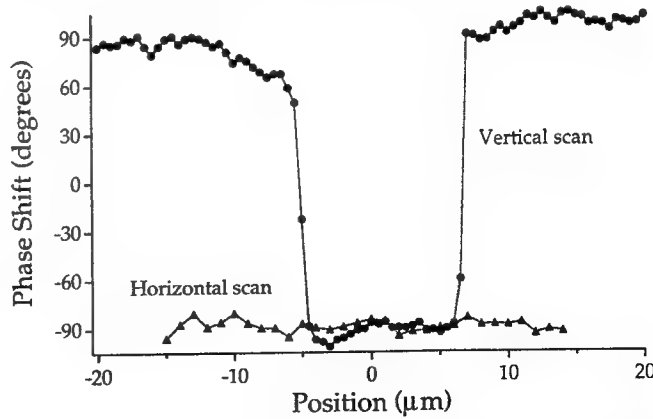


Fig. 3. Measured phase shift  $\Delta\theta$  versus the probing beam position near the center (position 0) of the seeded spot. For a horizontal scan (triangles) the phase shift is independent of the position. However, for a vertical scan (circles) the phase shift experiences  $180^\circ$  jumps on the outskirts of the seeding light beams, where the dc dipole electric field reverses sign (see Fig. 4).

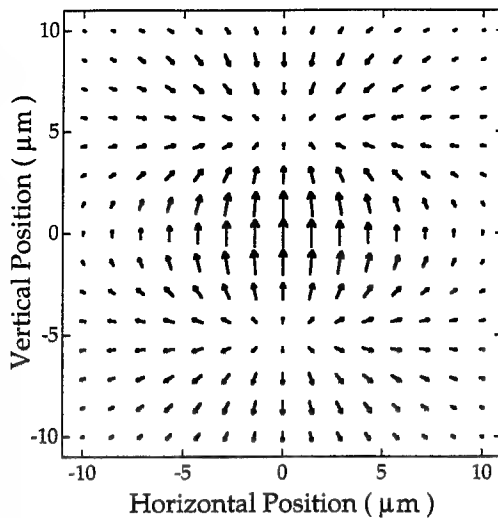


Fig. 4. Shape of the light-induced dc electric field transverse to the direction of the seeding beams when both of the seeding beams are vertically polarized (from Ref. 12). Note that along the vertical axis of symmetry ( $x = 0$ ) the dc field switches direction from up to down at the outskirts of the dipole pattern, near  $y = \pm 6 \mu\text{m}$ . In contrast, along the horizontal axis of symmetry ( $y = 0$ ) the dc field points up everywhere. This dipole electric field explains the phase-shift data seen in Fig. 3.

always points in the same direction ( $+y$ ). Therefore we expected and observed no jumps in the measured phase shift  $\Delta\theta$  as we scanned the horizontal position of the probing beam in the glass, as shown in Fig. 3. Notice that the  $x$  component of the dc electric field is negligible along centered horizontal and vertical scans, so it does not affect the measured phase. We measured the same phase map even when we reduced the green seeding intensity by a factor of 200, which was the lower limit for our detection system.

In these experiments the intensity of the glass-generated green is always much less than that of the LBO-generated green that seeded the glass. Therefore the LBO-generated green beam sets the phase of the dc field in the glass, and the weak, glass-generated green beam does not affect its own generation. In this case, the seeding fields at  $\omega$  and  $2\omega$  create a dc electric field in the glass given by<sup>2</sup>

$$\begin{aligned} E_{dc} &= \Gamma E_{\omega}^* E_{\omega}^* E_{2\omega}^{LBO} \exp[i(k_{2\omega} - 2k_{\omega})z] \\ &= |\Gamma| E_{\omega}^* E_{\omega}^* E_{2\omega}^{LBO} \exp[i(k_{2\omega} - 2k_{\omega})z + i\phi_{\Gamma}], \end{aligned} \quad (1)$$

where  $z$  is the direction of light propagation,  $\Gamma$  is the growth rate constant,  $\phi_{\Gamma}$  is the spatial phase shift between the three-field interference term and the dc electric field, and  $E_{2\omega}^{LBO}$  is the optical field of the green seeding beam. We wish to determine  $\phi_{\Gamma}$ . The coupled-wave equation for dc-field-induced second-harmonic generation is

$$\frac{dE_{2\omega}^{glass}}{dz} = i \frac{3\omega}{2n_{2\omega}c} \chi^{(3)} E_{dc} E_{\omega} E_{\omega} \exp[i(2k_{\omega} - k_{2\omega})z]. \quad (2)$$

Inserting Eq. (1) into Eq. (2) and keeping only the phase-matched terms in the interaction, we find that

$$\frac{dE_{2\omega}^{glass}}{dz} = i \frac{3\omega}{2n_{2\omega}c} \chi^{(3)} |\Gamma| |E_{\omega}|^4 E_{2\omega}^{LBO} \exp(i\phi_{\Gamma}). \quad (3)$$

The measured phase shift  $\Delta\theta$  between the glass-generated green and the LBO-generated seeding green will be  $\Delta\theta = \phi_{\Gamma} + 90^\circ$  because of that factor of  $i$  in Eqs. (2) and (3). Our measurements yield a value  $\Delta\theta = -90^\circ$ , which implies that  $\phi_{\Gamma} = -180^\circ$ , so that the dc field induced inside the SK5 glass is spatially in phase with the three-field interference term  $-E_{\omega}^* E_{2\omega}$ . This result confirms the spatially local response seen in Ge-doped fused silica<sup>6,7</sup> and in the Soviet glass ZhS-4.<sup>8</sup>

Compared with previous techniques, our experimental technique offers several advantages for studying the phase of the frequency-doubled light generated by glass. Because we do not disturb the seeding beam, we can map out the phase at different locations in the sample. We observe a  $180^\circ$  discontinuity in the phase of the green light generated in the glass sample as we move the optical probe toward the edge of the seeded region in the vertical direction but not in the horizontal direction. These results confirm that the original green and infrared seeding beams create a dipole-like charge distribution in the glass.

This research was supported by grant F49620-92-J-0022 of the U.S. Air Force Office of Scientific Research (AFOSR) and by the Joint Services Electronics Program. Vince Dominic thanks the AFOSR Summer Faculty Research Program and the Materials Directorate at Wright-Patterson Air Force Base for their support.

\*Present address, Center for Electro-Optics, University of Dayton, Dayton, Ohio 45469-0245.

## References

1. U. Österberg and W. Margulis, Opt. Lett. **11**, 516 (1986); **12**, 57 (1987).
2. R. H. Stolen and H. W. K. Tom, Opt. Lett. **12**, 585 (1987).
3. V. Dominic and J. Feinberg, Phys. Rev. Lett. **71**, 3446 (1993).
4. V. Mizrahi, Y. Hibino, and G. Stegeman, Opt. Commun. **78**, 283 (1990).
5. E. M. Dianov, P. G. Kazansky, D. S. Starodubov, and D. Yu. Stepanov, Sov. Lightwave Commun. **2**, 83 (1992).
6. W. Margulis, I. C. S. Carvalho, and J. P. von der Weid, Opt. Lett. **14**, 1346 (1989).
7. K. Koch and G. T. Moore, Opt. Lett. **16**, 1436 (1991).
8. M. A. Bolshtyansky, V. M. Churikov, Yu. E. Kapitzky, A. Yu. Savchenko, and B. Ya. Zel'dovich, Opt. Lett. **18**, 1217 (1993).
9. V. L. Vinetskii, N. V. Kukhtarev, S. G. Odulov, and M. S. Soskin, Sov. Phys. Usp. **22**, 742 (1979).
10. E. M. Dianov, P. G. Kazanskii, and D. Yu. Stepanov, Sov. J. Quantum Electron. **20**, 849 (1990).
11. M. I. Dyakonov and A. S. Furman, Electron. Lett. **27**, 1429 (1991).
12. V. Dominic and J. Feinberg, Opt. Lett. **18**, 784 (1993).
13. T. J. Driscoll and N. M. Lawandy, J. Opt. Soc. Am. B **11**, 355 (1994).

## Light-Induced Second-Harmonic Generation in Glass via Multiphoton Ionization

Vince Dominic\* and Jack Feinberg

Departments of Electrical Engineering and Physics, University of Southern California, Los Angeles, California 90089-0484  
(Received 1 July 1993)

Irradiating glass by intense light at frequencies  $\omega$  and  $2\omega$  generates a semipermanent dc electric field in the glass that transforms the glass into a phase-matched optical-frequency doubler. We map out this dc electric field over a wide variety of experimental conditions. We show that its symmetries are predicted by a theory based on the interference of competing multiphoton ionization channels.

PACS numbers: 32.80.Fb, 32.80.Rm, 42.65.Ky, 42.70.Ce

Intense light containing frequencies  $\omega$  and  $2\omega$  can produce a semipermanent, spatially periodic dc electric field in glass [1-4]. This strong dc field ( $\sim 10^4$  V/cm) then enables phase-matched second-harmonic generation in the glass [5]. A fundamental question is: What microscopic mechanism produces this strong dc electric field? Explanations invoke either light-induced currents [6-8] or structural orientation [5,9]. Our data support the former; the intense light beams at frequency  $\omega$  and  $2\omega$  cause electrons to be ejected with an angular distribution that is not inversion symmetric and which varies periodically in space [10-12]. In this Letter we map out the actual dc electric fields and show, in four different cases, that these fields are well described by a theory based on the interference of different multiphoton ionization channels.

We produce the dc electric field by irradiating a 4 mm thick glass sample (Schott SK-5) with the fundamental ( $\lambda = 1.064 \mu\text{m}$ ) and the second-harmonic light beams of a  $Q$ -switched, mode-locked Nd:YAG laser. The peak powers of the infrared and green beam are typically 2 and 0.02 MW, respectively. Both colors are focused to the same spot (to within  $0.5 \mu\text{m}$ ) either in the bulk or on the surface of the glass by a lens ( $f = 25 \text{ mm}$ ) designed to be achromatic at our two wavelengths. After several minutes of intense laser irradiation we block the two seeding beams; any charges that moved during laser irradiation are then trapped in place in the glass. We probe the glass sample with a strongly focused infrared beam and detect any second-harmonic light produced by the glass sample. By inducing the dc field on the surface of the glass and probing with a tightly focused infrared beam we significantly improve the spatial resolution of the dc field maps compared to our previous work [4].

The strength of the generated second-harmonic optical field passing through a polarization analyzer  $\hat{\epsilon}_a$  is

$$E_{2\omega} \propto \hat{\epsilon}_a^* \cdot \{ \chi_{xyx}^{(3)} (\hat{\epsilon}_\omega \cdot \hat{\epsilon}_\omega) \hat{\epsilon}_{dc} + 2\chi_{xxyy}^{(3)} \hat{\epsilon}_\omega (\hat{\epsilon}_\omega \cdot \hat{\epsilon}_{dc}) \} E_{dc} E_\omega E_\omega, \quad (1)$$

where the circumflex denotes the (possibly complex) unit polarization vector, and  $E_{dc}$  and  $E_\omega$  represent the complex amplitudes of the dc electric field and the infrared optical probing field, respectively. By prudently choosing

the reading polarization and the analyzer polarization we can map out the individual components of the dc electric field.

We created four different dc electric field patterns by irradiating separate regions of the glass sample with differently polarized green and infrared seeding beams, as follows: (1) Both seeding beams were  $\hat{y}$  polarized; (2) the infrared beam was  $\hat{y}$  polarized and the green beam was  $\hat{x}$  polarized; (3) the infrared and green seeding beams had the same circular polarization; and (4) the infrared and green seeding beams had opposite circular polarizations.

Figure 1 shows maps of the measured second-harmonic power for case 1. With a  $\hat{y}$ -polarized probing beam and a  $\hat{y}$ -polarized analyzer we measure the  $\hat{y}$  component of the

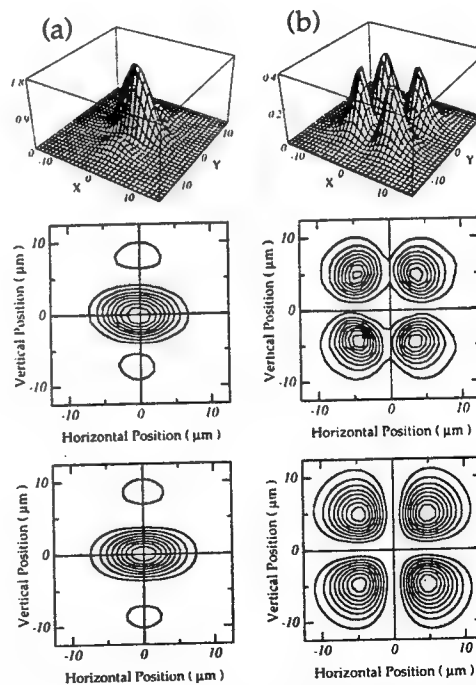


FIG. 1. Strength of the second-harmonic signal versus transverse position after case 1 seeding (see text): (a)  $|(\hat{E}_{dc})_y|^2$  and (b)  $|(\hat{E}_{dc})_x|^2$ . The top two rows are the experimental data displayed in two formats. The bottom row is calculated from a charge distribution that is the spatial derivative of a Gaussian along the  $y$  direction.

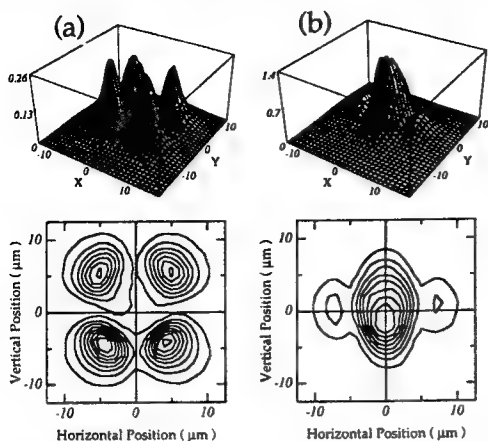


FIG. 2. Strength of the second-harmonic signal versus transverse position after case 2 seeding (see text): (a)  $|E_{dc}|_y^2$  and (b)  $|E_{dc}|_x^2$ . The data are identical to that in Fig. 1 except that  $x$  and  $y$  are now switched, as predicted by theory.

dc electric field,  $(E_{dc})_y$ . Figure 1(a) shows the magnitude  $|E_{dc}|_y^2$  in the  $x$ - $y$  plane: We find a strong central hill, with two smaller hills positioned vertically above and below, and the signal decreases to nearly zero between the hills. For Fig. 1(b) we measured the variation of the  $\hat{x}$  component of the dc field,  $(E_{dc})_x$ , using a probing beam and analyzer that were both  $\hat{x}$  polarized. Now we find four strong peaks, with the signal weak in the interconnecting valleys. The central peak in Fig. 1(a) is a factor of 3 larger than the strongest of the four peaks in Fig. 1(b). These patterns are consistent with charges that had separated along the  $\hat{y}$  direction in the glass, creating a dipolelike electric field [4]. Predicted maps using this *ad hoc* field are shown for comparison.

In case 2 the two seeding beams have different polarizations; the infrared seeding beam is  $\hat{y}$  polarized while the green seeding beam is  $\hat{x}$  polarized. Figure 2 shows that the light-induced dc electric field is now oriented primarily along the  $\hat{x}$  direction; i.e., the charges have migrated along the polarization direction of the incident green beam.

In case 3 we use right circularly polarized infrared and green seeding beams. Now we expect a helical dc field pattern, as sketched in the inset of Fig. 3. The direction of the dc electric field rotates one full turn after traveling in the  $z$  direction by the phase-matching periodicity distance  $(0.532 \mu\text{m})/(n_{2\omega} - n_\omega) = 36 \mu\text{m}$ , where the  $n$ 's are the refractive indices at  $2\omega$  and  $\omega$ . Inspection of Eq. (1) shows that the combination right-circular probing beam and right-circular polarization analyzer projects out the spatially counterclockwise-spiraling component of the dc field. Figure 3(a) shows the resulting spatial map: a compact, solitary bump in the center. A left/left probing experiment detects any clockwise-spiraling dc field, and the resulting spatial map [Fig. 3(b)] resembles a volcano. These maps are expected for a spatially spiraling charge

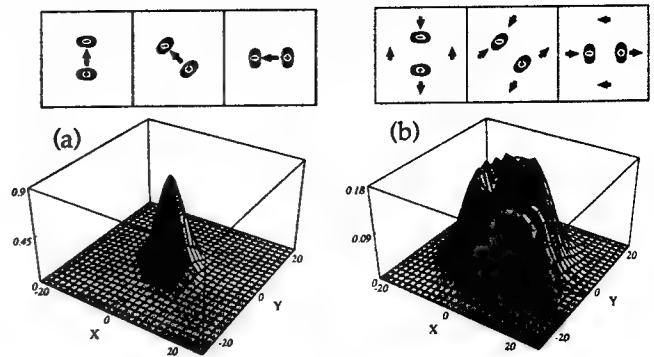


FIG. 3. Strength of the second-harmonic signal versus transverse position after case 3 seeding (see text): (a)  $|E_{dc}|_y^2$  and (b)  $|E_{dc}|_x^2$ . The insets show one-quarter period of a spiraling charge pattern and the associated spiraling dc fields. Case (a) picks out any *counterclockwise* spiraling dc field, which is strongest at the center of the spiraling charge pattern. Case (b) picks out any *clockwise* spiraling dc field, which is strongest at the perimeter of the spiraling charge pattern.

distribution, because its dc field rotates in one direction at the center but rotates in the opposite direction off center (see insets). [The signal does not drop completely to zero at the center of Fig. 3(b) due to the finite size of our probing beam.] We confirmed the signal contours shown in all the above figures with numerical calculations that account for the spatial shape of the dc electric field and the propagation of the Gaussian probing beams [4].

Finally, we prepared the sample with seeding beams having opposite circular polarizations (case 4), and measured a peak signal strength that was 400 times weaker than the peak signal strengths in cases 1–3 above, and with a dc field that spiraled in the opposite direction than the dc field in case 3. However, the purity of our circular polarizations was only  $\sim 95\%$ , and any leakage of the opposite circular polarization of the green beam would produce the mirror image of case 3.

We also performed separate experiments to confirm the orientation of the dc electric field. We position the probing beam at each pattern's center of symmetry, rotate both the probing beam's linear polarization and the linear analyzer to an angle  $\Phi$ , and measure the signal strength as a function of  $\Phi$ . Figure 4 shows our measurements plotted in cylindrical coordinates, where the radial distance is the strength of the measured second-harmonic signal. The solid lines are fits using Eq. (1), assuming that the dc electric field at the center is purely in the  $\hat{y}$  direction for case 1 [Fig. 4(a)] and purely in the  $\hat{x}$  direction for case 2 [Fig. 4(b)]. The fit for case 3 [Fig. 4(c)] allows the Cartesian components of the dc electric field to be spatially out of phase (as expected for a spiraling field), so that the maximum of the  $\hat{x}$  component of the field occurs at a different  $z$  plane than the maximum of the  $\hat{y}$  component. The fit gave a ratio of  $(E_{dc})_y/(E_{dc})_x = 1.1 \pm 0.2$  (instead of the expected 1) and a spatial

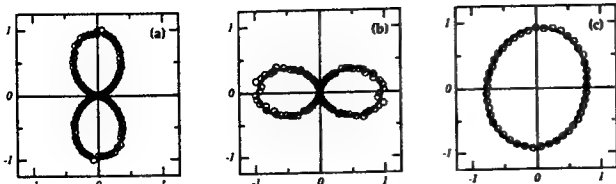


FIG. 4. Polar maps of the measured (circles) and predicted (solid lines) dc electric field strength at the center of Figs. 1, 2, and 3. (a) In case 1 the field is completely along  $\hat{y}$ . (b) In case 2 the field is completely along  $\hat{x}$ . (c) In case 3 the dc field spirals with  $z$ .

phase shift between the field components of  $87.2^\circ \pm 1.5^\circ$  (instead of the expected  $90^\circ$ ).

These spatial maps, as well as the far-field maps of Di-anov *et al.* [3], convincingly rule out structural orientation models since these models predict signals that monotonically decrease with distance from the beam center. In contrast, we observe spatial structure in the measured signal consistent with a dc electric field produced by charge separation.

Photogalvanic current models [6,7] predict a dc current  $j_{pg}$  proportional to [13]

$$j_{pg} \propto \{a(\hat{e}_\omega^* \cdot \hat{e}_\omega^*)\hat{e}_{2\omega} + 2b\hat{e}_\omega^*(\hat{e}_\omega^* \cdot \hat{e}_{2\omega})\}E_\omega^*E_\omega^*E_{2\omega}\exp(i\Delta kz), \quad (2)$$

where  $\Delta k = k_{2\omega} - 2k_\omega$ . Equation (2) contains the distinct combinations of vectors in an isotropic media that give another vector which uses all three of the optical fields  $E_\omega\hat{e}_\omega$ ,  $E_\omega\hat{e}_\omega$ , and  $E_{2\omega}\hat{e}_{2\omega}$  precisely once and that varies as  $\exp(i\Delta kz)$ . The dc electric field arising from this current possesses all of the symmetries of our data. However, this form of  $j_{pg}$  lacks many of the details contained in richer, more complete theories. We expand the multiphoton ionization model [8] here and show that the polarization dependences of Eq. (2) are recovered. We assume that electrons in the glass are ejected after absorbing either a single green photon or two infrared photons, and that these two ionization channels interfere. In fact, the number of absorbed photons is larger than this in glass [14]. However, our experiments here probe only the  $\exp(i\Delta kz)$  component of the charge distribution, in fact, only its transverse symmetries, and this phase-matched component is always produced by the interference of channels having one unmatched green photon and two unmatched infrared photons. We have also derived the expected photoelectron angular distributions for cases having additional photons [15] and find that, even when we include the proliferation of possible angular momentum states, we obtain the same transverse symmetries.

For simplicity we assume an *s*-type ground state, non-resonant ionization, the dipole approximation, classical fields, hydrogenic intermediate state wave functions, and no spin-orbit coupling. We make the standard partial-wave expansion of the electron wave-function final state

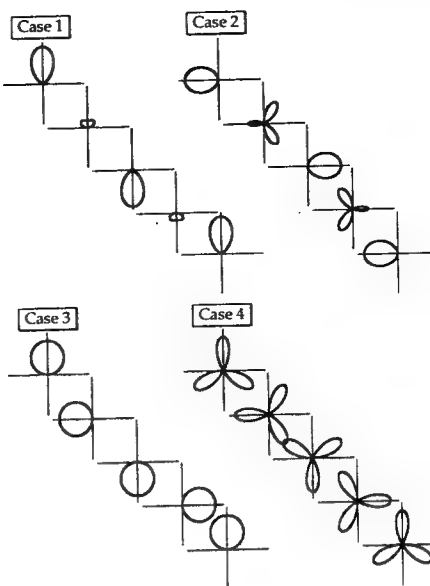


FIG. 5. Plots of the probability for ejecting electrons in the  $x$ - $y$  plane at different  $z$  planes for cases 1 through 4 above. The charges are asymmetrically ejected primarily along  $\hat{y}$  for case 1,  $\hat{x}$  for case 2, in a spiral for case 3, and in a spiral of opposite handedness for case 4.

[16]. We let  $z$  be the propagation direction and the optical polarization vectors lie in the  $x$ - $y$  plane. The continuum state can be reached by *either* of two ionization paths, and in these experiments we cannot distinguish which path was taken. Consequently, the two paths interfere to produce the following angular distribution:

$$\frac{d\sigma}{d\Omega} \propto |M_{fi}^{(1)} + M_{fi}^{(2)}|^2, \quad (3)$$

where  $M_{fi}^{(1)}$  and  $M_{fi}^{(2)}$  are the one- and two-photon matrix elements, respectively. The cross terms in the expansion of Eq. (3) vary periodically along the propagation direction  $z$ . These terms are not inversion symmetric; they eject the electrons in a preferred direction, and create the spatially periodic, transverse, dc electric field.

Figure 5 shows plots of the probability of electron ejection vs azimuthal angle  $\Phi$  for the four different cases. If the infrared and the green beams are both  $\hat{y}$  polarized (case 1), then in the plane transverse to the propagation direction the noncentrosymmetric term in the angular distribution is

$$\frac{d\sigma}{d\Omega} \Big|_{\text{noncentro}} = \{Q + Q'\sin^2\Phi\} \{Q''\sin\Phi\} \exp(i\Delta kz) + \text{c.c.}, \quad (4)$$

where the bracketed terms arise from two- and one-photon ionization, respectively. The complex  $Q$ 's include the radial overlap integral, the summation over intermediate states, and the scattering phase shift. In Eq. (4) the preferential direction of electron ejection is seen to

vary sinusoidally with  $z$  between  $+\hat{y}$  and  $-\hat{y}$  (because of the  $\sin\Phi$  term in the second bracket) in agreement with our data. That is, the charges separate along the  $y$  direction, creating a dipole field. Case 1 was also studied in Refs. [2-4,11,12,17] and their data are consistent with the simple analysis given here.

For case 2, where the infrared light is  $\hat{y}$  polarized but the green light is  $\hat{x}$  polarized, theory gives a result identical to Eq. (4) but with  $\cos\Phi$  substituted for  $\sin\Phi$  in the second bracketed term. In agreement with our data, the preferential direction of electron ejection has now switched to vary periodically between  $+\hat{x}$  and  $-\hat{x}$ .

For case 3, where both the green and the infrared are right circularly polarized, we find

$$\left. \frac{d\sigma}{d\Omega} \right|_{\text{noncentro}} = \{Q''' e^{i\Phi}\} \exp(i\Delta kz) + \text{c.c.} \quad (5)$$

Now the preferential direction of electron ejection rotates in the  $x$ - $y$  plane periodically with  $z$ , and so produces a helical dc field. Our theory predicts that this helical field spirals with the same spatial handedness as the green circular polarization (so long as we are in a normally dispersive wavelength range, where  $n_{2\omega} - n_\omega > 0$ ), and this is what we observe.

Finally, if the infrared is right and the green is left circularly polarized we obtain

$$\left. \frac{d\sigma}{d\Omega} \right|_{\text{noncentro}} = \{Q''' e^{i3\Phi}\} \exp(i\Delta kz) + \text{c.c.} \quad (6)$$

Now the electron ejection pattern has become three lobed and spirals in the opposite direction from case 3. This three-lobed ejection pattern is inefficient in producing an electric field in the  $x$ - $y$  plane (and, in fact, produces a zero electric field at the center). The dc field is expected to be small in this case, as we observe.

In conclusion, we find excellent agreement between the predictions of photocurrent models and the measured spatial shapes of the dc electric field induced in glass samples by intense light beams at frequencies  $\omega$  and  $2\omega$ . Our data rule out structural reorientation models. The symmetries contained in the photocurrent model can be derived from the interference of two multiphoton ionization channels. We also note the universality of the symmetries observed here; we found similar dc electric field shapes in all the glass samples that we tried to date, including a  $\text{GeO}_2$ -doped  $\text{SiO}_2$  optical fiber preform, and samples of Schott Glass SK4 and BK7.

We thank Dan Elliott for informative and pleasant discussions, and Joseph Haydn of Schott Glass and Frank Dabby of Ensign-Bickford Optical Technologies, Inc. for glass samples. This work was supported by AFOSR Grant No. F49620-92-J-0022.

*Note added.*—Since the submission of this manuscript we have learned of similar measurements [17] that confirm our cases 1 and 2.

\*Present address: Electro-Optics Program, University of Dayton, 300 College Park, Dayton, OH 45469-0227.

- [1] A. Kamal *et al.*, in *Digest of Optical Society of America Annual Meeting* (Optical Society of America, Washington, DC, 1990), paper PD25.
- [2] V. Mizrahi, Y. Hibino, and G. Stegeman, *Opt. Commun.* **78**, 283 (1990).
- [3] E. M. Dianov, P. G. Kazansky, D. S. Starodubov, and D. Yu. Stepanov, *Sov. Lightwave Commun.* **2**, 83 (1992).
- [4] V. Dominic and J. Feinberg, *Opt. Lett.* **18**, 784 (1993).
- [5] R. H. Stolen and H. W. K. Tom, *Opt. Lett.* **12**, 585 (1987).
- [6] E. M. Dianov, P. G. Kazansky, and D. Yu. Stepanov, *Kvant. Elektron. (Moscow)* **16**, 887 (1989) [*Sov. J. Quantum Electron.* **19**, 575 (1990)].
- [7] B. Ya. Zel'dovich and A. N. Chudinov, *Pis'ma Zh. Eksp. Teor. Fiz.* **50**, 405 (1989) [*JETP Lett.* **50**, 439 (1989)].
- [8] D. Z. Anderson, V. Mizrahi, and J. E. Sipe, *Opt. Lett.* **16**, 796 (1991).
- [9] F. Charra, F. Kajzar, J. M. Nunzi, P. Raimond, and E. Ildiart, *Opt. Lett.* **18**, 941 (1993).
- [10] H. G. Muller, P. H. Bucksbaum, D. W. Schumacher, and A. Zavriyev, *J. Phys. B* **23**, 2761 (1990).
- [11] N. B. Baranova, I. M. Beterov, B. Ya. Zel'dovich, I. I. Ryabtsev, A. N. Chudinov, and A. A. Shul'ginov, *Pis'ma Zh. Eksp. Teor. Fiz.* **55**, 451 (1992) [*JETP Lett.* **55**, 439 (1992)].
- [12] Y.-Y. Yin, C. Chen, D. S. Elliott, and A. V. Smith, *Phys. Rev. Lett.* **69**, 2353 (1992).
- [13] E. M. Dianov, V. O. Sokolov, and V. B. Sulimov, *Sov. Lightwave Commun.* **2**, 133 (1992).
- [14] V. Dominic and J. Feinberg, *Opt. Lett.* **17**, 1761 (1992).
- [15] V. Dominic, Ph.D. thesis, University of Southern California, 1993.
- [16] S. J. Smith and G. Leuchs, in *Advances in Atomic and Molecular Physics* (Academic, Boston, 1988), Vol. 24.
- [17] M. A. Bolshtyansky, V. M. Churikov, Yu. E. Kapitzky, A. Yu. Savchenko, and B. Ya. Zel'dovich, *Pure Appl. Opt.* **1**, 289 (1992).

# High-brightness output from a laser-diode array coupled to a phase-conjugating mirror

Stuart MacCormack and Jack Feinberg

Departments of Physics and Electrical Engineering, University of Southern California, Los Angeles, California 90089-0484

Received September 11, 1992

We obtain single-lobed, near-diffraction-limited output from a 20-element laser-diode array coupled to an apertured photorefractive phase conjugator. At low driving currents the output beam is diffraction limited and contains 75% of the total output power emanating from the array. At high driving current a  $1.5\times$  diffraction-limited lobe contains 490 mW of power, or 54% of the output power. By studying the near-field emission pattern and the frequency spectrum of the laser, we confirm that the apertured conjugator selects a narrow range of output array transverse modes.

Although laser-diode arrays can produce impressive amounts of optical power, they usually simultaneously operate on many transverse modes, which makes their far-field pattern a mess.<sup>1,2</sup> Their poor beam quality makes laser-diode arrays ill suited for many applications, such as launching intense light into single-mode waveguides and pumping minilaser systems.

Here we couple a laser-diode array to an external, photorefractive phase conjugator and thereby force the array to operate on a single transverse mode. Even while running close to its maximum rated output power, this device now puts out a near-diffraction-limited beam.

A number of external devices have been used previously to modify the far-field emission profile of laser-diode arrays. Spatial filters within the external cavity can force the array to operate in its fundamental, in-phase transverse mode.<sup>3,4</sup> Similarly, a mirror aligned to retroreflect one side of the output beam can enhance operation of a modified high-order array transverse mode,<sup>5-7</sup> although the resulting device is then extraordinarily sensitive to alignment, temperature, and output power. Optical phase conjugation is an ideal way to feed light back into a laser-diode array, because the conjugator automatically returns the light to the high-gain region of the diode. A laser-diode array coupled to an off-axis phase-conjugating mirror gave near-diffraction-limited single-lobed output in the far field.<sup>8</sup> However, that system was not self-starting, requiring an external light source, and the stability and reflectivity of the phase conjugator limited the system's output power. In this Letter we describe a laser-diode array plus phase conjugator that overcomes all of these problems.

Figure 1 shows the optical setup. A 1-W, 20-stripe, laser-diode array (Spectra Diode Labs 2461-P1 with no special coatings) is mounted on a heat sink to maintain the laser's temperature at 10 °C. The array of lasers forms a line in the horizontal plane, and the laser's output is polarized along this line. The output of the array has poor spatial coherence along a line parallel to the array but near-perfect spatial

coherence along a line perpendicular to the array. The laser output is collected by an 8-mm focal-length lens (N.A. 0.5) and passes through a half-wave plate, which rotates the polarization through 90° and makes the light's axes of coherence and polarization parallel. A prism positioned in the far-field plane (generated by the  $f = 100$  mm lens) picks off one half of the quasi-twin-lobed output beam. Two mirrors oriented at 45° to the plane of the table direct the light into a BaTiO<sub>3</sub> crystal. The two 45° mirrors rotate both the light's polarization and coherence axes by 90° into the horizontal plane. This arrangement of mirrors and wave plates ensures that the polarization and the coherence axes of the light lie in the plane defined by the BaTiO<sub>3</sub> crystal's *c* axis and the direction of the incident beam, which is necessary for the crystal to operate as a CAT conjugator.<sup>9</sup> (An alternative and simpler arrangement is to eliminate the two 45° mirrors and instead rotate the crystal so that its *c* axis points out of the plane of the table.)

The chromium-doped BaTiO<sub>3</sub> crystal (named CROW) measures 5.8 mm × 5.2 mm × 2.9 mm, with the *c* axis along the longest dimension, and operates

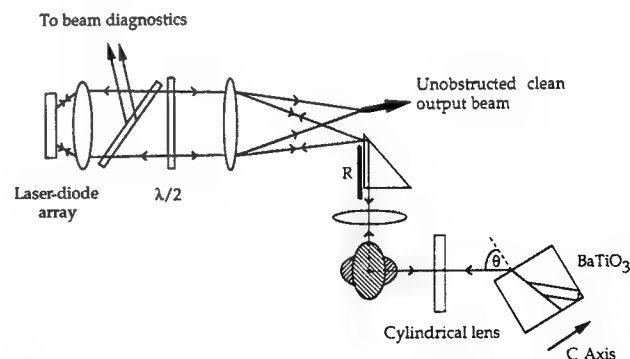


Fig. 1. Laser-diode array coupled to a self-pumped phase conjugator. The half-wave plate rotates the plane of polarization, and the two 45° mirrors align the coherence plane and the plane of polarization parallel to the BaTiO<sub>3</sub> crystal's *c* axis. The right-angled prism and the vertical razor edge *R* form an adjustable aperture in the far field. The angle of incidence of the signal beam on the crystal is  $\theta = 60^\circ$ .

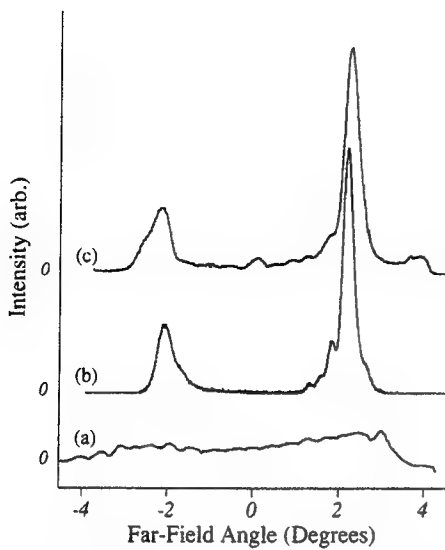


Fig. 2. Array far-field pattern under free-running conditions [curve (a)], with phase-conjugate external cavity feedback at a low drive current ( $1.7I_{th}$ ) [curve (b)], and with phase-conjugate feedback at the maximum drive current ( $3.1I_{th}$ ) [curve (c)]. The main lobe in curve (b) has a FWHM of  $0.317^\circ$ , which corresponds to 1.09 times the diffraction limit (a Strehl ratio of 0.44). Curve (c) corresponds to an output power of 910 mW, and the main lobe has a FWHM of  $0.43^\circ$ , 1.48 times the diffraction limit (a Strehl ratio of 0.30).

as a self-pumped CAT conjugator. A spherical and cylindrical lens pair generates a 1.5-mm square beam at the crystal face. All the transmission optics, excluding the prism, are antireflection coated at the laser wavelength. A razor edge and the vertical prism edge form a variable spatial filter in the far field. The frequency spectrum of the laser output is analyzed by a Spex 0.75-m double-grating spectrometer with a resolution of  $\sim 0.01$  nm. We record either the near-field or the far-field beam profile by a 512-element linear photodiode array.

When we first switch on the laser, its output is that of a usual, free-running laser-diode array: a poorly defined, twin-peaked, far-field pattern ( $\sim 40$  times the diffraction limit of the  $200\text{-}\mu\text{m}$  emitting region) having a broad frequency spectrum. After a short delay (typically 20 s), the phase conjugator turns on, and one of the farfield lobes grows at the expense of the other one. After an additional  $\sim 50$  s the phase-conjugate reflectivity attains its steady-state level, and the laser settles into single-peaked operation. With a drive current of 0.8 A ( $1.7I_{th}$ ), the angular width of this output lobe in the far field is 2.9 times the diffraction limit. Narrowing the width of the aperture then produces a diffraction-limited beam at this drive current, as shown in Fig. 2(b). Once the phase-conjugate mirror turns on, it can track in real time small changes in the laser's far-field profile or in the aperture's position. The most efficient operation of the external cavity always occurs for an emission angle centered close to  $2.2^\circ$ . For the case of high-power operation of the cavity, the prism and razor edges are positioned at far-field angles of  $-1.98^\circ$  and  $-2.58^\circ$ . The array maintains single-peaked emission

for all driving currents. The maximum driving current is 1.5 A ( $3.1I_{th}$ ), which produced a total array output power of 910 mW. We limit the driving current to 1.5 A to avoid the possibility of intensity damage to the array facet. At high output powers the far-field lobe width gradually increases up to 1.48 times the diffraction limit at the maximum array drive current. In addition, at high drive currents a larger fraction of the array output lies outside the locked array mode and appears as a background intensity in the far field. These effects may be due to self-focusing of the light in the laser gain medium, increased free-running mode competition, and the decreased phase-conjugate reflectivity (discussed below) that accompanies the higher laser drive currents. At the 1.5-A maximum drive current, the main lobe contains 493 mW of power (of which 406 mW is contained in a Gaussian spike of width 1.48 times the diffraction limit).

The phase-conjugate reflectivity of the CAT conjugator decreases from 35% at small driving currents, close to the lasing threshold, to 14% at the highest measured drive current. This, in conjunction with the increasing signal power, causes the power fed back to the laser from the conjugator to remain roughly constant at  $\sim 13$  mW over the range of drive currents investigated. The total laser output is approximately 3% higher with the conjugator than without it at the same driving current.

The external cavity output exhibits surprising intensity stability ( $<0.5\%$  fluctuations) over a time scale ranging from a few seconds to hours. The dynamic response of the phase-conjugate mirror compensates for gradual changes in the drive current, operating wavelength, or ambient temperature with no degradation in the single-peaked profile. The dark-storage time of this particular  $\text{BaTiO}_3$  crystal exceeds 12 h, so that, once the phase conjugator turns on and establishes single-peaked laser emission, the conjugator will then turn on instantly the next day, and the laser will immediately display a single-mode output, even if the laser had been switched off overnight.

When the conjugator first turns on, it pulls the laser's output spectrum  $\sim 2$  nm toward the red and

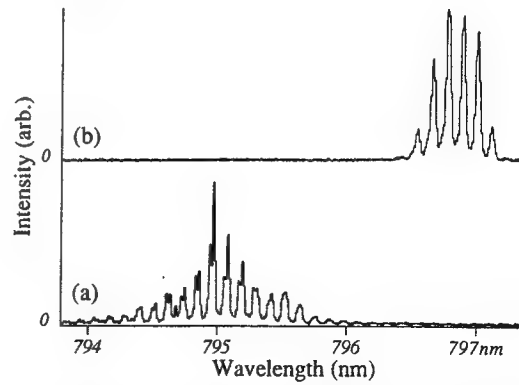


Fig. 3. Frequency spectrum of the array output showing the longitudinal modes under free-running conditions [curve (a)] and with phase-conjugate external cavity feedback [curve (b)]. The conjugator shifts and narrows the frequency spectrum. Note the absence of fine splitting in curve (b), indicating that the laser is operating on one array mode (or perhaps a few adjacent modes).

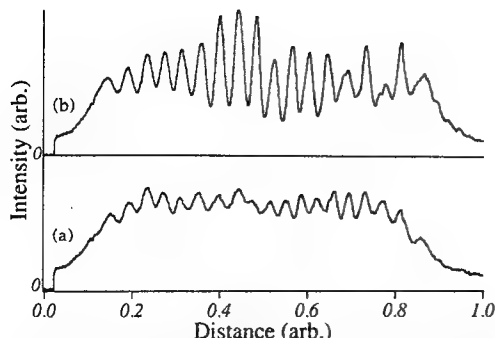


Fig. 4. Array near-field profile under free-running conditions [curve (a)] and with external cavity feedback [curve (b)]. The drive current was 1 A. Note the increased intensity modulation present with phase-conjugate feedback, indicating that the laser is running on only a few array modes.

narrows the spectrum to a few longitudinal modes under a stable, 0.5-nm Gaussian envelope (FWHM), as Fig. 3 shows. This frequency width is close to the expected  $\sim 1$ -nm-wavelength Bragg selectivity of the grating self-formed inside the CAT conjugator. For comparison, we also tried replacing the phase-conjugate mirror with an ordinary high-reflectivity plane mirror and adjusted the lens pair to form a focus at this mirror. With careful (and finicky) alignment, at a drive current of 1 A we were able to generate a near-diffraction-limited far-field lobe containing 34% of the array output. However, this simple mirror was less successful at higher drive currents; at 1.5 A the output lobe could not be narrowed below 1.75 times the diffraction limit, and the lobe contained only 25% of the array's total output.

The far-field aperture, and to a lesser extent the phase-conjugate mirror, presents a small angular window through which the array can receive optical feedback. Because each array mode has a slightly different emission angle for its main far-field lobes,<sup>1,2</sup> the far-field aperture enhances the mode (or closely spaced modes) whose emission angle is directed at the aperture window. By adjusting the position and the width of the aperture, it is possible to enhance a single array mode at the expense of the other modes and so produce a sharp, twin-lobed structure in the far-field. The array modes  $\nu = 19$  and  $\nu = 20$  for a 20-element array are predicted to have emission angles of  $2.18^\circ$  and  $2.29^\circ$ , respectively. These compare well with the main lobe emission angles of  $2.18^\circ$  and  $2.24^\circ$  measured from the data in Fig. 2. This suggests that the array is operating primarily on the  $\nu = 19$  mode, with some of the  $\nu = 20$  mode creeping in at higher powers.

The phase conjugator ensures that all the light fed back to the laser is coupled into natural modes of the laser. In close analogy to conventional injection locking of a laser-diode array,<sup>10</sup> the asymmetry of the feedback in this external cavity causes a pre-

ferred direction of emission at the same angle as the aperture window but on the opposite side of the normal to the array facet. The assumption that the laser is operating on but a few closely spaced array transverse modes is further confirmed by the absence of any observable fine splitting in the longitudinal mode spectrum shown in Fig. 3 and by the increase in the spatial modulation of the near-field intensity pattern when the conjugator is present, as shown in Fig. 4. An alternate explanation for the single-lobe output pattern is given in Ref. 11, in which all of the laser's array modes are assumed to be operating but locked together in phase. However, if this were true then the near-field pattern would lack the spatial modulation clearly seen in Fig. 4.

In summary, we have presented a technique for obtaining stable, near-diffraction-limited output from a high-power laser-diode array. Because the laser emits only a small fraction of its output into the conjugator, we envisage that the output power can be significantly increased without damaging the conjugator. The ability of the phase conjugator to feed light back to precisely the high-gain region of the laser should permit the extension of this technique to much larger arrays or to more-complicated, higher-power diode-laser structures, and this is the current direction of our investigations.

This research was supported in part by the University Research Initiative for the Integration of Optical Computing (U.S. Air Force Office of Scientific Research grant AFOSR-90-0133) and by the National Center for Integrated Photonics Technology. We thank C. Warde for the barium titanate crystal.

## References

1. G. R. Hadley, J. P. Hohimer, and A. Owyong, *IEEE J. Quantum Electron.* **QE-23**, 765 (1987).
2. J. M. Verdiell and R. Frey, *IEEE J. Quantum Electron.* **26**, 270 (1990).
3. F. X. D'Amato, E. T. Siebert, and C. Roychoudhuri, *Appl. Phys. Lett.* **55**, 816 (1989).
4. J. R. Leger, M. L. Scott, and W. B. Veldkamp, *Appl. Phys. Lett.* **52**, 1771 (1988).
5. C. J. Chang-Hasnain, J. Breger, D. R. Scribes, W. Streifer, J. R. Whinnery, and A. Dienes, *Appl. Phys. Lett.* **50**, 1465 (1987).
6. L. Goldberg and J. F. Weller, *Appl. Phys. Lett.* **51**, 871 (1987).
7. L. Goldberg and J. F. Weller, *Electron. Lett.* **25**, 112 (1989).
8. S. MacCormack and R. W. Eason, *Opt. Lett.* **16**, 705 (1991).
9. J. Feinberg, *Opt. Lett.* **7**, 486 (1982).
10. L. Goldberg, H. F. Taylor, J. F. Weller, and D. R. Scribes, *Appl. Phys. Lett.* **46**, 236 (1985).
11. C. J. Chang-Hasnain, A. Dienes, J. R. Whinnery, W. Streifer, and D. R. Scribes, *Appl. Phys. Lett.* **54**, 484 (1989).

# Spatial shape of the dc electric field produced by intense light in glass

Vince Dominic and Jack Feinberg

Departments of Electrical Engineering and Physics, University of Southern California, Los Angeles, California 90089-0484

Received December 11, 1992

A light beam and its second harmonic can create a semipermanent dc electric field inside glass. This dc electric field is responsible for the unexpected production of second-harmonic light in the glass. We determine the transverse spatial shape of this photoinduced dc field inside a bulk sample of germanium-doped fused-silica glass.

There has been a considerable effort since 1986 to understand how an apparently centrosymmetric material such as a glass fiber<sup>1</sup> or a bulk glass sample<sup>2</sup> can act as a frequency doubler. We now know that the incident light creates a dc electric field inside the glass, breaking its inversion symmetry.<sup>3-6</sup> This photoinduced dc electric field acts through the symmetry-allowed third-order susceptibility  $\bar{\chi}^{(3)}$  of the glass to produce the required second-order nonlinearity  $\bar{\chi}^{(2)}$ ,

$$\bar{\chi}^{(2)}(-2\omega; \omega, \omega) = 3\bar{\chi}^{(3)}(-2\omega; \omega, \omega, 0) \cdot \mathbf{E}_{dc}, \quad (1)$$

where  $\mathbf{E}_{dc}$  is the photoinduced dc electric field. The experiments of Mizrahi *et al.*<sup>4</sup> elegantly demonstrate that the polarization properties of  $\bar{\chi}^{(2)}$  obey Eq. (1) as long as  $\chi_{xxxx}^{(3)} = 3\chi_{xxyy}^{(3)}$ , which is true for nondispersive materials.

Here we report a measurement of the transverse spatial shape of the photoinduced dc electric field. We use the polarization properties of  $\bar{\chi}^{(2)}$  to map the spatial shape of the dc electric field  $\mathbf{E}_{dc}$ . Unfortunately, the finite size of our probing beam smears out the finer details of the induced field. Although our spatial map lacks fine resolution, it does clearly show the symmetry of the dc field. With this dc field we find excellent agreement between our predictions and our measurements.

We performed our experiments not in glass fibers but in germanium-doped fused-silica optical fiber preforms.<sup>7</sup> Bulk samples offer several advantages over optical fibers: there are no modal constraints; we can probe regions adjacent to the original focal spot; and we can perform many experiments, each in virgin material, by simply translating the sample between experiments. We confined our experiments to the core region of the preform, because the cladding region was birefringent. In contrast, linearly polarized light transmitted through the core region maintained its polarization to better than 3000:1, regardless of orientation.

Our laser was a mode-locked and *Q*-switched Nd:YAG operating at  $\lambda = 1.064 \mu\text{m}$ . A lithium triborate crystal frequency doubled some of infrared light to produce a green beam collinear with the infrared beam. We controlled the power levels of these two colors independently, using two harmonic wave plates and a vertically oriented polarizer. A

25-mm focal-length achromatic lens focused both colors into the glass sample. Even though we took special precautions (a noncritically phase-matched doubling crystal and an achromatic lens), in general the two colors focused at slightly different spots. However, by rotating the achromatic lens we could almost perfectly overlap the infrared and green beams (to within  $0.5 \mu\text{m}$ ) inside the sample.

Typically, we irradiated our 3-mm-thick glass samples with 3 W of average infrared power and 1 mW of average green power for a period of 10–60 min. The laser was *Q* switched at 1 kHz and mode locked at 76 MHz, with  $\sim 23$  mode-locked pulses [each  $\sim 100$  ps (FWHM) long] inside the 300-ns (FWHM) *Q*-switch envelope. The beam waists ( $1/e^2$  of intensity radius) were  $9.7 \mu\text{m}$  for the infrared and  $7.4 \mu\text{m}$  for the green, and the resulting peak intensities were  $4.4 \times 10^{11}$  and  $3.6 \times 10^8 \text{ W/cm}^2$ , respectively.

After seeding, we studied the frequency-doubling ability of our glass samples by permanently blocking the incident green beam and reducing the power of the infrared beam (now used as a reading beam) to avoid infrared-induced erasure. We recollimated light coming from the sample and then separated the transmitted infrared reading beam from the sample-generated second-harmonic green beam by using a harmonic beam splitter, a hot mirror, a BG40 absorption filter, and a  $0.532-\mu\text{m}$  interference filter. The

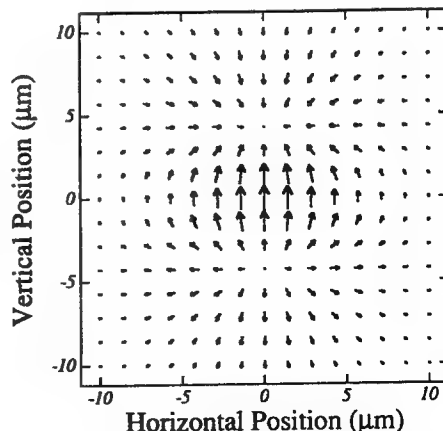


Fig. 1. The dc electric field produced from the charge distribution given by Eq. (2) below. With this dc field shape we successfully predicted the results of six experiments.

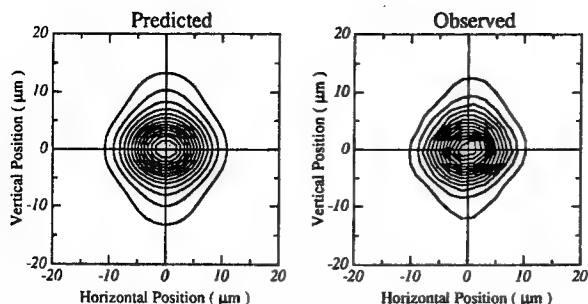


Fig. 2. Comparison of the predicted and observed second-harmonic signals for the case of a vertically oriented reading beam probing different regions of the photoinduced dc field and viewing through a vertically oriented polarizer.

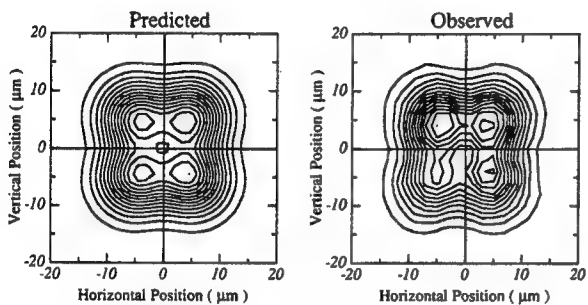


Fig. 3. Same as Fig. 2, except here we flipped both the reading-beam polarization and the analyzing polarizer to horizontal. The contour plots show a four-peaked distribution. The peaks are imperfectly resolved because of the finite size of the probing beam.

green light was detected by a photomultiplier tube. We could alter the polarization of the reading infrared beam with a wave plate ( $\lambda/2$  at  $1.064 \mu\text{m}$ ) in front of the achromatic focusing lens, and we could measure the polarization of the generated green beam with an analyzing polarizer placed immediately after the recollimating objective.

In an isotropic material Eq. (1) shows that the measured signal is proportional to only the vertical component  $\hat{y} \cdot \mathbf{E}_{dc}$  of the dc electric field if the infrared reading beam polarization and the green analyzer polarization are both vertical. If we flip both the reading polarization and the analyzer polarization to be horizontal, then the measured second-harmonic signal is proportional to only the horizontal component  $\hat{x} \cdot \mathbf{E}_{dc}$  of the dc field. By translating the sample we can probe the variation of  $\hat{x} \cdot \mathbf{E}_{dc}$  and  $\hat{y} \cdot \mathbf{E}_{dc}$  in the  $x$ - $y$  plane. We perform two such spatial scans, one for each transverse component of the dc field.

Because the original writing beams were vertically polarized, we expect vertical charge separation inside the glass. We guess a final charge distribution:

$$\rho(x, y) = (\rho_0 y / w) \exp[-(x^2 + y^2)/w^2], \quad (2)$$

which is the vertical derivative of a cylindrically symmetric Gaussian function of width  $w$ . The charge density  $\rho_0$  is unspecified. We choose the parameter  $w = 4.5 \mu\text{m}$  to match our data. Figure 1 shows the dc electric field caused by such a charge distribution. We note that a charge density of  $\sim 10^{14}$  electrons/ $\text{cm}^3$  produces an electric-field strength of

$10^4 \text{ V/cm}$ . (Fields of this size are induced in fibers.<sup>5</sup>) We performed many experiments, over a range of writing-beam powers (infrared,  $0.5 - 4 \text{ W}$ ; green,  $0.1 - 40 \text{ mW}$ ), and found that the dc field was always shaped as shown in Fig. 1.

Ideally, the probe beam should be infinitely small in the mapping experiments, but ours is not. It is a simple matter, however, to use the guessed dc field shown in Fig. 1 and the known size of our probing beam to predict the results of the field-mapping measurements. Figure 2 gives a side-by-side comparison of the predicted and the observed signal for the case of a vertically polarized probe and a vertically oriented analyzer. Figure 3 shows the corresponding comparison for the case of a horizontally polarized probe and a horizontal analyzer. The

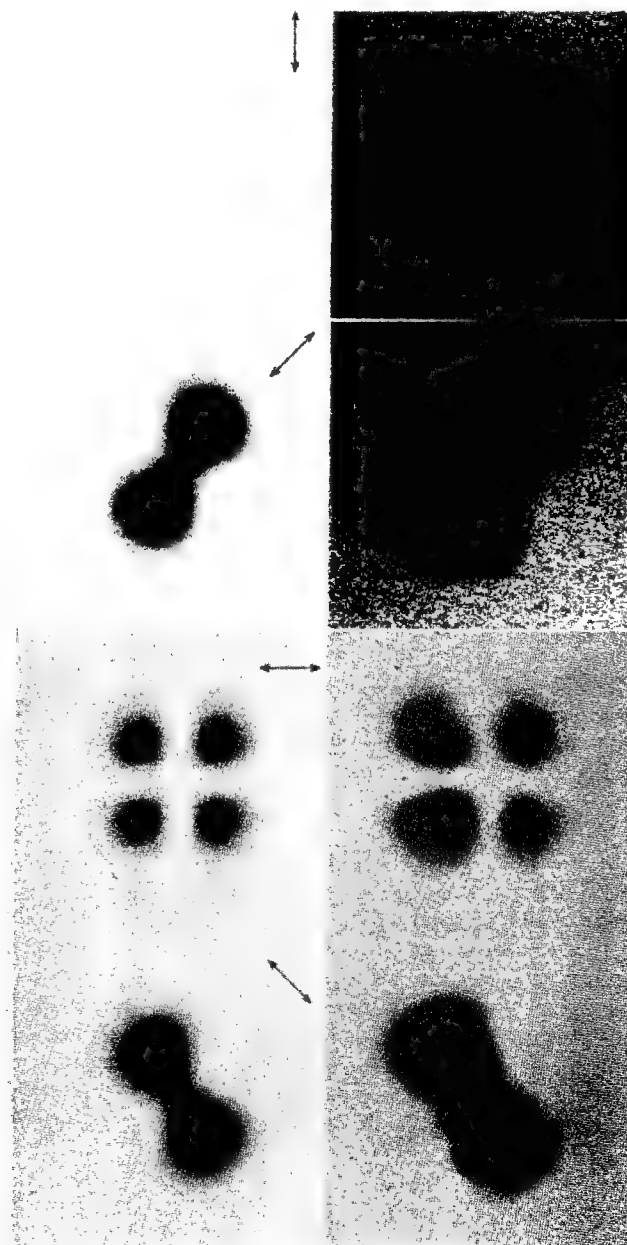


Fig. 4. Photographs of the observed and predicted far-field mode patterns. We oriented the analyzing polarizer horizontally and photographed the far-field pattern of generated green light. The arrow indicates the reading beam's polarization.

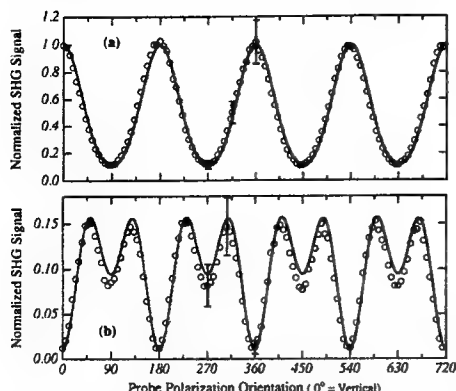


Fig. 5. Comparison of the observed (circles) and predicted (curves) second-harmonic signals versus the reading beam's polarization using either (a) a vertical analyzer or (b) a horizontal analyzer.

measured ratio of the maximum signal using vertical polarization to the maximum signal using horizontal polarization is 8.3, while the computed ratio is 8.0. The agreement between theory and experiment is quite good both for the spatial shape and for the relative strength of the signals. We believe that the slight asymmetry in the experimental data of Fig. 3 is caused by the not-quite-perfect overlap of the writing beams. From the agreement between the theoretical prediction and the observed signal, we conclude that Fig. 1 represents the optically induced dc field quite well.

The far-field mode technique, described by Driscoll and Lawandy,<sup>6</sup> offers an elegant method to confirm this field shape. In contrast to our field-mapping scans, their technique works best when the probe beam is much larger than the dc field pattern. We performed such far-field mode measurements by simply replacing the photomultiplier tube with a CCD camera and recording the shape of the far-field mode pattern of the generated second-harmonic signal. We observed the mode patterns through either a vertically or a horizontally oriented analyzer. Figure 4 shows a comparison between the theoretically predicted far-field mode shape and the observed mode shape using a horizontal analyzer and with various polarizations of the reading beam. We also calculated the far-field mode pattern by taking the Fourier transform of the near field produced by the polarization density  $\mathbf{P}(2\omega) = 3\epsilon_0\tilde{\chi}^{(3)} : \mathbf{E}_\omega\mathbf{E}_\omega\mathbf{E}_{dc}$ , where  $\epsilon_0$  is the permittivity of free space,  $\mathbf{E}_\omega$  is the optical infrared field envelope, and  $\mathbf{E}_{dc}$  is the electric-field shape. Note that the agreement shown in Fig. 4 is quite good. We performed a more complete comparison between theory and experiment by slowly rotating the polarization of the reading beam and videotaping the resulting green far-field mode patterns. We simultaneously displayed, on a split screen, the calculated and measured mode patterns, which agreed in all important aspects.

There is one complication worth discussing. The far-field mode shapes depended on the intensity of the writing beams. At lower writing intensities the charges did not separate so far in the vertical direc-

tion in a given amount of time, and so they produced a more spatially compact dc field. Reading this compact field with a vertical analyzer then produced a far-field pattern with two lobes separated vertically. At higher writing intensity, or with a longer exposure time, the charges separated further, producing a vertically elongated single lobe pattern.

To confirm further the field shape shown in Fig. 1, we launched the infrared reading beam into the center of the dc field pattern and measured the generated signal strength while slowly rotating the reading beam's polarization. Using Eq. (1), the condition  $\chi_{xxxx}^{(3)} = 3\chi_{xxyy}^{(3)}$ , the known size of our probing beam, and the field shape shown in Fig. 1, we predicted the dependence of the second-harmonic signal strength on the reading beam's polarization. Figure 5 shows these results, along with the experimentally measured values. We normalized the data taken with the vertical analyzer for the best fit and then used the same normalization factor for the data taken with a horizontal analyzer. Again, the agreement is exceptionally good.

A two-color light beam (fundamental and its second harmonic) induces a dc electric field inside a glass fiber or a bulk glass sample. This field permits second-harmonic generation in an originally centrosymmetric material. By scanning a probe beam across the field distribution and using simple polarization relationships, we map out the dc electric field. We then invent a simple charge distribution whose dc electric field agrees with the observed dc field. This charge distribution (the derivative of a Gaussian) predicts not only our spatial scanning results but also the generated far-field mode patterns and the dependence of the generated signal on the reading beam's polarization.

This research was supported by grant F49620-92-J-0022 from the U.S. Air Force Office of Scientific Research. Vince Dominic acknowledges fellowship support from the Joint Services Electronics Program.

## References

1. U. Österberg and W. Margulis, *Opt. Lett.* **11**, 516 (1986); **12**, 57 (1987).
2. N. M. Lawandy and M. D. Selker, *Opt. Commun.* **77**, 339 (1990); M. D. Selker and N. M. Lawandy, *Opt. Commun.* **81**, 38 (1991).
3. R. H. Stolen and H. W. K. Tom, *Opt. Lett.* **12**, 585 (1987).
4. V. Mizrahi, Y. Hibino, and G. Stegeman, *Opt. Commun.* **78**, 283 (1990).
5. A. Kamal, M. L. Stock, A. Szpak, C. H. Thomas, D. A. Weinberger, M. Frankel, J. Nees, K. Ozaki, and J. Valdmanis, in *Annual Meeting*, Vol. 15 of 1990 OSA Technical Digest Series (Optical Society of America, Washington, D.C., 1990), paper PD25.
6. T. J. Driscoll and N. M. Lawandy, in *Conference on Lasers and Electro-Optics*, Vol. 12 of 1992 OSA Technical Digest Series (Optical Society of America, Washington, D.C., 1992), paper JTUA4.
7. Ensign-Bickford Optical Technologies, Inc., 6737 Valjean Avenue, Van Nuys, California 91406.

# Growth rate of second-harmonic generation in glass

Vince Dominic and Jack Feinberg

Departments of Electrical Engineering and Physics, University of Southern California, Los Angeles, California 90089-0484

Received July 13, 1992

We study the growth rate of the light-induced second-order nonlinearity in germanium-doped optical fiber preforms. We seed the glass with both infrared light and green light (Nd:YAG and doubled Nd:YAG) to create the second-order nonlinearity and measure its formation rate while varying the intensity of either the fundamental or the second-harmonic seeding beams. We find that the formation rate varies as a power law of the intensities, but with an exponent larger than predicted by recent models.

Because the core of an optical fiber is macroscopically centrosymmetric, second-harmonic generation is not expected to occur. However, in 1986 Österberg and Margulis reported rather efficient (5%) second-harmonic generation inside a germanium-doped optical fiber that had been illuminated by intense infrared light for many hours.<sup>1</sup> Stolen and Tom<sup>2</sup> showed that by injecting both infrared and green light into the fiber, the preparation time of the fiber could be shortened from many hours to just a few minutes.

What breaks the inversion symmetry of the glass? Recent experiments indicate that the incident light gradually produces a spatially periodic<sup>3</sup> dc electric field in the glass.<sup>4,5</sup> This dc electric field induces a second-order nonlinearity:

$$\chi^{(2)}(-2\omega; \omega, \omega) = 3\chi^{(3)}(-2\omega; \omega, \omega, 0)E_{dc}. \quad (1)$$

Phase matching can be achieved if the dc field ( $E_{dc}$ ) periodically changes direction along the fiber length. Many theories have been postulated to explain the origin of this spatially periodic dc field.<sup>2,6-9</sup> However, these different models predict different dependencies of the growth rate of the dc field on the intensity of the injected optical beams. To discriminate among these models we measured the dependence of the growth rate of the second-harmonic signal on the intensity of the injected light beams.

We found it simpler to perform our experiments in glass fiber preforms instead of in the fibers themselves. Our preform sample had an outer diameter of 12.5 mm and a 3.4-mm-diameter germanium-doped core.<sup>10</sup> The germanium concentration decreased abruptly at the core-cladding interface and then fell exponentially with distance, with occasional rings of higher index. These rings result from the fabrication process, and they aberrate optical beams transmitted through them. We performed our experiments far enough away from the core to avoid these aberrations. We worked in the cladding region so that we could fit many more experiments into one rotation of the sample. We verified that the dependence of the growth rate on intensity was the same in the core region as in the cladding region of the preform.

Before starting each experiment we rotated the sample to a new, unused portion of the preform. Because the doping was cylindrically symmetric, the germanium density remained constant from experiment to experiment.

We used a seeding technique<sup>2</sup> in which we focused both the fundamental and some externally generated second-harmonic light into the sample. (In the absence of a second-harmonic seeding beam no second-harmonic generation was observed from the preform.) A mode-locked and Q-switched Nd:YAG laser had a Q-switch repetition rate of 1 kHz, with ~23 mode-locked pulses under the 300-ns Q-switch pulse envelope. Its 1.064- $\mu\text{m}$  light was doubled in a noncritically phase-matched lithium triborate crystal to produce second-harmonic light collinear with the fundamental light. We controlled the power levels of the fundamental and second-harmonic seeding beams independently with two harmonic wave plates. The paths of our seeding fundamental ( $I_{\omega}$ ) and second-harmonic ( $I_{2\omega}$ ) beams were never separated to ensure that their relative phase remained stable during seeding.<sup>11</sup> We checked this phase stability and found that it exceeded 4 h.

A spinning wheel (~5 Hz) in front of the sample periodically blocked the green seeding beam (with both a cold mirror and an RG780 absorption filter), so that any green light generated in the sample could be measured. Light reflected from the cold mirror triggered the data-acquisition system. The power in each incident infrared and green pulse was monitored with photodiodes, and the generated green light was monitored with a photomultiplier. All these detectors were carefully checked for linearity over their range of detected intensities. A 25-mm focal-length achromatic lens focused the infrared and the green to the same location within the glass preform. The infrared and green beams were measured to be 9.7 and 7.4  $\mu\text{m}$  (radius at  $1/e^2$  of intensity), respectively, at the focus.

We acquired two types of data sets: (1) we held the infrared power constant and varied the green power level, and (2) we held the green constant and varied the infrared power level. For both types of experiment, we measured the early-time growth of the

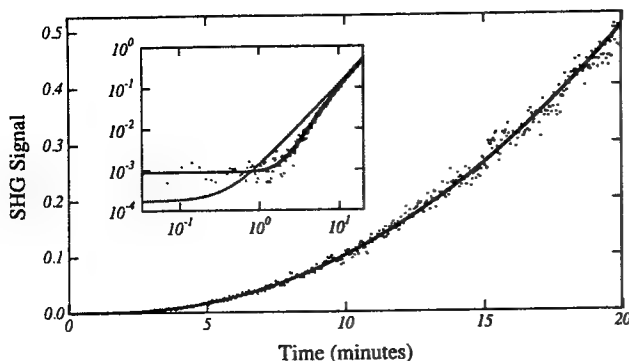


Fig. 1. Quadratic growth of the second-harmonic generation (SHG) signal during seeding. The solid curve is a fit using Eq. (3). The inset shows the same data plotted log-log with the best fits using Eq. (2) (dotted curve) and Eq. (3) (solid curve).

second-harmonic signal and fitted its dependence to a quadratic function of time, as shown in Fig. 1. We fitted the data up to the point where it began to saturate, i.e., where the growth was no longer quadratic in time, which could take longer than 40 min at low infrared and green intensities. We performed fits using two different fitting functions:

$$I_{2\omega}^{\text{produced}} = \Gamma t^2 + \text{offset}, \quad (2)$$

$$I_{2\omega}^{\text{produced}} = \Gamma \{t - \tau[1 - \exp(-t/\tau)]\}^2 + \text{offset}, \quad (3)$$

where offset is a small dc voltage produced by our detection system. We found that Eq. (3) fitted the data better than did Eq. (2), especially at early times, as shown in the inset of Fig. 1. We derived Eq. (3) by assuming that an initially unoccupied level must first be populated (with a time constant  $\tau$ ) before the internal dc electric field can begin to form. This idea was inspired by recent suggestions that metastable levels may be involved in the induced second-harmonic generation effect.<sup>12,13</sup> We found experimentally that  $\tau$  varied from three minutes at low intensities to less than a second at high intensities.

For all feasible power levels, we determined the growth rate  $\Gamma$  and then fitted it to a power law in the optical intensities: either  $AI_{\omega}^x$  for the infrared or  $BI_{2\omega}^y$  for the green. Figure 2 shows the dramatic variation of  $\Gamma$  with the infrared seeding intensity and the less dramatic variation of  $\Gamma$  with the green seeding intensity. Figure 3 shows the results of accumulating many such power-law dependencies; we plot the exponent  $x$  in  $\Gamma = AI_{\omega}^x$  as a function of the green seeding intensity in Fig. 3(a), and the exponent  $y$  in  $\Gamma = BI_{2\omega}^y$  versus infrared seeding intensity in Fig. 3(b). We found that the exponent  $y$  varied from  $y = 3.5$  at low infrared intensity to  $y = 2.5$  at high infrared intensity. In contrast, the exponent  $x$  varied from  $x = 12.5$  at low green seeding intensity to  $x = 8$  at high green seeding intensity.

How do our data compare with the recent theories of second-harmonic generation? The models of Dianov *et al.*<sup>8</sup> and Anderson *et al.*<sup>9</sup> postulate a spatially oscillating photogalvanic ( $j_{\text{pg}}$ ) current to explain the generation of the dc electric field. At early times the current flows unchecked and the dc electric field grows linearly in time:  $E_{\text{dc}} \propto j_{\text{pg}}t$ . In

our experiments we measured the second-harmonic signal power, which is proportional to  $|\chi^{(2)}|^2$  of Eq. (1), so that according to the current models,<sup>8,9</sup> we measured  $|j_{\text{pg}}|^2$ . The predicted intensity dependencies for our parameter  $\Gamma$  from the model of Ref. 8 is then

$$\Gamma \propto \{I_{2\omega} I_{\omega}^2\} I_{\omega}^2, \quad (4)$$

while from the model of Ref. 9 it is

$$\Gamma \propto \{I_{2\omega} I_{\omega}^2 (\eta_4 I_{\omega}^4 + \eta_4 I_{\omega}^2 I_{2\omega} + I_{2\omega}^2)\} I_{\omega}^2. \quad (5)$$

In relations (4) and (5) the terms inside the braces are proportional to  $|j_{\text{pg}}|^2$ , while the reading process itself imparts the additional quadratic variation ( $I_{\omega}^2$ ) to the measured growth rate  $\Gamma$ . This extra quadratic variation is not normalized out of the data displayed

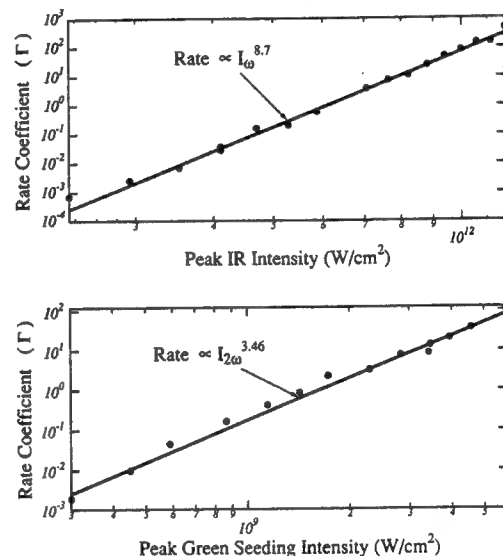


Fig. 2. (a) Dependence of the rate  $\Gamma$  on the infrared seeding power, with the green seeding power held fixed at 6 mW. (b) The dependence of the rate  $\Gamma$  versus the green seeding power, with the infrared power held constant at 3 W.

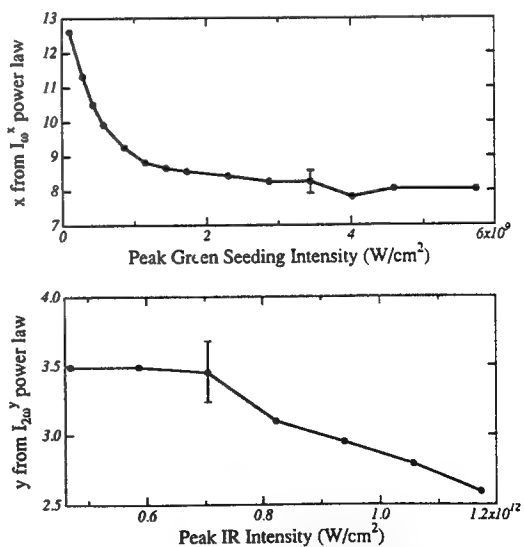


Fig. 3. (a) Dependence of the infrared power-law exponent  $x$  on the green seeding set-point intensity. (b) Dependence of the green power-law exponent  $y$  on the infrared set-point intensity.

in Figs. 2 and 3. If we include this built-in quadratic dependence on  $I_\omega$ , then the anisotropic photoionization model<sup>9</sup> predicts a power law  $\Gamma \propto I_\omega^x$  with the exponent in the range of  $x = 4-8$ . Another model<sup>8</sup> gives  $x = 4$ . The trend in Fig. 3 is consistent with the model of Anderson *et al.*, in that the power-law exponent drops to a lower value as the green seeding intensity is increased. However, even at the highest obtainable green intensity we still observe  $x = 8$ . These data clearly indicate a higher-order dependence on  $I_\omega$  than predicted by either model.

There have been reports<sup>14-16</sup> of the intensity dependence of seeded second-harmonic generation in germanium-doped fused silica. Kamal *et al.*<sup>16</sup> performed experiments similar to the ones reported here; however, their experiments were carried out in a specially grown fiber. If their data are analyzed with the rate parameter  $\Gamma$  discussed here, they observed  $x \approx 4$  for the dependence of the rate on infrared intensity and  $y \approx 3$  for the dependence on green intensity. Their observed dependence of the rate on the green intensity agrees with ours, but their infrared dependence is quite different.

Lawandy and Selker<sup>15</sup> reported a distinct infrared intensity threshold below which no second-harmonic generation was observed in samples that had been seeded for only 20 min. Our data also show a dramatic dependence of the second-harmonic effect with the infrared intensity, but at intensities 100 times greater than the threshold cited in Ref. 15. Rather than observing a threshold intensity below which no effect occurs, we find that at low infrared intensities the formation rate of the dc electric field simply becomes extremely slow.

Our observed green intensity scaling data are not in gross disagreement with the anisotropic photoionization model of Anderson *et al.*<sup>9</sup> However, the infrared scaling data require more infrared photons than this model postulates. We examined our experiment to see if systematic errors caused the higher-than-expected  $I_\omega$  variation. First we checked whether the beam spot size entering the focusing lens changed as we adjusted the infrared power. We measured the infrared beam profile and found no systematic variation of the beamwidth to within experimental error (0.6%). Additionally, we checked to see if self-focusing or thermal lensing changed the focal spot size as the power was varied, and we found no variation. We intentionally displaced the infrared beam from the green seeding beam by  $\sim 6 \mu\text{m}$  at the focus to determine whether thermal beam steering contributed to the intensity dependence and found that although the infrared power-law exponent  $x$  was lower with the beams offset, it was still within the error bar of Fig. 3(a).

Because the diameters of our tightly focused optical beams change as they propagate through the glass preform, their intensity varies in both the transverse directions and along the propagation direction and therefore so should the growth rate. However, we performed numerical calculations and found that the measured signal should still grow quadratically in time. Because only the most intense part of the beam contributes to the signal at early times, the

intensity scaling laws of the early-time growth rate are not affected. Another complication is that our laser is  $Q$  switched and mode locked, so that there is a range of peak intensities present under the envelope, and our measured rate is an average over all these peak intensities. This averaging over intensities could mask an even more dramatic dependence of the generation rate on optical intensity.

In summary, we measured the buildup rate of the second-harmonic signal in germanium-doped fused-silica optical fiber preforms. The second-harmonic signal rises quadratically in time. The rate coefficient increases with the intensity of the infrared seeding beam as  $I_\omega^{8-12}$  and with the intensity of the green seeding beams as  $I_{2\omega}^{2.5-3.5}$ . Both the  $I_\omega$  and  $I_{2\omega}$  power laws are faster than predicted by the model of Dianov *et al.*<sup>8</sup> The variation of the rate with the intensity of the green seeding light seems to agree with the model of Anderson *et al.*<sup>9</sup> reasonably well. However, the variation of the rate with the intensity of the infrared seeding light is too rapid to be explained by this model.

We thank Robert M. Pierce for his experimental assistance. Vince Dominic acknowledges fellowship support from the Joint Services Electronics Program, and Jack Feinberg acknowledges research support from the U.S. AFOSR.

## References

1. U. Österberg and W. Margulis, Opt. Lett. **11**, 516 (1986); **12**, 57 (1987).
2. R. H. Stolen and H. W. K. Tom, Opt. Lett. **12**, 585 (1987).
3. A. Kamal, D. A. Weinberger, and W. H. Weber, Opt. Lett. **15**, 613 (1990).
4. V. Mizrahi, Y. Hibino, and G. Stegeman, Opt. Commun. **78**, 283 (1990).
5. A. Kamal, M. L. Stock, A. Szpak, C. H. Thomas, D. A. Weinberger, M. Frankel, J. Nees, K. Ozaki, and J. Valdmanis, in *Digest of Optical Society of America Annual Meeting* (Optical Society of America, Washington, D.C., 1990), paper PD25.
6. N. M. Lawandy, Opt. Commun. **74**, 180 (1989).
7. N. B. Baranova, A. N. Chudinov, and B. Ya. Zel'dovich, Opt. Commun. **79**, 116 (1990).
8. E. M. Dianov, P. G. Kazansky, and D. Yu Stepanov, Sov. J. Quantum Electron. **19**, 575 (1989); Sov. Light-wave Commun. **1**, 247 (1991).
9. D. Z. Anderson, V. Mizrahi, and J. E. Sipe, Opt. Lett. **16**, 796 (1991).
10. The sample was grown by Ensign-Bickford Optical Technologies, Inc., using a hybrid VAD:OVD method. The core was doped to give  $\Delta n = 4.5 \times 10^{-3}$ .
11. D. M. Krol, M. M. Broer, K. T. Nelson, R. H. Stolen, H. W. K. Tom, and W. Pleibel, Opt. Lett. **16**, 211 (1991).
12. I. C. S. Carvalho, W. Margulis, and B. Lesche, Opt. Lett. **16**, 1487 (1991).
13. T. J. Driscoll and N. M. Lawandy, Opt. Lett. **17**, 571 (1992).
14. A. Krotkus and W. Margulis, Appl. Phys. Lett. **52**, 1942 (1988).
15. N. M. Lawandy, Phys. Rev. Lett. **65**, 1745 (1990); M. D. Selker and N. M. Lawandy, Opt. Commun. **81**, 38 (1991).
16. A. Kamal, R. W. Terhune, and D. A. Weinberger, Proc. Soc. Photo-Opt. Instrum. Eng. **1516**, 137 (1991).

# Intensity dependence of the photovoltaic effect in barium titanate

R. S. Cudney

Department of Physics and Department of Electrical Engineering, University of Southern California,  
Los Angeles, California 90089-0484

R. M. Pierce

Department of Physics, University of Southern California, Los Angeles, California 90089-0484

G. D. Bacher

Department of Physics and Department of Electrical Engineering, University of Southern California,  
Los Angeles, California 90089-0484

Daniel Mahgerefteh

Department of Physics, University of Southern California, Los Angeles, California 90089-0484

Jack Feinberg

Department of Physics and Department of Electrical Engineering, University of Southern California,  
Los Angeles, California 90089-0484

Received December 27, 1992; revised manuscript received April 2, 1992

A crystal of  $\text{BaTiO}_3$  illuminated by a spatially periodic light intensity pattern will exhibit both uniform and spatially periodic photovoltaic currents. The modulated part of the intensity produces a spatially periodic photovoltaic current, which creates a spatially periodic electric field in the crystal. This field, measured by two-beam coupling, is spatially in phase with the light pattern and increases monotonically with intensity, saturating at  $\sim 450 \text{ V/cm}$ . The spatially uniform photovoltaic current produced by the average light intensity creates a spatially uniform electric field, which is surprisingly small ( $\sim 10 \text{ V/cm}$ ) across a nominally open-circuited  $\text{BaTiO}_3$  crystal at high optical intensity. We explain the observed intensity dependence of two-beam coupling by proposing that photovoltaic currents arise with different strengths from at least two trap levels in the crystal.

## 1. INTRODUCTION

Light can cause electric charge to move in a preferential direction in crystals that lack inversion symmetry. In general the direction of this photovoltaic current depends on the direction of polarization of the incident light beam and the symmetry group of the crystal. Let a monochromatic light wave with an optical electric field  $\mathbf{E}_{\text{opt}}(\mathbf{x}, t) = \text{Re}[\mathbf{E}_{\text{opt}}(\mathbf{x})\exp(-i\omega t)]$  be incident upon a crystal lacking a center of symmetry. In general the magnitude and the direction of the photovoltaic current density  $\mathbf{j}^{\text{pg}}$  are related to the complex electric-field envelope  $\mathbf{E}_{\text{opt}}(\mathbf{x})$  by<sup>1</sup>

$$\mathbf{j}^{\text{pg}}(\mathbf{x}) = \overline{\beta} \cdot \mathbf{E}_{\text{opt}}(\mathbf{x}) \mathbf{E}_{\text{opt}}^*(\mathbf{x}), \quad (1)$$

where  $\overline{\beta}$  is a phenomenological, third-rank photovoltaic tensor that must have the same symmetry as the point group of the crystal and where, since the current is a real quantity,  $\beta_{\lambda\mu\nu} = \beta_{\lambda\nu\mu}^*$ . Currents obeying Eq. (1) have been detected in numerous ferroelectric crystals, such as  $\text{LiNbO}_3$ ,  $\text{LiTaO}_3$ ,<sup>2,3</sup> and  $\text{BaTiO}_3$ ,<sup>4</sup> and even in nonferroelectric crystals such as  $\text{Bi}_{12}\text{SiO}_{20}$ ,  $\text{GaAs}$ , and  $\text{Te}$ .<sup>2,3</sup>

For the particular case of light beams polarized along only one of the optical axes of a ferroelectric crystal, the

product of the two optical electric fields in Eq. (1) can be expressed in terms of the intensity of the incident light. In this case Glass *et al.*<sup>5</sup> found that the observed  $\mathbf{j}^{\text{pg}}$  and the absorption  $\alpha$  of a lithium niobate crystal were related by

$$\mathbf{j}^{\text{pg}}(I) = \mathbf{p}I = \hat{c}\kappa\alpha I. \quad (2)$$

Here  $\hat{c}$  is the unit vector in the direction of the permanent polarization of the ferroelectric crystal, and  $\kappa$ , now known as the Glass constant, is a proportionality factor that was found to be relatively independent of the light intensity. This photovoltaic current was attributed to an asymmetry of the potential well holding the trapped charge carrier, which causes charges located in trap sites to move preferentially in a given direction on excitation or on recombination.

It has been observed that in some photorefractive crystals, such as barium titanate, the absorption coefficient  $\alpha$  of the crystal changes appreciably with intensity.<sup>6</sup> In view of this relation a natural question arises: How can Eq. (2) be modified to account for this light-induced absorption? The light-induced absorption of barium titanate has been explained quite successfully by assuming

photoexcitation of charge carriers from at least two different kinds of trap sites located in the band gap of the crystal, each having its own absorption cross section.<sup>7,8</sup> In like manner, we suggest that the charge excited from different kinds of trap sites makes different contributions to the total photogalvanic current. Since both the absorption and the photogalvanic current from each kind of trap site are proportional to the number of those trap sites that are occupied, and since the density of occupied trap sites is intensity dependent, the total photogalvanic effect should have the form

$$\mathbf{j}^{\text{pg}}(I) = \mathbf{p}(I)I = \hat{c}\kappa(I)\alpha(I)I, \quad (3)$$

where now both the absorption  $\alpha(I)$  and  $\kappa(I)$  are intensity dependent.

Although the current densities produced by the photogalvanic effect are typically small ( $\sim 10^{-9}\text{--}10^{-13} \text{ A/cm}^2$ ), they can noticeably affect the coupling of light beams in photorefractive crystals. Here we study the photogalvanic effect, using two-beam coupling in barium titanate. In Section 2 we derive expressions for beam coupling in a photorefractive crystal in the presence of the photogalvanic effect. We extend the usual band-conduction model to include multiple levels of trap sites, with each level contributing its own photogalvanic current. Section 3 describes our photorefractive coupling experiments in barium titanate. We show how the measured coupling of light beams depends on the total light intensity and on the magnitude of the grating wave vector, and we fit the data to a model with two trapping levels. In Appendix A we treat the more general case of photorefractive beam coupling with arbitrary beam polarizations and crystal configurations.

## 2. THEORY

### Photogalvanic Currents from Multiple Levels

Consider the case with only one incident light polarization and electrical currents only along  $\hat{c}$ , the direction of permanent polarization of a ferroelectric  $\text{BaTiO}_3$  crystal. Assume that each time a localized charge is optically excited from a trap site there is a tendency for it to move a distance  $d^{\text{opt}}$  away from the trap site along the  $+\hat{c}$  axis. There may also be a tendency for charges to move a distance  $d^{\text{therm}}$  on thermal excitation as well as a distance  $d^{\text{rec}}$  on recombination into an empty trap site. If there is only one level of trap sites from which photoexcitation can occur, then the model of Glass *et al.*<sup>5</sup> can be reexpressed in the form

$$\mathbf{j}^{\text{pg}}(I) = e\hat{c}(d^{\text{opt}}sIN^F + d^{\text{therm}}\beta N^F + d^{\text{rec}}\gamma nN^E), \quad (4)$$

where  $e$  is the unit charge;  $s$ ,  $\beta$ , and  $\gamma$ , respectively, are the optical excitation, thermal excitation, and recombination rate constants;  $I$  is the total light intensity; and  $N^F$  and  $N^E$  are the number densities of trap sites that are full or empty of the charge carrier, respectively. At steady state the excitation and the recombination rates of the free charges are balanced, giving

$$n = (sI + \beta)N^F/(\gamma N^E). \quad (5)$$

Combining Eqs. (4) and (5), and using the second law of thermodynamics to make the total current vanish in the ab-

sence of optical excitation, we find that  $d^{\text{therm}} = -d^{\text{rec}}$  and that the total photogalvanic current can be expressed as

$$\mathbf{j}^{\text{pg}}(I) = e\hat{c}sIN^F(d^{\text{opt}} - d^{\text{rec}}) = e\hat{c}sIN^Fd, \quad (6)$$

which involves only optical excitation. Here  $d$  is the effective photogalvanic transport distance, defined by  $d = d^{\text{opt}} - d^{\text{therm}}$ .

If there are multiple levels of trap sites, with each contributing to the photogalvanic effect, then by assuming detailed balance we obtain

$$\mathbf{j}^{\text{pg}}(I) = e\hat{c}I \sum_j d_j s_j N_j^F(I) = \mathbf{p}(I)I, \quad (7)$$

where the subscript  $j$  identifies the trap-site level. With multiple levels the photogalvanic current is no longer linear in the light intensity, because the number densities  $N_j^F(I)$  are, in general, intensity dependent; this makes  $\mathbf{p}(I) = e\hat{c}\sum_j d_j s_j N_j^E(I)$  a function of the light intensity.

### Two-Beam Coupling

Conceptually, the simplest method for measuring the photogalvanic current predicted by Eq. (7) would be to illuminate a crystal uniformly with light and measure any resulting dc current by using electrodes attached to the crystal. However, in practice the photogalvanic current can be measured with more precision and with fewer experimental complications (such as electrode contact potentials) in photorefractive crystals by studying the effect of the photogalvanic current on the coupling of two light beams in the crystal. In a photorefractive crystal, light rearranges charges in the crystal, producing a static electric field. If the light pattern is spatially periodic, as from the interference of two light beams, there will be a component of the resulting static electric field with the same periodicity. This space-charge field alters the refractive index of the crystal by means of the Pockels effect, and this periodic refractive-index pattern can act as a grating to couple the incident light beams. Depending on the relative phase of the space-charge field with respect to the light intensity pattern, the grating can couple the amplitudes or the phases (or both) of the incident light beams.

Consider the case of coupling between two ordinary polarized optical beams, which we call the probe and the reference beams. Using a multiple-level band-conduction model with a single type of charge carrier (holes) and Eq. (7), we show in Appendix A that in the undepleted-pump approximation (for reference intensity much larger than probe intensity) the amplitude of the probe beam,  $E_p(z)$ , will evolve with propagation distance  $z$  according to

$$E_p(z) = E_p(0)\exp(g^{\text{eo}}z), \quad (8)$$

where the electro-optic coupling coefficient  $g^{\text{eo}}$  depends on the magnitude of the grating wave vector  $k_g$  according to

$$g^{\text{eo}}(k_g, I) = \frac{\omega}{2c} n_{\text{ord}}^3 r_{13} \frac{k_B T}{e} \times \frac{\eta(I)[k_g + ik_{\text{drift}}(I)] + ik_{\text{pg}}(I) + ik_{\Delta\text{pg}}(I)}{1 + \{[k_g[k_g + ik_{\text{drift}}(I) - ik_{\text{uniform}}(I)]]/[k_0^2(I)]\}}. \quad (9)$$

In Eq. (9)  $n_{\text{ord}}$  is the ordinary index of refraction,  $r_{13}$  is the appropriate Pockels coefficient, and  $k_B T/e$  is the thermal

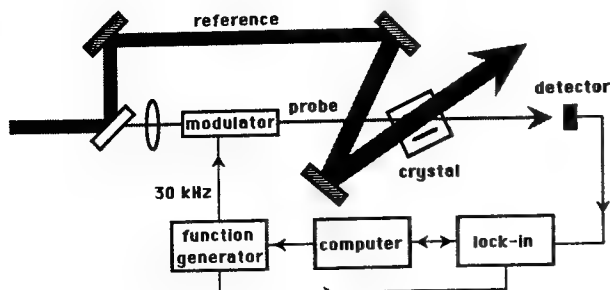


Fig. 1. Experimental setup for measuring the two-beam coupling.

energy per unit charge. The quantities  $k_0(I)$ ,  $k_{\text{drift}}(I)$ ,  $\eta(I)$ ,  $k_{\text{pg}}(I)$ ,  $k_{\Delta\text{pg}}$ , and  $k_{\text{uniform}}(I)$  have complicated intensity dependences, and their analytic expressions are given in Appendix A. However, their physical origin can be described rather simply, as follows:

$k_0(I)$  is the total inverse Debye screening length, which depends on the density of the full and the empty trap sites of all the levels. Since optical excitation redistributes charges among the various levels,  $k_0(I)$  is intensity dependent.

The term  $k_{\text{drift}}(I) = [e/(k_B T)]E_0(I)$  accounts for the drift of charges in any uniform electric field  $E_0(I)$ . This electric field may be externally applied or internally developed, such as by a spatially uniform photogalvanic current, as we discuss below.

The term  $\eta(I)$  is the optical-to-thermal ratio of the charge-excitation rates averaged over all the various trap levels and weighted by their effective number density. At low light intensities the thermal excitation rate dominates, and  $\eta(I)$  tends to zero. At high light intensities the thermal excitation rate can be neglected, and  $\eta(I)$  approaches unity.

The terms  $k_{\text{pg}}(I)$ ,  $k_{\Delta\text{pg}}(I)$ , and  $k_{\text{uniform}}(I)$  all arise from the photogalvanic effect, but each has a slightly different origin, as we show below. Let the total light intensity in the crystal be written as

$$I(z) = I_0(1 + m \cos k_g z), \quad (10)$$

where  $m$  is the modulation of the light interference pattern. Expanding Eq. (7) in a Taylor series around the average light intensity  $I_0$ , we obtain

$$\begin{aligned} j^{\text{pg}}[I(z)] &= \mathbf{p}[I(z)]I(z) \\ &= \mathbf{p}[I_0(1 + m \cos k_g z)]I_0(1 + m \cos k_g z) \\ &= \mathbf{p}(I_0)I_0 + \mathbf{p}(I_0)I_0 m \cos k_g z \\ &\quad + \left( \frac{d\mathbf{p}}{dI} \Big|_{I=I_0} \right) I_0^2 m \cos k_g z \\ &\quad + (\text{terms of higher order in } m). \end{aligned} \quad (11)$$

The first term on the right-hand side of Eq. (11) produces the term  $k_{\text{uniform}}(I)$  in Eq. (9) and represents the effect of spatially uniform photogalvanic currents. The second term produces the term  $k_{\text{pg}}(I)$  and is due to spatially varying optical charge excitation. Finally, the third term produces the term  $k_{\Delta\text{pg}}$  in Eq. (9); it accounts for the spatial variation of the effective photogalvanic coefficient  $\mathbf{p}(I)$  caused by the spatially varying distribution of charges among the various trapping sites. If there were only one

kind of trapping site this term would vanish, since in that case  $\mathbf{p}$  would be independent of intensity.

In the experiments described below we use small beam-crossing angles, so that  $k_g \ll k_0$ . In this case Eq. (9) takes a simpler form:

$$\begin{aligned} g^{\text{eo}}(k_g, I) &= \frac{\omega}{2c} n_{\text{ord}}^3 r_{13} \frac{k_B T}{e} \{ \eta(I)[k_g + ik_{\text{drift}}(I)] \\ &\quad + ik_{\text{pg}}(I) + ik_{\Delta\text{pg}}(I) \}. \end{aligned} \quad (12)$$

### 3. EXPERIMENT

#### Two-Beam Coupling

According to Eq. (8), the amplitude of the probe beam is altered by the real part of the coupling coefficient  $g_R^{\text{eo}} = \text{Re}(g^{\text{eo}})$ , whereas the phase of the probe beam is altered by the imaginary part  $g_I^{\text{eo}} = \text{Im}(g^{\text{eo}})$ . Both the real and the imaginary parts of the coupling coefficient can be measured by two-beam coupling experiments.<sup>9,10</sup> Let the phase of the input probe beam be modulated by a known amplitude  $\mu$  at a frequency  $\Omega$  with an electro-optic modulator, as shown in Fig. 1. The phase modulation dithers the position of the interference pattern. If the frequency  $\Omega$  is large enough, the crystal will not be able to follow these rapid variations, and an average, stationary grating will build up in the crystal. A portion of the reference beam will diffract from the grating and beat with the transmitted phase-modulated probe beam, producing intensity fluctuations at harmonics of  $\Omega$ . For  $\mu \ll 1$ , a coupled-wave analysis gives<sup>10</sup>

$$I_p(\Omega) = 2\mu I_p^0 \exp(g_R l) \sin(g_I l), \quad (13)$$

$$I_p(2\Omega) = (\mu^2/2)I_p^0 [\exp(g_R l) \cos(g_I l) - 1], \quad (14)$$

where  $I_p(\Omega)$  and  $I_p(2\Omega)$  are the magnitudes of the intensity fluctuations at the frequencies  $\Omega$  and  $2\Omega$  and  $I_p^0$  is the intensity that the transmitted probe beam would have if there were no coupling. By measuring  $I_p^0$ ,  $I_p(\Omega)$ , and  $I_p(2\Omega)$  and solving Eqs. (13) and (14), we can obtain  $g_R$  and  $g_I$ . Notice that in Eqs. (13) and (14) we omitted the superscript  $\text{eo}$  on the coupling coefficient  $g$ ; these equations do not depend on the physical origin of the coupling coefficient. In general, there may be processes other than the electro-optic effect that couple the light beams in photorefractive crystals. For example, the different polarizabilities of the full and the empty trapping sites can couple the light beams, as described in Ref. 10. If accurate measurements of the purely electro-optic coupling are to be obtained, then the effects of these other coupling mechanisms must be removed, as they are in the experiments described below.

We measured coupling in a 5.29 mm  $\times$  5.47 mm  $\times$  7.34 mm barium titanate crystal (called FREE) at  $\lambda = 488$  nm by using the phase-modulation technique described above. This crystal has a dark yellow appearance and exhibits marked light-induced absorption.<sup>8</sup> The crystal's  $c$  axis was aligned parallel to the grating wave vector, and the beams were polarized perpendicular to the plane of incidence (ordinary polarization). The diameters of the reference and the probe beams (where the intensity dropped to  $1/e$  of the maximum) were 2.14 and 0.76 mm, respectively, and the power ratio of these two beams was

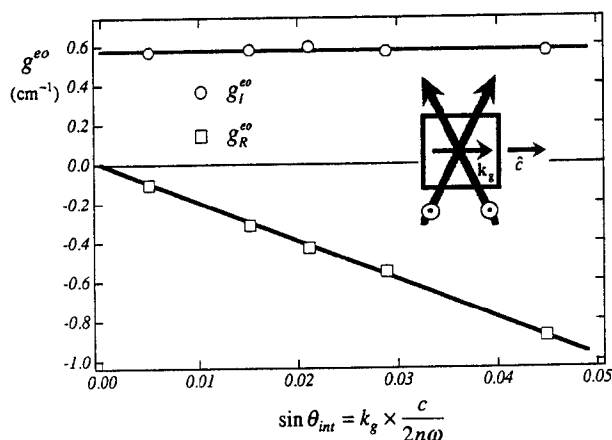


Fig. 2. Imaginary  $g_I^{eo}$  and real  $g_R^{eo}$  parts of the purely electro-optic coupling in the crystal FREE versus  $k_g$  at a fixed, high intensity ( $13 \text{ W/cm}^2$ ).  $\lambda = 488 \text{ nm}$ ,  $T = 17.7 \pm 0.2^\circ\text{C}$ . The inset shows the polarization of the beams and the direction of the grating wave vector.

kept fixed at 570:1. This gives an intensity ratio of 72:1 for these two beams, resulting in a modulation  $m = 0.23$ . The crystal was cemented with silver paint to a copper block, which in turn was immersed in a cuvette filled with water, with the temperature of the whole assembly regulated by a Peltier cooler. Such temperature regulation is required because absorption of the incident light tends to heat the crystal, which changes the thermal excitation rates of the various trapping levels as well as other crystal parameters.

For  $k_g \ll k_0$ , Eq. (12) predicts that the real and the imaginary parts of the electro-optic coupling are

$$g_R^{eo}(k_g) = \frac{\omega}{2c} n_{\text{ord}}^3 r_{13} \frac{k_B T}{e} \eta k_g, \quad (15)$$

$$g_I^{eo} = \frac{\omega}{2c} n_{\text{ord}}^3 r_{13} \frac{k_B T}{e} (\eta k_{\text{drift}} + k_{\text{pg}} + k_{\Delta\text{pg}}). \quad (16)$$

Figure 2 shows both the real and the imaginary parts of the measured electro-optic coupling versus  $k_g$  at a fixed, high optical intensity ( $I = 13 \text{ W/cm}^2$ ). As expected,  $g_R^{eo}$  changes linearly with  $k_g$ , whereas  $g_I^{eo}$  is constant. From the slope of  $g_R^{eo}$  we obtain  $\eta(I)r_{13} = 12 \times 10^{-12} \text{ m/V}$ . Using the crystal parameters given in Ref. (8) and the explicit intensity dependence of  $\eta$  given in Appendix A for a two-level model,<sup>11,12</sup> we estimate that at the intensity used the optical-to-thermal ratio excitation-rate factor has a value of  $\eta(I) \approx 0.93$ , which implies a Pockels coefficient  $r_{13} \approx 13 \times 10^{-12} \text{ m/V}$ . This value differs from the non-holographic, unclamped value  $r_{13} = 19.4 \times 10^{-12} \text{ m/V}$  obtained by Ducharme *et al.*<sup>13</sup> at a slightly different wavelength ( $\lambda = 515 \text{ nm}$ ). This discrepancy could be due to electron-hole competition,<sup>14</sup> which has not been included in our model and which would reduce the total space-charge field, or to an alteration of the effective  $r_{13}$  coefficient through the elasto-optic effect,<sup>15</sup> or to the remote possibility that  $180^\circ$  domains exist, leaving the crystal only partially poled.

The imaginary part of the coupling is caused by the component  $E_{\text{inphase}}$  of the space-charge field that is spatially in phase with the light intensity pattern. According to Eq. (16) this component owes its existence both to

the spatially oscillating photogalvanic current and to the spatially uniform photogalvanic current. At the light intensity used in this experiment the magnitude of this component of the field is given by

$$E_{\text{inphase}} = \frac{k_B T}{e} (\eta k_{\text{drift}} + k_{\text{pg}} + k_{\Delta\text{pg}}) = g_I^{eo} \frac{2c}{\omega n_{\text{ord}}^3 r_{13}}. \quad (17)$$

Using the value  $r_{13} \approx 13 \times 10^{-12} \text{ m/V}$  obtained above, we find that at this intensity  $E_{\text{inphase}} = 450 \text{ V/cm}$  along the  $-\hat{c}$  direction. The magnitude of this periodic field is in agreement (within factors of 2) with that obtained in  $\text{BaTiO}_3$  by other researchers.<sup>16-18</sup>

Figure 3 shows the intensity dependence of the imaginary part of the electro-optic coupling for two different internal beam-crossing half-angles ( $\theta_{\text{int}} = 0.3^\circ$  and  $\theta_{\text{int}} = 0.8^\circ$ ) of the optical beams. At these small angles trap gratings, which are caused by the polarizabilities of the trap sites, contribute significantly to the measured coupling.<sup>10</sup> In the data shown in Fig. 3 we have already subtracted the coupling produced by these trap gratings, using a procedure given in Ref. 10. We see that at both beam-crossing angles the intensity dependence of the imaginary part of the coupling is practically identical, as predicted by Eq. (16).

### Competing Photogalvanic Terms

From these measurements alone we cannot distinguish the effects of the various terms in parentheses in Eq. (16) or (17). However, assume for simplicity that we have only two levels from which photoexcitation of holes may occur: a deep donor level and a shallow acceptor level. In Appendix A we show that

$$k_{\text{pg}}(I) = \frac{eI}{k_B T \mu_{\parallel} n_0(I)} [s_A d_A N_{A;0} F(I) + s_D d_D N_{D;0} F(I)], \quad (18)$$

where  $n_0$  is the average density of free holes in the valence band,  $\mu_{\parallel}$  is the hole mobility parallel to the crystal's  $c$  axis, and the subscripts  $A$  and  $D$  refer to the acceptor and donor levels, respectively. The drift term  $k_{\text{drift}}$  in Eq. (16) depends on the boundary conditions of the crystal. If the crystal is shorted and there is no externally applied electric field, then  $E_0 = 0$ , making  $k_{\text{drift}} = 0$ . If instead the

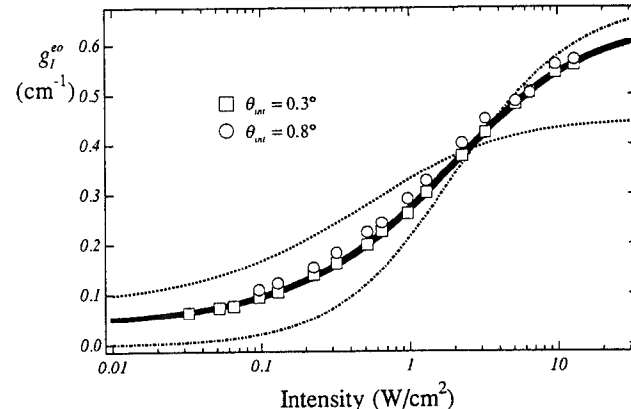


Fig. 3.  $g_I^{eo}$  in crystal FREE versus light intensity  $I$  at two internal beam crossing half-angles  $\theta_{\text{int}}$ . The solid curve is the best fit to the two-level model discussed in the text. The other curves are best fits assuming that only one of the levels contributes to the photogalvanic effect.  $\lambda = 488 \text{ nm}$ ;  $T = 17.7 \pm 0.2^\circ\text{C}$ .

crystal is an open circuit, then the spatially uniform part of the photogalvanic current causes charge to pile up on the  $\pm\hat{c}$  faces of the crystal, eventually creating a spatially uniform photovoltaic electric field  $E_{pv}$  inside the crystal:

$$E_0(I) = E_{pv}(I) = -\frac{\langle j^{pg}(I) \rangle}{\langle \sigma(I) \rangle}$$

$$= -\frac{I}{\mu_0 n_0(I)} [s_A d_A N_{A,0} F(I) + s_D d_D N_{D,0} F(I)]. \quad (19)$$

Here  $\sigma(I)$  is the total conductivity and the angle brackets denote spatial averaging. Combining Eq. (19) with the definition  $k_{drift}(I) = [e/(k_B T)]E_0(I)$  shows that under open-circuit conditions

$$k_{drift} = -k_{pg}, \quad (20)$$

so that at high intensities, where  $\eta(I)$  approaches unity (negligible dark conductivity), two of the terms in Eq. (16) should exactly cancel, leaving only  $g_I^{(0)} \propto k_{\Delta pg}$ . But at high intensity this term vanishes as well, because the light-induced redistribution of charges among the various levels at any given location saturates at high intensity. Although Eq. (20) was derived for the special case of a two-level model with a single charge carrier, in Appendix B we show, using open-circuit conditions and a few general assumptions, that the steady-state spatially oscillating currents produced directly by the photogalvanic effect and indirectly by the induced photovoltaic field are always of the same magnitude and of opposite sign. In other words, in open-circuit conditions and at optical intensities at which the dark conductivity can be neglected, the photogalvanic effect should have no net influence on the steady-state space-charge field.

But this null effect is not what we observe! Although, mathematically, at high intensity  $g_I^{(0)}$  should approach zero, experimentally we observe that it approaches its maximum value instead. This discrepancy could be explained if, for some reason, the uniform photovoltaic field created by the spatially uniform part of the photogalvanic current did not build up to the expected amount. We measured this field externally with a high-impedance ( $>10^{14} \Omega$ ) electrometer, taking precautions not to short the crystal faces inadvertently, and obtained the value  $E_{pv} \approx 10 \text{ V/cm}$  in the  $+\hat{c}$  direction,<sup>19</sup> which is much smaller than the observed 450-V/cm amplitude of the spatially varying space-charge field. The magnitude of this externally measured field agrees with previously published values.<sup>20</sup> When we measured the photogalvanic current directly, we found that it flowed in the  $-\hat{c}$  direction, which is consistent with the sign of the field measured by the electrometer, since at steady state the field should oppose the photogalvanic current. This is also the correct direction to account for the sign of our holographically measured  $g_I^{(0)}$ , provided that the coupling is due mainly to the spatially oscillating photogalvanic current term  $k_{pg}$ . We confirmed this conclusion by applying an external field along the  $+\hat{c}$  direction and observing a decrease of  $g_I^{(0)}$ , whereas  $g_I^{(0)}$  increased when a field was applied along the  $-\hat{c}$  direction.

We do not understand why the uniform electric field  $E_{pv}$  is so low under apparently open-circuit conditions, al-

though we considered several possibilities. The simplest explanation is that the crystal is in a closed circuit and not in an open circuit. Other researchers have also noticed that  $E_{pv}$  never builds up to the total amount expected for a closed circuit, and they have attributed this phenomenon to some kind of shorting mechanism.<sup>16,21</sup> In our experiments the silver paint that mounts the crystal may have provided an adequate pathway to short out the  $\pm\hat{c}$  faces of the crystal, as could have the water bath around the crystal. However, when we performed similar experiments, but with the crystal mounted on an insulating block in air with no silver paint, we found no change in the measured value of the imaginary part of the coupling with or without a wire electrically connecting the  $\pm\hat{c}$  faces. A second shorting mechanism could be that the surface conductivity of the crystal is somehow significantly higher than the bulk conductivity, thereby permitting the circuit to be shorted through the crystal surface. For example, Günter claims that in  $\text{LiNbO}_3$  the surface conductivity can be a few hundred times that of the bulk.<sup>21</sup> For either the crystal surfaces or the silver paint to be effective in shorting out the bulk, the charges must first reach the surfaces of the crystal. To see if they do, we numerically calculated the steady-state distribution of charge and the resulting electric field produced by an incident Gaussian beam for the case of the crystal surrounded by a perfect insulator and also for the case of a crystal surrounded by a perfect conductor. We made a few reasonable simplifications to make this calculation practical: Diffusion was neglected, the photoconductivity and the photogalvanic current were assumed to be linearly proportional to the light intensity, and the intensity of the probe beam was neglected. However, we retained the dark conductivity as well as the variation of conductivity with direction in the crystal.<sup>22,23</sup> For the beam size and crystal dimensions used, our calculation predicts that only small amounts of charge reach the four surfaces surrounding the light beam. It is still possible that charge flows down the light beam and connects the entrance and the exit faces of the crystal, although this conduction path is perpendicular to the direction of the photovoltaic field. There might also be an internal short circuit if either the conductivity or the photogalvanic current itself were a function of  $k_g$ . For example, electron conduction, while not large enough to create a significant, spatially periodic, space-charge field, might be sufficient to short out the spatially uniform field. However, one can show that if this were true then  $g_I^{(0)}$  would vary appreciably with  $k_g$ ; yet the data in Figs. 2 and 3 clearly show that  $g_I^{(0)}$  does not vary with  $k_g$ . Finally, there is a more exotic explanation, which is that there are clamped and unclamped values of the photogalvanic tensors and that these differ widely, akin to the variation between clamped and unclamped Pockels coefficients.<sup>15</sup> The spatially oscillatory current would then act through the clamped value of the photogalvanic effect, while the spatially uniform current would act through the unclamped value, thereby accounting for the failure of these two effects to balance.

Notwithstanding the above excuses for the small size of the externally measured value of  $E_{pv}$ , we tried to determine  $E_{pv}$  by another method. We connected the crystal to an electrometer with silver print electrodes and measured the photogalvanic current while illuminating the crystal

with a single light beam. We also determined the conductivity  $\sigma$  of the same crystal through grating decay measurements. From Ohm's law we obtain  $E_{pv}(I) = -j^{pg}(I)/\sigma(I)$ , which gives a value of 15 V/cm at high optical intensities. This value is similar to the electrometer reading mentioned above. However, both of these measurements use external electrodes and so may underestimate both the  $E_{pv}$  and the  $j_{pg}$  present in the bulk of the crystal. For example, in order to permit the current measurements to be made correctly with external electrodes, the beam should uniformly illuminate the entire crystal; otherwise the current that actually reaches the surfaces of the crystal can be significantly reduced, as we explain below. The large size of our crystal did not allow us to illuminate it at a high intensity. We compromised by using a  $1/e$  beam diameter of 6 mm, which is slightly smaller than the 7.34-mm distance between the  $c$  faces of the crystal. A further complication is that transverse illumination (light propagation perpendicular to the electrodes) always causes a dark fringe at the electrode surfaces, which results from the interference between the incident beam and the Fresnel reflection off the surface.<sup>24</sup> This dark region reduces the amount of the internally generated current that reaches the external electrodes. Finally, polishing of our crystal produced scratches and microcracks on its  $c$  faces, which inhibit good electrical contact.

Consequently we do not know whether the small size of  $j^{pg}$  measured with external electrodes is a true measure of the internal  $E_{pv}$ . However, we do know from our measured values of  $g_I$ <sup>20</sup> that inside the crystal the effect of any spatially uniform field is overwhelmed by the effect of the spatially varying photogalvanic current.

Finally, we also considered the possibility that the observed imaginary<sup>25</sup> part of the coupling was due to pyroelectric currents and not to the photogalvanic effect. However, these currents would contribute only to the real part of the coupling and at a level orders of magnitude smaller than what we observe.

#### Two-Level Model

Although the two-level model developed here cannot explain the dominance of the spatially varying photogalvanic current over the spatially uniform photogalvanic current, it can account for the intensity dependence shown in Fig. 3. Let us assume that the crystal is in a closed circuit, so that we can ignore the spatially uniform photogalvanic current and set  $E_{pv} \approx 0$ . We assume that holes can be either optically or thermally excited from the shallow acceptor traps but can be excited only by light from the deep donor traps. The model for the intensity dependence of the population of both levels of trap sites is given in Appendix A; it requires four parameters, which we have previously measured for this BaTiO<sub>3</sub> sample (FREE) by both induced absorption and holographic experiments.<sup>8</sup> The only two extra parameters needed for performing the curve fits are terms proportional to the average photogalvanic transport distances  $d_A$  and  $d_D$  and to the recombination constants  $\gamma_A$  and  $\gamma_D$ . Since this crystal absorbs light strongly, the intensity of the light beam decreases considerably between the crystal's entrance and exit faces. We took this variation of light intensity with propagation distance into account in our curve fit, which is shown by the solid curve in Fig. 3. This fit yields the values

$$\left( \frac{\omega}{2c} \frac{n_{ord}^3 r_{13}}{\mu_{\parallel}} \gamma_D N_D \right) d_D = 1.4 \text{ cm}^{-1},$$

$$\left( \frac{\omega}{2c} \frac{n_{ord}^3 r_{13}}{\mu_{\parallel}} \gamma_A N_D \right) d_A = 0.5 \text{ cm}^{-1}.$$

From these measurements we cannot extract the values of the photogalvanic transport distance  $d_A$  and  $d_D$ , because we do not know  $\gamma_A$  and  $\gamma_D$ . However, we can estimate their order of magnitude. If we assume that the recombination rates to both trap levels are approximately equal, then we can set

$$\frac{\mu_{\parallel}}{\gamma_D N_D} \approx \frac{\mu_{\parallel}}{\gamma_A N_D} \approx \frac{\mu_{\parallel} \tau}{2},$$

where  $\tau$  is the time that an excited hole remains in the valence band. Using  $\mu_{\parallel} \tau \approx 2 \times 10^{-10} \text{ cm}^2/\text{V}$ ,<sup>26</sup> we estimate that  $d_A$  and  $d_D$  are of the order of 1 nm.

We also tried fitting our data to a two-donor-level model in which only one of the levels contributes to the photogalvanic current. The dashed and dashed-dotted curves in Fig. 3 are these curve fits, and it is evident that in this model both levels must be photogalvanically active to explain the data best.

#### Direct-Current Measurements

The data in Fig. 3 show that the photogalvanic coupling can be described well by a two-level model. This model gives a nonlinear dependence of the photogalvanic current on light intensity, which, in principle, should be detectable by measuring the spatially uniform component of the photogalvanic current directly. We measured the photogalvanic current directly on the same crystal (FREE) by connecting an electrometer to its  $c$  faces with silver paint electrodes. We do not have confidence in these measurements on the crystal FREE because the data were not reproducible and for the reasons stated above. Consequently we measured the photogalvanic current in another crystal (CHIP) with light-induced absorption characteristics similar to those of FREE but of smaller size (along  $\hat{a}$ , 3.65 and 5.63 mm; along  $\hat{c}$ , 4.93 mm) and of better surface quality. The  $(1/e)$  beam diameter was 10.7 mm, more

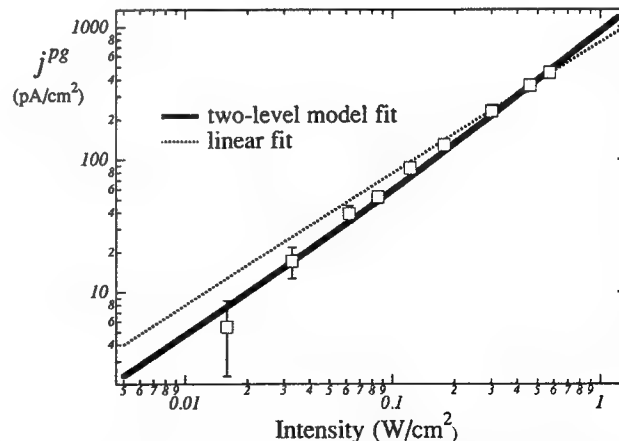


Fig. 4. Photogalvanic current measured externally with an electrometer in crystal CHIP versus light intensity  $I$ . The solid line is the best fit to the two-level model; the dotted line is a best fit to a simple linear dependence of the photogalvanic current on intensity.  $\lambda = 488 \text{ nm}$ ;  $T = 21.4 \pm 0.2^\circ\text{C}$ .

than twice the crystal length in the  $\hat{c}$  direction. The large amount of power absorbed by the crystal prevented us from taking measurements at the same temperature at which the coupling measurements were taken (17.7°C), so we used the lowest temperature that our setup could provide,  $21.4 \pm 0.2^\circ\text{C}$ . These data are shown in Fig. 4. The solid line is a fit with the four parameters obtained from light-induced absorption experiments in this crystal and the two photovoltaic parameters obtained previously for FREE. The only unknown parameter is an overall scaling factor. We see that, although the two-level model gives a better fit to the data than does a simple one-level (linear) model, it is necessary to measure the current over a 2-order-of-magnitude range in order to see any significant difference between the two models. In contrast, with the holographic measurements shown in Fig. 3 the different predictions of the two models are more obvious.

## Discussion

Finally, we explain the intensity dependence of the photovoltaic effect in a different way. Since  $k_{\Delta pg}$  contributes only a small correction to the coupling, and only at intermediate optical intensities, we focus our discussion on  $k_{pg}$ , which makes the dominant contribution to  $g_I^{(0)}$ . Let a hole be excited into the valence band from any trap site. Once this charge carrier has reached thermal equilibrium with the lattice, it will have forgotten from which site it was excited and will diffuse by a random walk. Neglecting the time required for thermalization, the mean-square distance that the hole diffuses before recombining into an acceptor trap site or a donor trap site is given by

$$\Lambda_A^2 = (k_B T/e) \mu \tau_A, \quad (21a)$$

$$\Lambda_D^2 = (k_B T/e) \mu \tau_D, \quad (21b)$$

where  $\tau_A$  and  $\tau_D$  are the average times that the hole spends in the valence band before it recombines into an acceptor or a donor trap site, respectively. From Eqs. (18) and (21) and the intensity dependence of the free charge carriers given in the Appendix A (Eq. A27), we find that

$$k_{pg}(I) = \frac{k_B T}{e} \left[ \frac{d_A}{\Lambda_A^2(I)} \frac{s_A I}{s_A I + \beta_A} + \frac{d_D}{\Lambda_D^2(I)} \right]; \quad (22)$$

i.e., for a given photovoltaic transport distance  $d_A$  or  $d_D$ , the smaller the mean-square diffusion length the larger will be the effect on the photovoltaic current on beam coupling. Because a spatially varying optical intensity redistributes charges among the trapping levels, it alters the lifetimes  $\tau_{A,D}$  and the corresponding diffusion lengths  $\Lambda_{A,D}^2(I)$ . This effect adds an additional intensity dependence to the imaginary part of the coupling coefficient.

## 4. CONCLUSIONS

Using a band-conduction model, we have shown that photovoltaic currents should alter the phase shift of photorefractive gratings both directly, by creating a spatially oscillating current, and indirectly, by creating a spatially uniform electric field. For an open-circuited crystal, at optical intensities for which thermal excitation can be neglected, these two effects should exactly cancel. However, we observe that in a nominally open-circuited crystal the effect of the spatially uniform electric field and its

associated drift current are anomalously small compared with the effect of the spatially oscillating current. Although results of only one crystal sample were presented in this paper, we have analyzed other barium titanate crystals, and all exhibit similar behavior.

To explain the intensity dependence of the imaginary part of the measured two-beam coupling, we have generalized Glass's model of the photovoltaic effect to include the effects of multiple trap sites. Assuming that the drift current is negligible, we account for the intensity dependence of the imaginary part of the coupling by using only two different levels of trap sites. We find two contributions to the intensity dependence: First, because the photovoltaic transport distances of the two levels are different, the light-induced redistribution of charge among the levels changes the net photovoltaic current. Second, because the diffusion length of the mobile charge changes with light intensity, light can alter how much a given photovoltaic current affects photorefractive beam coupling.

## APPENDIX A

We extend the band-conduction model to include charge excitation and recombination from multiple levels. For simplicity we consider a single type of charge carrier (electrons or holes, but not both). Our starting equations are a generalization of those presented in Ref. 8, but with the addition of a photovoltaic current for each level. The equations are

$$\frac{\partial N_j^E}{\partial t} = (\beta_j + \bar{s}_j : \mathbf{E}_{\text{opt}} \mathbf{E}_{\text{opt}}^*) N_j^F - \gamma_j N_j^E n, \quad (A1)$$

$$\mathbf{j} = en\bar{\mu} \cdot \mathbf{E}_{\text{SC}} \mp k_B T \bar{\mu} \cdot \nabla n + \mathbf{j}^{\text{pg}}, \quad (A2)$$

$$\sum_j \left( \xi_j^F \frac{\partial N_j^F}{\partial t} + \xi_j^E \frac{\partial N_j^E}{\partial t} \right) \mp \frac{\partial n}{\partial t} + \frac{\nabla \cdot \mathbf{j}}{e} = 0, \quad (A3)$$

$$\nabla \cdot (\epsilon_0 \bar{\epsilon} \cdot \mathbf{E}) = e \sum_j (\xi_j^F N_j^F + \xi_j^E N_j^E), \quad (A4)$$

where  $N_j^E$  and  $N_j^F$ , respectively, are the densities of the  $j$ th sites that are empty or full of the mobile charge and  $n$  is the density of charges in the appropriate band. The rate of optical excitation from the  $j$ th level into the appropriate band is  $\bar{s}_j : \mathbf{E}_{\text{opt}} \mathbf{E}_{\text{opt}}^*$ . Note that we have generalized  $\bar{s}_j$  to a second-rank tensor in order to describe the polarization dependence of the optical excitation. The thermal excitation rate and the recombination constant for the  $j$ th level are denoted by  $\beta_j$  and  $\gamma_j$ , respectively. In Eq. (A2)  $\mathbf{j}$  is the total current density,  $k_B T$  is the thermal energy,  $e$  is the charge constant,  $\bar{\mu}$  is the mobility tensor of the charge carrier,  $\mathbf{E}_{\text{SC}}$  is the space-charge electric field, and  $\mathbf{j}^{\text{pg}}$  is the total photovoltaic current. In Eq. (A4)  $\bar{\epsilon}$  is the relative static dielectric tensor of the crystal and  $\epsilon_0$  is the permittivity of vacuum. We have neglected the density of free carriers in Eq. (A4) because it is small for the cw intensities considered here. In Eqs. (A2) and (A3) the upper or the lower sign applies according to whether the charge carriers are holes or electrons, respectively. The factors  $\xi_j^F$  and  $\xi_j^E$  in Eqs. (A3) and (A4) denote the sign of the charge at a full or an empty site of the  $j$ th level. The values of  $\xi_j^F$  and  $\xi_j^E$  will depend on whether the site is an electron donor or acceptor and on the type of charge carrier. For example, if the mobile charges are holes, then

$\xi_j^F = 0$  and  $\xi_j^E = -1$  for acceptor levels, while  $\xi_j^F = +1$  and  $\xi_j^E = 0$  for donor levels. These  $\xi_j$  terms are a book-keeping device used to ensure charge neutrality, but they play no role in our subsequent results since they appear only as a difference in the formulas. In general  $\xi_j^F - \xi_j^E = +1$  for holes and  $\xi_j^F - \xi_j^E = -1$  for electrons.

Assume that each type of trap site has a different contribution to the total photogalvanic current  $\mathbf{j}^{pg}$ . Let the total electric field at any position  $\mathbf{x}$  and any time  $t$  be given by  $\mathbf{E}_{opt}(\mathbf{x}, t) = \text{Re}[\mathbf{E}_{opt}(\mathbf{x})\exp(-i\omega t)]$ . Then  $\mathbf{j}^{pg}$  should have the phenomenological form

$$\mathbf{j}^{pg}(\mathbf{x}) = e \sum_j N_j^F \chi_j \cdot \mathbf{E}_{opt}(\mathbf{x}) \mathbf{E}_{opt}^*(\mathbf{x}), \quad (A5)$$

where  $\chi_j$  is the third-rank photogalvanic tensor of the trap sites of the  $j$ th level. We changed the notation from  $\bar{\beta}$  to  $\chi_j$ , since in Eq. (A5) the number density has been factored out. There is a difference in form between Eq. (A5) and Eq. (7) of the text: here we do not explicitly write  $\chi_j$  in terms of an optical excitation tensor and a photogalvanic displacement vector, because this cannot be done (or cannot be done in a simple way) for arbitrary beam polarizations.

Let two monochromatic quasi-plane waves, a reference beam and a probe beam, interact in a photorefractive medium. Then

$$\mathbf{E}_{opt}(\mathbf{x}) = E_r(\mathbf{x}) \hat{e}_r \exp(i\mathbf{k}_r \cdot \mathbf{x}) + E_p(\mathbf{x}) \hat{e}_p \exp(i\mathbf{k}_p \cdot \mathbf{x}),$$

where  $E_{r,p}(\mathbf{x})$  are slowly varying envelopes and  $\hat{e}_{r,p}$  are the polarization unit vectors of the reference and the probe beams, respectively. If  $|E_p| \ll |E_r|$ , we can linearize Eqs. (A1)–(A5), by expanding  $N_j^{F,E}$ ,  $n$ ,  $\mathbf{j}$ , and  $\mathbf{E}$  into first order in  $\exp(i\mathbf{k}_g \cdot \mathbf{x})$ :

$$N_j^{F,E} = N_{j;0}^{F,E} + \text{Re}[N_{j;1}^{F,E} \exp(i\mathbf{k}_g \cdot \mathbf{x})], \quad (A6)$$

$$n = n_0 + \text{Re}[n_1 \exp(i\mathbf{k}_g \cdot \mathbf{x})], \quad (A7)$$

$$\mathbf{j} = \mathbf{j}_0 + \text{Re}[\mathbf{j}_1 \exp(i\mathbf{k}_g \cdot \mathbf{x})], \quad (A8)$$

$$\mathbf{E} = \mathbf{E}_0 + \text{Re}[\mathbf{E}_1 \exp(i\mathbf{k}_g \cdot \mathbf{x})], \quad (A9)$$

where the grating wave vector is defined by

$$\mathbf{k}_g = \mathbf{k}_p - \mathbf{k}_r = (\omega/c)(n_p \hat{s}_p - n_r \hat{s}_r). \quad (A10)$$

In Eq. (A10)  $n_{p,r}$  are the indices of refraction for the beams traveling in the directions of the unit vectors  $\hat{s}_{p,r}$ . Solving Eqs. (A1)–(A5), we find that the steady-state, spatially varying space-charge field depends on the grating wave vector according to

$$\mathbf{E}_1 = \pm i \hat{k}_g \frac{k_B T}{e} \frac{(k_g \pm i k_{\text{drift}}) \left( \sum_j m_j k_{0j}^2 / k_0^2 \right) \pm i \frac{2E_p E_r^*}{I} k_{pg} \pm i \left( \sum_j m_j k_{sj} - \sum_j k_{sj} \sum_j m_j \frac{k_{0j}^2}{k_0^2} \right)}{1 + \{[k_g(k_g \pm i k_{\text{drift}} \mp i k_{\text{uniform}})]/k_0^2\}}, \quad (A11)$$

where

$$k_{\text{drift}} = \frac{e}{k_B T} \frac{(\hat{k}_g \cdot \bar{\mu} \cdot \mathbf{E}_0)}{(\hat{k}_g \cdot \bar{\mu} \cdot k_g)}, \quad (A12)$$

$$k_{0j}^2 = \frac{e^2}{k_B T \epsilon_0 (\hat{k}_g \cdot \bar{\epsilon} \cdot \hat{k}_g)} N_j^{\text{eff}}, \quad (A13)$$

$$N_j^{\text{eff}} = \frac{N_{j;0}^F N_{j;0}^E}{N_{j;0}^F + N_{j;0}^E}, \quad (A14)$$

$$k_0^2 = \sum_j k_{0j}^2, \quad (A15)$$

$$k_{pg} = \frac{eI}{k_B T n_0 (\hat{k}_g \cdot \bar{\mu} \cdot \hat{k}_g)} \sum_j N_{j;0}^F \hat{k}_g \cdot \bar{\chi}_j \cdot \hat{e}_p \hat{e}_r^*, \quad (A16)$$

$$k_{\text{uniform}} = \sum_j k_{sj}, \quad (A17)$$

$$k_{sj} = \frac{e}{k_B T n_0 \hat{k}_g \cdot \bar{\mu} \cdot \hat{k}_g} n_j^{\text{eff}} (|E_p|^2 \hat{k}_g \cdot \bar{\chi}_j \cdot \hat{e}_p \hat{e}_r^* + |E_r|^2 \hat{k}_g \cdot \bar{\chi}_j \cdot \hat{e}_r \hat{e}_p^*), \quad (A18)$$

$$m_j = \frac{2E_p E_r^* \bar{s}_j \cdot \hat{e}_p \hat{e}_r^*}{\bar{s}_j \cdot (|E_p|^2 \hat{e}_p \hat{e}_p^* + |E_r|^2 \hat{e}_r \hat{e}_r^*) + \beta_j}. \quad (A19)$$

Note that in Eq. (A19)  $m_j$  is not the modulation of the light intensity pattern; it is the modulation of the optical excitation from the  $j$ th level.

The coupling is obtained by using the usual coupled-mode analysis and the space-charge field given in Eq. (A11). In the undepleted-pump approximation we find that the coupling that is due to the electro-optic effect is

$$E_p(z) = E_p(0) \exp(g^{\text{eo}} z), \quad (A20)$$

where

$$g^{\text{eo}} = -\frac{i\omega}{2n_p c} \hat{e}_p^* \cdot [\bar{\epsilon}(\omega) \cdot \bar{R} \cdot E_1 \cdot \bar{\epsilon}(\omega)] \cdot \hat{e}_r E_r. \quad (A21)$$

Substitution of Eq. (A11) into Eq. (A21) gives us the  $\mathbf{k}_g$  dependence of the coupling for an arbitrary orientation and polarization of the incident beams. For the case considered in the text,  $\hat{e}_p = \hat{e}_r$ , and  $\mathbf{k}_g \parallel \hat{c}$ , and we obtain

$$\sum_j m_j k_{0j}^2 / k_0^2 = m \eta(I), \quad (A22)$$

$$\begin{aligned} \sum_j m_j k_{sj} - \sum_j k_{sj} \sum_j m_j \frac{k_{0j}^2}{k_0^2} \\ = m \left( \sum_j \frac{s_j I}{s_j I + \beta_j} k_{sj} - \eta(I) \sum_j k_{sj} \right) \\ = m k_{\Delta pg}(I), \end{aligned} \quad (A23)$$

where  $m$  is the modulation of the light intensity pattern and

$$\eta(I) \equiv \sum_j \frac{s_j I}{s_j I + \beta_j} \frac{k_{0j}^2}{k_0^2}. \quad (A24)$$

From the previous equations we get

$$\begin{aligned} g^{\text{eo}}(\mathbf{k}_g, I) &= \frac{\omega}{2c} n_{\text{ord}}^3 r_{13} \frac{k_B T}{e} \\ &\times \frac{\eta(I)[k_g + i k_{\text{drift}}(I)] + i k_{pg}(I) + i k_{\Delta pg}(I)}{1 + \{k_g[k_g + i k_{\text{drift}}(I) - i k_{\text{uniform}}(I)]/k_0^2(I)\}}, \end{aligned} \quad (A25)$$

which is Eq. (9) of the text.

All of these quantities depend on the light intensity, either directly or indirectly (through  $n_0$ ,  $N_{D;0}^F$ , or  $E_0$ ); however, in order to find their intensity dependence the number of active levels must be specified. The simplest multiple-level model that will show any intensity dependence is one with two active levels, a donor level and an acceptor level. We allow optical excitation of holes from both of them into the valence band; however, significant thermal excitation of holes can occur only from the shallow acceptor level. Let the total number of acceptor and donor sites be designated by  $N_A$  and  $N_D$ . Under these assumptions  $\xi_A^F = \xi_D^F = 0$ ,  $\xi_A^E = -1$ , and  $\xi_D^E = +1$ , and bulk charge neutrality demands that

$$N_{A;0}^F + N_{D;0}^F = N_A, \quad (A26)$$

where we have assumed again that the density of free holes is negligible compared with the density of occupied traps. From Eq. (A1),

$$n_0 = \frac{(s_A I + \beta_A) N_{A;0}^F}{\gamma_A N_{A;0}^E} = \frac{S_D I N_{D;0}^F}{\gamma_D N_{D;0}^E}. \quad (A27)$$

From Eqs. (A26)–(A27) we get

$$N_{D;0}^F = \frac{N_D + N_A \pm [(N_D + N_A)^2 - 4N_D N_A G]^{1/2}}{2G}, \quad (A28)$$

where

$$G(I) = 1 - \frac{\gamma_A s_D}{\gamma_D s_A} \frac{s_A I}{s_A I + \beta_A}. \quad (A29)$$

For the curve fits shown in the text we used  $N_A/N_D = 0.96 \pm 0.02$ ,  $\beta_A/s_A = 0.73 \pm 0.06$  W/cm<sup>2</sup>, and  $\gamma_A s_D/\gamma_D s_A = 0.033 \pm 0.007$ , which were obtained independently from induced absorption measurements.<sup>8</sup>

Finally, we relate  $k_{pg}$  to the photogalvanic transport distances  $d_A$  and  $d_D$ . Since the beams are polarized along the  $x$  axis of the crystal and since  $\mathbf{k}_g \parallel \hat{c}$ , the only elements of  $\chi$  that come into play are  $\chi_{31}$  of the acceptor and the donor levels. Let  $\chi_{A,31} = s_A d_A$  and  $\chi_{D,31} = s_D d_D$ . Then

$$k_{pg}(I) = \frac{eI}{k_B T \mu_{||} n_0(I)} [s_A d_A N_{A;0}^E(I) + s_D d_D N_{D;0}^F(I)], \quad (A30)$$

which is Eq. (18) of the text.

## APPENDIX B

In this appendix we prove that for a crystal in an open circuit the photogalvanic effect makes no net contribution to the steady-state space-charge field.

We show that, under very general conditions, the photogalvanic effect should have no net effect on the steady-state space-charge electric field of a photorefractive crystal if the crystal is an open circuit.

Let the photorefractive crystal be illuminated by an intensity pattern given by  $I(\mathbf{x}) = I_0(1 + m \cos k_g z)$ , and let the grating wave vector be along the crystal's  $c$  axis. For small crossing angles we can neglect diffusion currents, so that the magnitude  $j^{\text{total}}(z)$  of the total current density is given by

$$\begin{aligned} j^{\text{total}}(z) &= j^{\text{drift}}(z) + j^{\text{pg}}(z) \\ &= \sigma(z)E(z) + p(z)I(z), \end{aligned} \quad (B1)$$

where  $j^{\text{drift}}(z)$  and  $j^{\text{pg}}(z)$  are the magnitudes of the current densities that are due to drift and to the photogalvanic effect, respectively. If we assume that the conductivity  $\sigma$  and the photogalvanic current depend on the local intensity (i.e., we ignore spatial dispersion), then  $j^{\text{pg}}(z) = p[I(z)]I(z)$  and  $\sigma(z) = \sigma_{\text{dark}} + a[I(z)]I(z)$ , where  $\sigma_{\text{dark}}$  is the dark conductivity and  $a(I)$  is a proportionality factor that does not vary much with light intensity. Expanding the space-charge field, conductivity, and photogalvanic current in powers of  $m \cos k_g z$  yields

$$E(z) = E_0 + E_1 m \cos k_g z + \dots, \quad (B2)$$

$$\begin{aligned} \sigma(z) &= \sigma_{\text{dark}} + a(I_0)I_0 \\ &+ \left[ a(I_0) + \left( \frac{da}{dI} \right) \Big|_{I_0} \right] I_0 m \cos k_g z + \dots, \end{aligned} \quad (B3)$$

$$p(z) = p(I_0) + \left( \frac{dp}{dI} \right) \Big|_{I_0} I_0 m \cos k_g z + \dots. \quad (B4)$$

Substituting Eqs. (B2)–(B4) into Eq. (B1) and equating terms that have equal powers of  $m \cos k_g z$ , we obtain

$$E_0 = - \frac{p(I_0)I_0}{\sigma_{\text{dark}} + a(I_0)I_0}, \quad (B5)$$

$$E_1 = - \frac{p(I_0)I_0 + I_0^2 (dp/dI) \Big|_{I_0} + E_0 [a(I_0)I_0 + I_0^2 (da/dI) \Big|_{I_0}]}{\sigma_{\text{dark}} + a(I_0)I_0}. \quad (B6)$$

In Eqs. (B5)–(B6) we assume that the crystal and its surroundings constitute an open circuit.

Experimentally it is observed that at high cw intensities (where dark conductivity can be neglected) the photoconductivity and photogalvanic currents are nearly linear with intensity, implying that both  $(dp/dI) \Big|_{I_0}$  and  $(da/dI) \Big|_{I_0}$  are small. With both terms set to zero and dark conductivity neglected, Eqs. (B5) and (B6) give

$$\begin{aligned} E_1(\text{high intensity}) &\approx - \frac{p(I_0)I_0 - p(I_0)I_0}{a(I_0)I_0} \\ &= 0. \end{aligned} \quad (B7)$$

This result implies that for a crystal that is in an open circuit the spatially oscillating photogalvanic current exactly balances the spatially oscillating drift current induced by the uniform photovoltaic field acting on the spatially modulated conductivity.

## ACKNOWLEDGMENT

We gratefully acknowledge support from U.S. Air Force Office of Scientific Research contract F49620-88-C-00095.

## REFERENCES

1. V. I. Belinicher, V. K. Malinovskii, and B. I. Sturman, "Photogalvanic effect in a crystal with polar axis," Sov. Phys. JETP **46**, 362 (1977).
2. V. M. Fridkin, "Review of recent work on the bulk photovoltaic effect in ferro and piezo-electrics," Ferroelectrics **53**, 169 (1984).

3. B. Sturman, "Dynamic holography effects in ferroelectrics induced by spatially oscillating photovoltaic currents," *J. Opt. Soc. Am. B* **8**, 1333 (1991).
4. R. M. Pierce and R. S. Cudney, "Photorefractive coupling between orthogonally polarized light beams in barium titanate," *Opt. Lett.* **17**, 784 (1992).
5. A. M. Glass, D. von der Linde, and T. J. Negran, "High-voltage bulk photovoltaic effect and the photorefractive process in  $\text{LiNbO}_3$ ," *Appl. Phys. Lett.* **25**, 233 (1974).
6. A. Motes and J. J. Kim, "Intensity dependent absorption coefficient in photorefractive  $\text{BaTiO}_3$  crystals," *J. Opt. Soc. Am. B* **4**, 1379 (1987).
7. G. A. Brost, R. A. Motes, and J. R. Rotge, "Intensity dependent absorption and photorefractive effects in barium titanate," *J. Opt. Soc. Am. B* **5**, 1879 (1988).
8. R. S. Cudney, R. M. Pierce, G. D. Bacher, and J. Feinberg, "Absorption gratings in photorefractive crystals with multiple levels," *J. Opt. Soc. Am. B* **8**, 1326 (1991).
9. P. Magno García, L. Cescato, and J. Frejlich, "Phase-shift measurement in photorefractive holographic recording," *J. Appl. Phys.* **66**, 47 (1989).
10. R. S. Cudney, G. D. Bacher, R. M. Pierce, and J. Feinberg, "Measurement of the photorefractive phase shift," *Opt. Lett.* **17**, 67 (1992).
11. L. Holtmann, "A model for the non-linear photoconductivity of  $\text{BaTiO}_3$ ," *Phys. Status Solidi A* **113**, 89 (1989).
12. D. Mahgerefteh and J. Feinberg, "Explanation of the apparent sublinear photoconductivity of photorefractive barium titanate," *Phys. Rev. Lett.* **64**, 2195 (1990).
13. S. Ducharme, J. Feinberg, and R. R. Neurgaonkar, "Electro-optic and piezoelectric measurements in photorefractive barium titanate and strontium barium niobate," *IEEE J. Quantum Electron.* **QE-23**, 2116 (1987).
14. F. P. Strohkendl, J. M. C. Jonathan, and R. W. Hellwarth, "Hole-electron competition in photorefractive gratings," *Opt. Lett.* **11**, 312 (1986).
15. P. Günter and M. Zgonik, "Clamped-unclamped electro-optic coefficient dilemma in photorefractive phenomena," *Opt. Lett.* **16**, 1826 (1991).
16. S. Sternklar, S. Weiss, and B. Fischer, "Tunable frequency shift of photorefractive oscillators," *Opt. Lett.* **11**, 165 (1986).
17. K. R. MacDonald, "Self-pumped phase conjugation in photorefractive barium titanate," Ph.D. dissertation (University of Southern California, Los Angeles, Calif., 1990).
18. I. McMichael and P. Yeh, "Phase shifts of photorefractive gratings and phase-conjugate waves," *Opt. Lett.* **12**, 48 (1987).
19. D. Mahgerefteh, "The speed of the photorefractive effect, shallow traps, photogalvanic currents, and light induced surface damage in barium titanate," Ph.D. dissertation (University of Southern California, Los Angeles, Calif., 1990).
20. M. C. Gower, "Photo-induced voltages and frequency shifts in a self-pumped phase-conjugating  $\text{BaTiO}_3$  crystal," *Opt. Lett.* **11**, 458 (1986).
21. P. Günter, "Holography, coherent light amplification and optical phase conjugation with photorefractive materials," *Phys. Rep.* **93**, 199 (1982).
22. T. Y. Chang, "Nonlinear optical studies of photorefractive barium titanate: parameter measurements and phase conjugation," Ph.D. dissertation (University of Southern California, Los Angeles, Calif., 1986).
23. D. Mahgerefteh, D. Kirillov, and J. Feinberg, "Is the hole mobility proportional to the dc dielectric constant in photorefractive  $\text{BaTiO}_3$ ?" in *OSA Annual Meeting*, Vol. 17 of 1991 OSA Technical Digest Series (Optical Society of America, Washington, D.C., 1991), paper MJ4.
24. E. J. Herbulock, M. H. Garrett, and A. R. Tanguay, Jr., "Electric field profile effects on photorefractive grating formation in bismuth silicon oxide," in *OSA Annual Meeting*, Vol. 11 of 1988 OSA Technical Digest Series (Optical Society of America, Washington, D.C., 1991), paper THU4.
25. S. Ducharme, "Pyro-electro-optic phase gratings," *Opt. Lett.* **15**, 1791 (1991).
26. A. L. Smirl, K. Bohnert, G. C. Valley, and T. H. Boggess, "Formation, decay and erasure of photorefractive gratings written in barium titanate by picosecond pulses," *J. Opt. Soc. Am. B* **6**, 606 (1989).

# Self-bending of light beams in photorefractive phase conjugators

V. V. Eliseev

General Physics Institute, Academy of Sciences, 38 Vavilov Street, Moscow 117924, Russia

A. A. Zozulya

P. N. Lebedev Physical Institute, Academy of Sciences, Leninsky Prospekt 53, Moscow 117924, Russia

G. D. Bacher and Jack Feinberg

Departments of Physics and Electrical Engineering, University of Southern California, Los Angeles, California 90089-0484

Received April 30, 1991; revised manuscript received September 17, 1991

Stimulated photorefractive phase conjugators often exhibit well-defined curved beam paths that cannot be explained by simple beam fanning. We propose a model of these apparently curved paths as a series of straight-line segments, with beams propagating in both directions along these segments. These line segments spring from the amplification of scattered light between regions of the crystal already containing counterpropagating pump beams. As these line segments form, they create new interaction regions that generate new segments, thereby making the final beam path appear to be curved. Application of our model to a single-interaction-region mutually pumped phase conjugator shows that the threshold coupling strength required for the appearance of these new segments is only slightly higher than the threshold for the phase conjugator itself.

## INTRODUCTION

Light beams appear to follow curved paths inside photorefractive phase conjugators. Here we propose a detailed, though necessarily simplistic, description of how these light beams spring up inside a photorefractive crystal. We show that their curved paths are in fact a sequence of straight-line segments that connect many four-wave mixing regions inside the crystal.

In recent years a variety of photorefractive devices have been demonstrated that rely on stimulated light beams to perform optical phase conjugation. These self-pumped and mutually pumped phase conjugators (which include the cat mirror,<sup>1</sup> the double phase-conjugate mirror,<sup>2</sup> the bird-wing,<sup>3</sup> the frog-legs,<sup>4</sup> and the bridge conjugators,<sup>5</sup> and the unnamed geometry of Eason and Smout<sup>6</sup>) are all closely related<sup>7</sup> and differ only in the number and angle of their input beams.

Figure 1 is a photomicrograph of stimulated beams inside a cat conjugator.<sup>1</sup> The stimulated beams have collapsed into narrow filaments (for reasons that will not be discussed here). These filaments appear to follow curved paths, but on close inspection the curves are seen to consist of a series of straight-line segments connected by distinct bends. Our model requires that the filaments themselves consist of counterpropagating waves. We show that two separated regions inside the crystal, each having its own pair of counterpropagating waves, can find each other with new light beams, provided that the total round-trip reflectivity of a small seed wave between these regions is greater than unity. Our model predicts a sequence of such couplings, so that the path of the filaments eventually resembles a curved trajectory.

Consider the case of two counterpropagating beams that are already present inside a photorefractive crystal, as shown in Fig. 2. If a reflecting surface, such as a mirror or a wedding ring, is placed nearby, then a beam of light will spring up between the crystal and the reflecting surface, provided that the photorefractive coupling strength exceeds a certain threshold.<sup>8</sup> These stimulated beams grow and reach steady state when the reflectivity of the photorefractive phase conjugator declines to  $1/M$ , where  $M$  is the reflectivity of the mirror. The crystal acts as a phase conjugator with gain: It returns light from the mirror back to the mirror. If the mirror surface is replaced by a second photorefractive crystal that is also pumped by two counterpropagating beams, then a beam of light can spring up between the two crystals; they will find each other and direct counterpropagating light beams from one to the other,<sup>9</sup> as shown in Fig. 2b. Instead of two crystals one could consider two separate regions inside the same crystal, as shown in Fig. 2c. In that case a pair of counterpropagating beams can spring up between these two regions. These new counterpropagating beams would then make new interaction regions available, permitting new beams to spring up, as shown in Fig. 3. This bifurcation can occur repeatedly, with each new pair of counterpropagating beams serving as a springboard for the generation of more such beam pairs.

## STIMULATED SCATTERING AND PHASE CONJUGATION

When a single laser beam traverses a photorefractive crystal, imperfections and defects in the crystal scatter the incident light. The scattered light can coherently inter-



Fig. 1. Photomicrograph of stimulated beams inside a  $\text{BaTiO}_3$  cat conjugator, showing the segmented bent trajectories of the light beams.

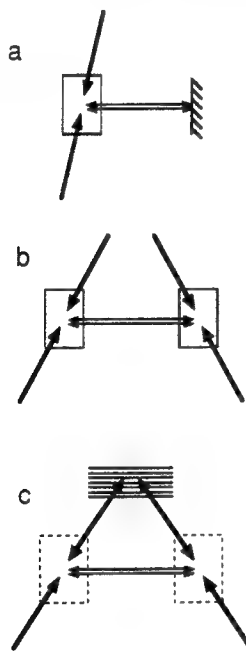


Fig. 2. a, Light beams (stippled arrows) springing up between a pumped crystal and the normal to a mirror. b, Light beams springing up between two pumped crystals. c, Light beam springing up between separate pumped regions of a single crystal, with the pumping beams connected by a photorefractive grating inside the crystal.

fer with the incident beam to create a multitude of photorefractive gratings in the crystal. A subset of the light scattered from these gratings reinforces the originally scattered beams, and these beams grow exponentially with distance in the crystal and emerge in a broad fan of light.

Now let two (preferably mutually incoherent) laser beams be incident upon the right- and the left-hand crystal boundaries with optical intensities  $I_R$  and  $I_L$ , respectively. Let the two beams intersect inside the crystal as shown in Fig. 3a. Because the two beams are mutually incoherent, they will not interfere with each other. However, each incident beam will interfere with its own randomly scattered beams to create its own armada of photorefractive gratings inside the crystal. The particu-

lar grating that diffracts beam  $R$  into the phase conjugate of beam  $L$  will also diffract beam  $L$  into the phase conjugate of beam  $R$  by time-reversal symmetry.<sup>2</sup> Because this grating is common to both beams, it is preferentially reinforced. In the simplest such mutually pumped phase conjugator (the geometry of Fig. 3a) the intensity transmission  $T_0$  of the device, defined as the fraction of the light input into one face that emerges phase conjugate to the beam at the other face, is found by solving the following equations<sup>2</sup>:

$$T_0 = \frac{c^2(q^{1/2} + q^{-1/2})^2 - (q^{1/2} - q^{-1/2})^2}{4}, \quad (1)$$

$$c = \tanh(G_0/2), \quad (2)$$

where  $q = I_R/I_L$  is the ratio of intensities of the two incident beams and  $G_0$  is the amplitude-coupling strength (dimensionless) in the region. These equations yield non-trivial solutions only if the coupling strength exceeds a threshold value  $G_0 \geq [(q + 1)/(q - 1)]\ln q$ .

## NEW BEAMS

Just above threshold the configuration of a single-interaction region turns out to be unstable: Arbitrarily weak beams will grow between two new regions of the nonlinear medium, with each region pumped by two counterpropagating waves as shown in Fig. 3b. The threshold for this instability occurs when the round-trip reflectivity of a weak seeding beam between the right- and the left-hand regions in Fig. 3b exceeds unity:

$$R_{\text{right}} R_{\text{left}} \geq 1. \quad (3)$$

In inequality (3)  $R_{\text{right}}$  is the phase-conjugate intensity reflectivity for the beam incident upon the right-hand re-

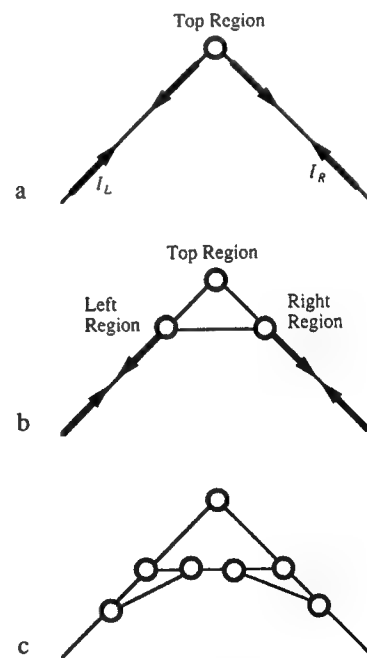


Fig. 3. Schematic of beam paths in a mutually pumped phase conjugator, a, before bifurcation, b, after one bifurcation, and, c, after a second bifurcation. The circles indicate interaction regions.

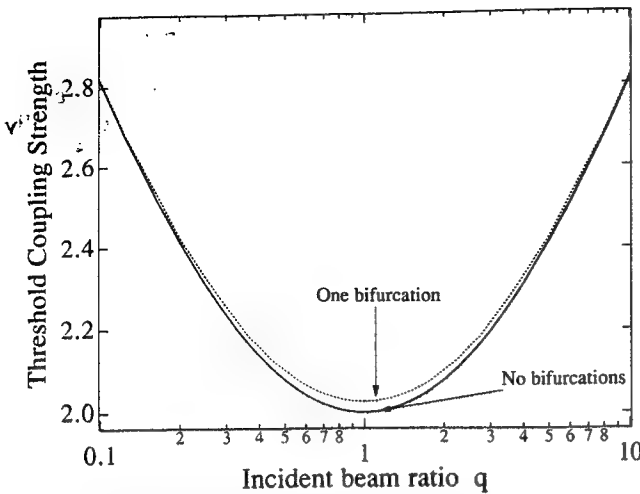


Fig. 4. Coupling strength at threshold versus incident beam ratio  $q$  for a mutually pumped phase conjugator with no bifurcations (solid curve; see Fig. 3a) and one bifurcation (dotted curve; see Fig. 3b).

gion from the left-hand region, and  $R_{\text{left}}$  is the same upon the left-hand region. Near threshold, these reflectivities can be computed from the traditional four-wave mixing equations with undepleted pumping beams, as in Ref. 10; here the usual counterpropagating pumping beams are taken to be the conjugate pairs  $I_L$  and  $I_L^C$  in the left-hand region and  $I_R$  and  $I_R^C$  in the right-hand region. We obtain

$$R_{\text{left}} = \frac{I_L}{I_L^C} \frac{[1 - \exp(-G_{\text{left}})]^2}{[1 + (I_L/I_L^C)\exp(-G_{\text{left}})]^2},$$

$$R_{\text{right}} = \frac{I_R}{I_R^C} \frac{[1 - \exp(-G_{\text{right}})]^2}{[1 + (I_R/I_R^C)\exp(-G_{\text{right}})]^2}.$$

In general, the values of coupling strengths in the various regions are all different. However, for simplicity we here take them all to be the same,  $G_0 = G_{\text{left}} = G_{\text{right}} \equiv G$ , for the remainder of our analysis. Even in this case we show that the system tends to generate new beams and that (except near threshold) these new beams increase the overall phase-conjugate reflectivity of the device.

Figure 4 shows the calculated threshold for phase conjugation versus the incident beam ratio  $q$  when there is only one interaction region and also shows the threshold for the system to bifurcate once to create three interconnected regions. Note that a single interaction region becomes unstable for a coupling strength that is even slightly larger than the single-region threshold, and a new path forms that bypasses the original interaction region. For example, for the case  $q = 1$  the single-region threshold (no bifurcations) is  $G_{\text{th}}^{(\text{1-region})} = 2$ , while the three-region threshold (one bifurcation) is only slightly larger:  $G_{\text{th}}^{(\text{3-regions})} = 2.026$ . For even larger values of  $G$  the system may undergo further bifurcation, as shown in Fig. 3c. This process will continue, with new beams springing up to connect new interaction regions and so to carve out a path, made of many straight-line segments, that approximates a curved trajectory. Because there is no unique path for the bifurcation, it is possible for different paths to be favored sequentially. This variability would cause the phase-conjugate signal to oscillate in time, as has been observed in the bird-wing and cat conjugators.<sup>11-13</sup>

## COUPLED-WAVE EQUATION

We analyze the three-region geometry of Fig. 3b by inspecting the slowly varying amplitudes  $A_j$  ( $j = 1, 2, 3, 4$ ) of the electromagnetic waves in each of the three interaction regions. For the geometry of Fig. 5 these amplitudes vary according to<sup>10</sup>

$$\frac{dA_1}{dx} = \nu A_4, \quad \frac{dA_2^*}{dx} = \nu A_3^*,$$

$$\frac{dA_3}{dx} = -\nu A_2, \quad \frac{dA_4^*}{dx} = -\nu A_1^*,$$

$$\nu = (\gamma/I_0)(A_1 A_4^* + A_2^* A_3). \quad (4)$$

In Eqs. (4)  $I_0 \equiv \sum_{j=1}^4 A_j^2$ ,  $0 \leq x \leq l$ , and  $\gamma = G/l$  is the coupling coefficient per unit length. Here we will consider only the case of a purely real coupling coefficient  $\gamma$  (which corresponds to a 90° phase shift between the light pattern and the resulting refractive-index pattern in the photorefractive crystal).<sup>14</sup> For this case the wave amplitudes  $A_j$  can all be taken as real without loss of generality.

The boundary conditions on the four wave amplitudes  $A_j$  differ here from those usually used. Consider the right-hand region shown in Fig. 3b, with the beams named as in Fig. 5. The usual boundary condition is to set the conjugate-wave amplitude to be zero at the right-hand boundary:  $A_3(l) = 0$ . Instead, here we let the conjugate wave be seeded by scattered light, so that  $A_3(l) = \epsilon^{1/2} A_2(l)$ . The finite seed in the right-hand (and left-hand) regions is required if the curved beam path is to dominate at large coupling strengths. Physically this seed is caused by the scattering from crystal defects of wave 2 into wave 3. We let the total amount of scattering remain constant but let the seeding parameter  $\epsilon^{1/2} \ll 1$  determine the fraction of the scattered light from amplitude  $A_2(l)$  that is scattered into precisely the amplitude  $A_3(l)$ . In the left-hand region we use a similar seeded boundary condition, and for simplicity we set the scattering strength to be the same in both of these regions. We set the phase of these scattered beams so that the light scattered from the left-hand region exactly reinforces the grating forming in the right-hand region and vice versa.

In the top region we could also replace the usual boundary conditions for a double-phase-conjugate mirror with the seeded boundary conditions, but we found that for  $\epsilon \ll 1$  the presence of finite seeding beams in this top region has a negligibly small influence on the behavior of the various waves except when the coupling coefficient is quite near the threshold  $G \approx G_{\text{th}}^{(\text{1-region})}$ . Therefore we set  $\epsilon = 0$  in the top region but keep  $\epsilon$  finite in the other two regions.

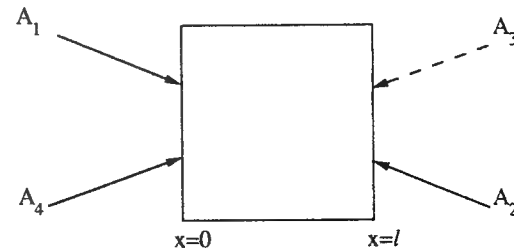


Fig. 5. Assignment of the interacting waves in a four-wave mixing region.

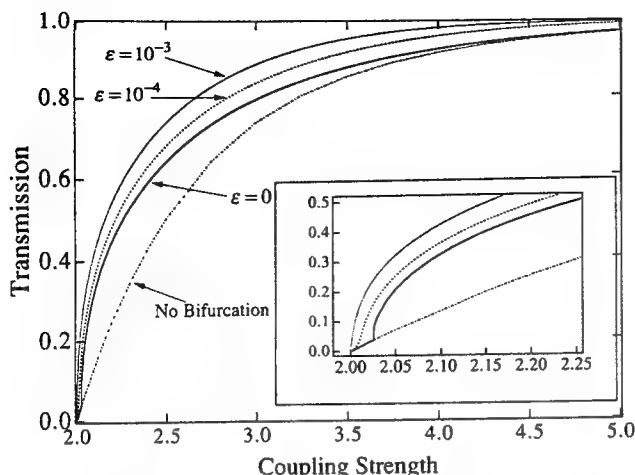


Fig. 6. Calculated transmission (throughput) of a mutually pumped phase conjugator with no bifurcation (i.e., the one-region geometry of Fig. 3a) and with one bifurcation (i.e., the three-region geometry of Fig. 3b) versus coupling coefficient  $G$ , for equal-intensity incident beams put into the device ( $q = 1$ ). The bifurcated data correspond to seeding values of  $\epsilon$  of  $0$ ,  $10^{-4}$ , and  $10^{-3}$ . The inset shows the region near threshold.

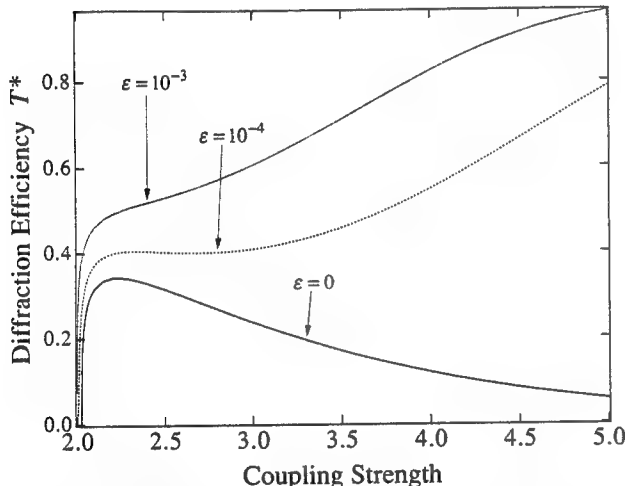


Fig. 7. Diffraction efficiency of the grating in the left-hand (or the right-hand) interaction region (Fig. 3b) versus coupling strength  $G$  for  $q = 1$ . The curves correspond to seeding values of  $\epsilon$  of  $0$ ,  $10^{-4}$ , and  $10^{-3}$ .

In Fig. 3b light entering from the bottom left-hand corner has the choice of two different paths before it exits at the bottom right-hand corner; the paths are a single diffraction from the grating at the top or two successive diffractions at the left- and the right-hand regions. These two paths will interfere provided that the difference in their lengths is within the coherence length of the incident laser beam. For the case of a purely real coupling coefficient  $\gamma$  this interference will always be exactly constructive irrespective of the lengths of these two optical paths. For example, consider the beam that propagates from the left-hand region directly to the right-hand region. This beam will always add constructively to the beam coming from the top region (as in two-beam energy coupling). A similar interference will also occur for the two light beams propagating from right to left, since they will traverse exactly the same two paths in the opposite direction. To show this quantitatively, consider Fig. 3b.

In the center of the right-hand region, let the phase of the beam incident from below be denoted by  $\phi_{R\uparrow}$ , where the first subscript denotes the region and the second indicates the incident beam's approximate direction. The phase of this beam when it reaches the left-hand region by way of the top is  $\phi_{L\downarrow} = \phi_{R\uparrow} + kd$ , where  $k$  is the wave-vector magnitude in the crystal and  $d$  is the path length from right to top to left. Similarly, the phase of the beam that starts in the center of the left-hand region and travels to the center of the right-hand region via the path left to top to right is  $\phi_{R\downarrow} = \phi_{L\downarrow} + kd$ . Because this path has the same optical length in both directions, these two equations can be combined to yield  $\phi_{R\downarrow} + \phi_{R\uparrow} = \phi_{L\downarrow} + \phi_{L\uparrow}$ , which is the condition for degenerate oscillation in a double-phase-conjugate resonator.<sup>15</sup> Therefore the seed beam that starts in the right-hand region, is phase conjugated in the left-hand region, and then is phase conjugated again in the right-hand region will be precisely in phase with the initial seed.

## RESULTS

When bifurcations occur, new beams spring up, and the overall transmission  $T$  of the system changes. For the case of equal-intensity input beams ( $q = 1$ ) the dependence of the transmission on the coupling strength  $G$  is shown in Fig. 6. Here the effect of the additional beam path is seen in the sharp jump in the transmission when  $G$  increases above the first bifurcation threshold  $G_{\text{th}}^{(3-\text{regions})}$  as shown in the inset of Fig. 6. The bifurcation increases the overall transmission of the device because the portion of the input not diffracted by the grating in the left-hand region will still be partially redirected by the grating at the top and will recombine coherently with the diffracted beam in the right-hand region. The original grating serves to catch some of the light that slips through the new gratings and to redirect it into the phase-conjugate beam.

Consider the symmetric case of equal-intensity input beams ( $q = 1$ ). Define  $T^*$  to be the fraction of beam  $I_L$  that is input into the left-hand side of the crystal and is deflected by the left-hand interaction region into the right-hand interaction region (i.e., the intensity diffraction efficiency of beam 2 into beam 4 described in Appendix A). Then we obtain  $T^* = (T^{1/2} - T_0^{1/2})/(1 - T_0^{1/2})$ , where  $T_0$  is defined just above Eq. (1) and  $T$  is the overall intensity transmission of the entire three-region device. Figure 7 illustrates the dependence of the diffraction efficiency  $T^*$  of either the left- or the right-hand region (these two diffraction efficiencies are equal when  $q = 1$ ) on the coupling strength  $G$  for several different values of the seeding parameter  $\epsilon$ . For any finite value of  $\epsilon$ ,  $T^*$  asymptotically approaches unity for high coupling strength, but the form of the approach depends on the value of the seed. For  $q = 1$  and for large values of the coupling strength, we find that

$$T^* = 2G \exp(-G) + \left[ \frac{\epsilon(1 - T^*)}{T^*} \right]^{1/2} \exp(G). \quad (5)$$

As  $T^*$  approaches 1, an increasing amount of light is channeled between regions, the left- and the right-hand interaction regions, so that the A-shaped pattern in Fig. 8a begins to resemble the sawed-off pattern of Fig. 8b. Note that Fig. 8b can be viewed as two mutually

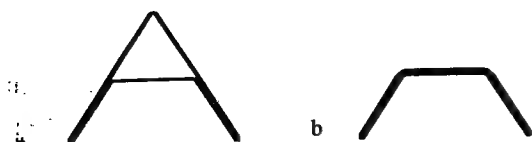


Fig. 8. Appearance of the beams of Fig. 3b for a, small coupling strength  $G$  and b, large  $G$ .

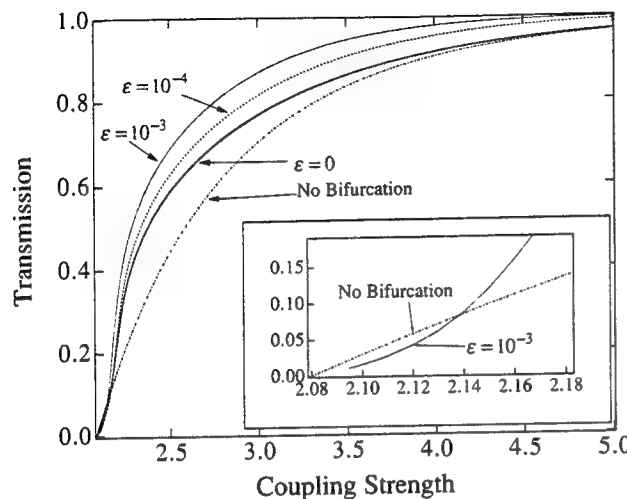


Fig. 9. Transmission in the one-region geometry of Fig. 3a, and in the three-region geometry of Fig. 3b versus coupling coefficient  $\Gamma$  for unequal incident beam intensities ( $q = 2$ ). The curves for the geometry of Fig. 3b correspond to seed values of  $\epsilon$  of 0,  $10^{-4}$ , and  $10^{-3}$ . The inset shows the region near threshold.

pumped phase conjugators sharing a common set of beams, and both the dynamic behavior and the stationary states of such a system have been shown to be critically dependent on the values of the seeds.<sup>16,17</sup>

In order to explore the behavior of the system with unequal input beam intensities ( $q \neq 1$ ), we repeated our analysis for the case of  $q = 2$ . The equations are less symmetric now, and each interaction region has a different diffraction efficiency. Nevertheless, the overall transmission of the device is quite similar to the  $q = 1$  case, as is shown in Fig. 9. However, with  $q = 2$  there is now a small region of  $G$  just beyond threshold in which the overall transmission decreases when the additional beams appear, as is shown in the inset of Fig. 9. In Fig. 10 we plot the diffraction efficiencies of each of the left- and the right-hand regions versus the coupling strength. The stronger beam is input on the left and the weaker beam on the right. Note that the diffraction efficiency is larger in the region with the weaker input beam. The asymmetry in the strength of the two bifurcation gratings is evident in Fig. 10, especially near threshold. Just above threshold we found a region of  $G$  for which the system oscillates between two states, first bifurcating and then relaxing back to the initial unbifurcated state.

For  $q \neq 1$  there is no longer a simple relation among the various grating efficiencies as in Eq. (5). We find numerically that the asymptotic behavior as  $G \rightarrow \infty$  of each region's diffraction efficiency is similar to the  $q = 1$  case, so that for any finite seed the bifurcation path dominates as  $G$  becomes large.

In summary, we have presented a simple model to explain the bending of light beams in various self-pumped

and mutually pumped phase conjugators. This model attributes the growth of curved beam paths inside the crystal to a series of straight-line segments caused by couplings between adjacent regions inside the crystal, each pumped by counterpropagating waves. We have shown that including a small but finite amount of scattered light is crucial for describing this self-bending. The bifurcation occurs even when the gratings in all three regions are taken to have the same coupling strength. In practice one should include the dependence of coupling strength on both the crossing angle and the orientation of the light beams inside the crystal, which can make the bifurcation path even more favorable. Also, we note that there are usually a multitude of possible bifurcation paths that compete for the available light energy and that the light path could oscillate repeatedly between them.

## APPENDIX A: MATHEMATICS

Consider a four-wave mixing region, described by the set of equations<sup>18</sup>

$$\begin{aligned} \frac{dA_1}{dx} &= \nu A_4, & \frac{dA_2^*}{dx} &= \nu A_3^*, \\ \frac{dA_3}{dx} &= -\nu A_2, & \frac{dA_4^*}{dx} &= -\nu A_1^*, \\ \nu &= (\gamma/I_0)(A_1 A_4^* + A_2^* A_3). \end{aligned} \quad (A1)$$

The values of waves 1, 2, and 4 are fixed at the beginning of the interaction region,

$$A_1(0), A_4(0), A_2(l),$$

and wave 3 is seeded:

$$A_3(l) = \epsilon^{1/2} A_2(l). \quad (A2)$$

We assume that  $\gamma$  is real. In this case the fields can be taken to be real. We introduce the variable

$$z = \int_0^x dx' \frac{\gamma}{I_0} (A_1 A_4 + A_2 A_3) = \int_0^x \nu dx'.$$

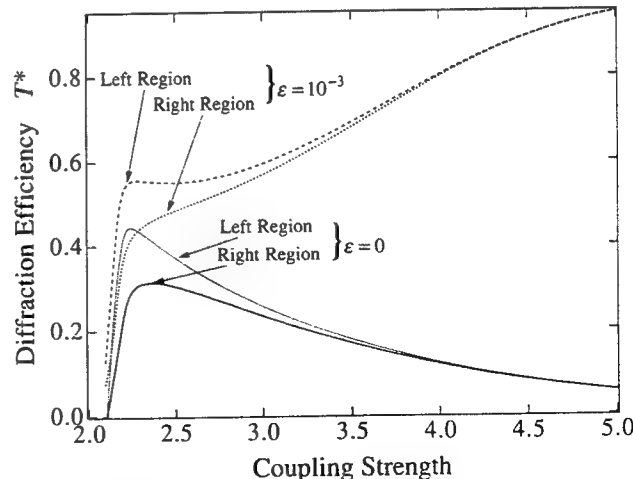


Fig. 10. Diffraction efficiency of the gratings in the left- and the right-hand interaction regions versus  $\Gamma$  for  $q = 2$ . Here the stronger beam is incident upon the crystal from the right and the weaker beam is incident from the left. The curves correspond to seeding values of  $\epsilon = 0$  and  $10^{-3}$ .

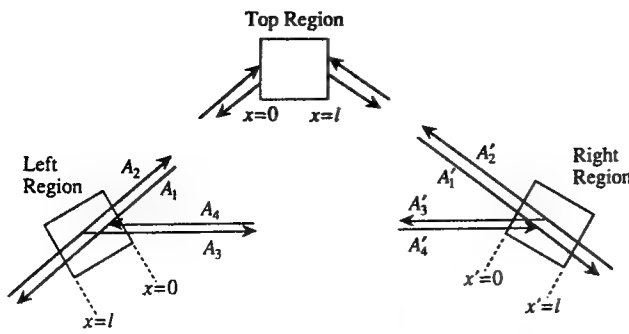


Fig. 11. Diagram of the three-interaction-region geometry, with the beams used in the analysis labeled. All beams in the right-hand region are primed. Note that the left- and the right-hand regions are laid out as mirror images.

The output amplitudes become a function of  $z$ :

$$\begin{aligned} A_1(l) &= A_1(0)\cos(z_l) + A_4(0)\sin(z_l), \\ A_4(l) &= -A_1(0)\sin(z_l) + A_4(0)\cos(z_l), \\ A_2(0) &= A_2(l)[\cos(z_l) - \epsilon^{1/2}\sin(z_l)], \\ A_3(0) &= A_2(l)[\sin(z_l) - \epsilon^{1/2}\cos(z_l)], \end{aligned} \quad (\text{A3})$$

where  $z_l \equiv z(x = l)$ .

Integrating Eqs. (A1) to obtain expressions for  $A_1(x)/A_4(x)$  and  $A_3(x)/A_2(x)$ , as in Ref. 10, and substituting Eqs. (A3) for the amplitudes, we obtain

$$\tanh(Ga) = b, \quad (\text{A4})$$

where

$$G \equiv \gamma l,$$

$$a \equiv \frac{\Delta}{2(I_1 + I_2 + I_4)},$$

$$b \equiv \frac{\Delta}{I_4 - I_1 + I_2 + 2\cot(z_l)[A_1(0)A_4(0) + \epsilon^{1/2}I_2]},$$

$$\begin{aligned} \Delta^2 &\equiv (I_1 + I_4)^2 + I_2^2 + 2I_2(I_1 - I_4)\cos(2z_l) \\ &+ 4I_2A_1(0)A_4(0)\sin(2z_l) \\ &+ 4I_2\epsilon^{1/2}[(I_4 - I_1)\sin(2z_l) \\ &+ 2A_1(0)A_4(0)\cos(2z_l)]. \end{aligned}$$

Here  $I_1 \equiv A_1^2(0)$ ,  $I_4 \equiv A_4^2(0)$ ,  $I_2 \equiv A_2^2(l)$ . If the three input fields are known, then Eq. (4) can be solved for  $z_l$ . The expressions for  $a$  and  $b$  are given here only to the lowest order in  $\epsilon$ . One may write exact expressions, but since  $\epsilon \ll 1$  there would be no advantage.

For the three-region geometry of Fig. 3b, there are three equations (A4) (one for each region), which are coupled by the boundary conditions. Since the presence of the seeding light has no effect on the top region except near threshold, we neglect the seeds in this region and use Eq. (2) from the text to calculate its transmission. The boundary conditions are as follows:

Left-hand region,

$$\begin{aligned} A_2(l) &= I_L^{1/2}, \\ A_1(0) &= T_0^{1/2}A_2'(0), \\ A_4(0) &= A_3'(0); \end{aligned}$$

right-hand region,

$$\begin{aligned} A_2'(l) &= I_R^{1/2}, \\ A_1'(0) &= T_0^{1/2}A_2(0), \\ A_4'(0) &= A_3(0). \end{aligned}$$

Here all the primed amplitudes refer to the right-hand region and the unprimed amplitudes refer to the left-hand region as indicated in Fig. 11. Note that the left- and the right-hand regions are laid out as mirror images, so that the external beams are input at  $x = l$  in both of these regions.  $T_0$  is the intensity transmission of the double phase conjugator in the top region, where  $A_2(0)$  and  $A_2'(0)$  are its two input beams. From Eq. (3) these boundary conditions are rewritten as

Left-hand region,

$$\begin{aligned} A_2(l) &= I_L^{1/2}, \\ A_1(0) &= (I_R T_0)^{1/2}[\cos(z_2) - \epsilon^{1/2}\sin(z_2)], \\ A_4(l) &= I_R^{1/2}[\sin(z_2) + \epsilon^{1/2}\cos(z_2)], \end{aligned}$$

where  $z_2 \equiv z(x = l)$ ;

Right-hand region,

$$\begin{aligned} A_2'(l) &= I_R^{1/2}, \\ A_1'(0) &= (I_L T_0)^{1/2}[\sin(z_1) - \epsilon^{1/2}\cos(z_1)], \\ A_4'(l) &= I_L^{1/2}[\sin(z_1) + \epsilon^{1/2}\cos(z_1)], \end{aligned}$$

where  $z_1 \equiv z(x = l)$ .

One determines  $z_1$  and  $z_2$ , and all other quantities are expressed through them. We could solve these equations analytically only for a few special cases. For example, if  $q = 1$  ( $I_L = I_R = I$ ) and  $\Gamma_1 = \Gamma_2 = \Gamma$ , then further analytic results can be obtained. In this case  $z_1 = z_2 = z$ . Since the system is left-right symmetric for input beams with equal intensities,  $q$  is always equal to 1 for the top region, regardless of the values of  $\epsilon$  and  $G$ , and the transmission of the top region depends only on  $G$ .

For  $q = 1$  one can solve for  $z$  in Eq. (4) by using the boundary conditions

$$\begin{aligned} A_2(l) &= I^{1/2}, \\ A_1(0) &= (T_0 I)^{1/2}[\cos(z) - \epsilon^{1/2}\sin(z)], \\ A_4(0) &= I^{1/2}[\sin(z) + \epsilon^{1/2}\cos(z)]. \end{aligned}$$

The overall transmission of the device is then given by

$$\begin{aligned} T &= \frac{[A_1(0)\cos(z) + A_4(0)\sin(z)]^2}{I} \\ &= [\sin^2(z) + T_0^{1/2}\cos^2(z) + \epsilon^{1/2}(1 - T_0^{1/2})\sin(z)\cos(z)]^2. \end{aligned}$$

## REFERENCES AND NOTES

1. J. Feinberg, "Self-pumped, continuous-wave phase conjugator using internal reflection," *Opt. Lett.* **7**, 486-488 (1982).
2. S. Weiss, S. Sternklar, and B. Fischer, "Double phase-conjugate mirror: analysis, demonstration, and applications," *Opt. Lett.* **12**, 114-116 (1987).
3. M. D. Ewbank, "Mechanism for photorefractive phase conjugation using incoherent beams," *Opt. Lett.* **13**, 47-49 (1988).

4. M. D. Ewbank, R. A. Vasquez, R. R. Neurgaonkar, and J. Feinberg, "Mutually pumped phase conjugation in photorefractive strontium barium niobate: theory and experiment," *J. Opt. Soc. Am. B* **7**, 2306-2316 (1990).
5. D. Wang, Z. Zhang, Y. Zhu, S. Zhang, and P. Ye, "Observations on the coupling channel of two mutually incoherent beams without internal reflection in BaTiO<sub>3</sub>," *Opt. Commun.* **73**, 495-500 (1989).
6. R. W. Eason and A. M. C. Smout, "Bistability and noncommutative behavior of multiple-beam self-pulsing and self-pumping in BaTiO<sub>3</sub>," *Opt. Lett.* **12**, 51-53 (1987).
7. M. Cronin-Golomb, "Almost all transmission grating self-pumped phase-conjugate mirrors are equivalent," *Opt. Lett.* **15**, 897-899 (1990).
8. J. Feinberg and R. W. Hellwarth, "Phase-conjugating mirror with continuous-wave gain," *Opt. Lett.* **5**, 519-521 (1980); erratum **6**, 257 (1981).
9. M. D. Ewbank, P. Yeh, M. Khoshnevisan, and J. Feinberg, "Time-reversal by an interferometer with coupled phase-conjugate reflectors," *Opt. Lett.* **10**, 282-284 (1985).
10. M. Cronin-Golomb, B. Fischer, J. O. White, and A. Yariv, "Theory and applications of four-wave mixing in photorefractive media," *IEEE J. Quantum Electron.* **QE-20**, 12-29 (1984).
11. G. Hussain, S. W. James, and R. W. Eason, "Observation and modeling of dynamic instabilities in the mutually pumped bird-wing phase conjugator in BaTiO<sub>3</sub>," *J. Opt. Soc. Am. B* **7**, 2294-2298 (1990).
12. D. J. Gauthier, P. Narum, and R. W. Boyd, "Observation of deterministic chaos in a phase conjugate mirror," *Phys. Rev. Lett.* **58**, 1640-1643, (1987).
13. A. V. Nowak, T. R. Moore, and R. A. Fisher, "Observation of internal beam production in a barium titanate phase conjugator," *J. Opt. Soc. Am. B* **5**, 1864-1878 (1988).
14. J. Feinberg, D. Heiman, A. R. Tanguay, Jr., and R. W. Hellwarth, "Photorefractive effects and light-induced charge migration in barium titanate," *J. Appl. Phys.* **51**, 1297-1305 (1980); erratum **52**, 537 (1981).
15. S. K. Kwong, A. Yariv, M. Cronin-Golomb, and B. Fischer, "Phase of phase conjugation and its effect in the double phase-conjugate resonator," *J. Opt. Soc. Am. A* **3**, 157-160 (1986).
16. A. V. Mamaev and A. A. Zozulya, "Dynamics and stationary states of a photorefractive phase-conjugate semilinear mirror," *Opt. Commun.* **79**, 373-376 (1990).
17. V. T. Tikhonchuk, M. G. Zhanuzakov, and A. A. Zozulya, "Stationary states of two coupled double phase-conjugate mirrors," *Opt. Lett.* **16**, 288-290 (1991).
18. These equations are the same as those used in Ref. 10 but with the substitution  $\gamma \rightarrow -\gamma$ .

# Simple in-line method to measure the dispersion of an optical system

X. Steve Yao<sup>a)</sup> and Jack Feinberg

Departments of Electrical Engineering and Physics, University of Southern California, Los Angeles, California 90089-0484

(Received 17 July 1992; accepted for publication 1 December 1992)

We describe a simple in-line method to measure the dispersion of an optical system. The light beam passing through the optical system interferes with a reference beam in a spectrometer, and the resulting spectrum yields the quadratic and cubic dispersion terms of the system. We demonstrate this technique on an optical system made of grating pairs.

The group velocity dispersion of an optical system (for example, a laser cavity or a grating pair) changes the shape and duration of ultrashort pulses passing through the system. Because the amount of dispersion varies markedly with the particular path taken by the pulses as they pass through the system, it is preferable to use the aligned laser pulses themselves to measure the dispersion parameters of the system. In this letter, we describe such an in-line technique to determine the quadratic and higher order dispersion terms of an optical system. We note that our method is simple, accurate, sensitive, and can easily be applied to measure the dispersion of a femtosecond-laser cavity.

Our method is based on that of Shang<sup>1</sup> and others<sup>2,3</sup> for measuring the chromatic dispersion of an optical fiber. We split a wide bandwidth optical beam into two. We send one beam through the optical system whose dispersion is to be measured. The other beam is sent through air (or through a material with known dispersion). The two beams are recombined by a beamsplitter and sent into a spectrometer, where each of the corresponding frequency components of the two beams interferes. This spectral interference pattern yields the dispersion of the optical system, as we show below.

Note that because the coherence length of the optical beams may be very short, if their path lengths are sufficiently unequal the two beams may not spatially interfere at the entrance of the spectrometer. Nevertheless, each of their frequency components can interfere in the spectrometer, depending on the spectrometer's spectral resolution. For example, if the spectrometer has a spectral resolution of  $1 \text{ cm}^{-1}$  ( $\sim 30 \text{ GHz}$ ), then a spectral interference pattern will be obtained for relative path differences as long as 1 cm, even though the coherence length of the wide band source may only be a few microns. In our experiments, we use the subpicosecond pulses from a sync-pumped dye laser as the light source. We purposely choose the path difference of the two beams to be larger than the coherence length of the pulses but smaller than the inverse of the spectrometer's resolution in  $\text{cm}^{-1}$ . Because the two beams do not need to interfere outside of the spectrometer, the relative path delay does not have to be fixed at a precise value, in contrast to previous methods.<sup>4-6</sup>

Let the normalized power spectrum  $P(\Delta\omega)$  be defined as the ratio of the spectrum of the combined beam to the

spectrum of the reference beam, then we obtain:<sup>1-3</sup>

$$P(\Delta\omega) = P_0 [1 + m \cos[\Psi_0(\tau) + \tau\Delta\omega + \beta(\Delta\omega)^2 + \gamma(\Delta\omega)^3]] \quad (1)$$

where  $P_0$  is a real constant,  $m$  is the modulation of the spectral interference pattern,  $\Psi_0(\tau)$  is a phase,  $\tau$  is the group delay between the reference arm and the sample arm,  $\Delta\omega$  is the frequency measured from the center frequency  $\omega_0$ ,  $\beta$  is the quadratic dispersion term of the optical system, and  $\gamma$  is the cubic dispersion term. In deriving Eq. (1), we assume that the dispersive element has no frequency-dependent attenuation.

Values for both the quadratic dispersion term  $\beta$  and the cubic dispersion term  $\gamma$  can be obtained by curve fitting the measured normalized spectrum  $P(\Delta\omega)$  to Eq. (1). The signs of  $\beta$  and  $\gamma$  can be determined by adjusting the path lengths of the two arms so that the reference beam clearly arrives before the signal beam, for example, so that the time delay  $\tau$  in Eq. (1) is positive, and then constraining the curve fit to only positive values of  $\tau$ . The resulting signs of  $\beta$  and  $\gamma$  from the curve fit will then be correct.

We demonstrate our technique by measuring the dispersion of grating pairs.<sup>7-9</sup> Grating pairs have proved useful for pulse compression,<sup>9-11</sup> pulse shaping,<sup>12-14</sup> pulse encoding and decoding,<sup>15</sup> as well as dispersion compensation.<sup>16</sup> The various dispersion parameters of grating pairs can be calculated analytically,<sup>7,16</sup> although, to the best of our knowledge, no direct measurement of such values has been published to date. In principle, such dispersion parameters can be inferred by comparing the width of the autocorrelation trace of a known light pulse before and after traversing a grating pair. However, the change in the pulse's temporal shape caused by traversing a grating pair strongly depends on the frequency chirp and the amplitude envelope of the input light pulse, and these quantities are difficult to measure. Even if we knew the precise shape and chirp of our input pulse, taking the autocorrelation of the output pulse tends to smear out subtle pulse shape changes caused by the optical system, and this limits the accuracy of autocorrelation for determining the dispersion parameters of an optical system. However, using the spectral interference method described above, we can easily and accurately determine the dispersion parameters of a grating pair.

Figure 1 shows the incoming laser beam was split into two by the first grating of the grating pair. The zero-order

<sup>a)</sup>Present address: Jet Propulsion Laboratory, Mail Stop 298-100, 4800 Oak Grove Dr., Pasadena, CA 91109.

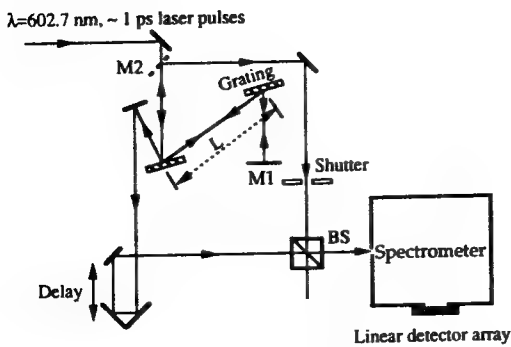


FIG. 1. In-line measurement of a grating pair's dispersion properties. The optical path length difference is chosen to be larger than the coherence length of the two beams so that they do not interfere outside of the spectrometer. However, in the spectrometer, each frequency component from the two beams interferes to create a spectral interference pattern.

beam reflected from the first grating was used as the reference beam. The first-order diffraction was sent to a second grating aligned parallel to the first. The beam diffracted in first order off the second grating was retroreflected by a mirror  $M_1$  to double pass the grating pair in order to double the group velocity dispersion and to eliminate spatial walkoff of the different temporal frequency components. Both of the gratings were mounted on a precision optical rail so that the spacing between them could be accurately varied. The mirror  $M_1$  was mounted together with the second grating to avoid changing the direction of the reflected beam when sliding the second grating on the rail. Also, the retroreflecting mirror  $M_1$  was tilted downwards a bit so that the backward going beam could be picked off by mirror  $M_2$  which lay below the incident beam in the plane of the figure. The grating spectrometer had a spectral resolution of  $1 \text{ cm}^{-1}$ . Its output spectrum was measured by a 512 element linear detector array and displayed on a digital oscilloscope. Data were transferred to a computer and fit to Eq. (1). By closing a shutter placed in the path of the sample beam, the spectrum of just the laser source could also be measured. The ratio of these two spectra is the normalized interferometric spectral curve  $P(\Delta\omega)$  defined in Eq. (1).

Figure 2(a) shows spectral curves measured with the shutter open and closed, and Fig. 2(b) shows the normalized interferometric spectrum  $P(\Delta\omega)$  obtained by taking the ratio of the two curves in Fig. 2(a). The effect of chirp (or group velocity dispersion) can be seen from the spectral curve; its periodicity changes as a function of frequency. Also shown is the fit to the data of Eq. (1). Although there are 6 parameters in Eq. (1), the amplitude  $P_0$  and the modulation  $m$  are not critical and are fixed once having been chosen properly. Consequently, there are only four parameters to be determined from fitting 250 data points.

Figures 3(a) and 3(b) show how the quadratic and cubic dispersion terms vary with the spacing  $L$  between the midpoints of the two gratings. (The grating spacing  $L$  was measured along the direction of the optical rail, as indicated in Fig. 1.) The measured  $\beta$  is negative and scales linearly with the grating separation  $L$ , in agreement with

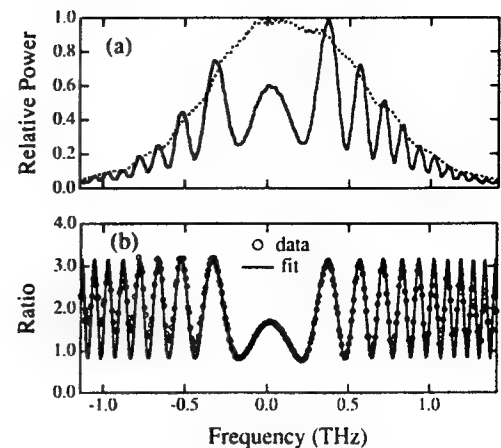


FIG. 2. (a) Dotted line: The laser spectrum. Solid line: A typical spectral interference pattern, (b) circles: the normalized spectral interference pattern (the ratio of the two curves above), solid line: its fit. The spectral curve's periodicity changes with frequency due to the dispersion of the grating pair.

analytical results.<sup>7,16</sup> For each  $L$ , we also tried varying the relative delay between the two beams and then fitting each set of data to Eq. (1). The values of the quadratic dispersion term obtained from our curve fits are consistent from set to set, while the values of the cubic dispersion term are small and fluctuate. Our measurement accuracy increases with the spectral width of the light source; our laser was sufficiently broad to accurately determine the quadratic dispersion term  $\beta$  but not the cubic term  $\gamma$ . (On the other hand, if the spectral width of the laser pulses is too narrow to measure  $\gamma$ , then  $\gamma$  will have little effect on these pulses and its value is unimportant.) By using a light source with a wider spectral width, for example a LED or a femtosecond laser, the cubic dispersion term  $\gamma$  can also be measured accurately. Figure 3(b) shows that despite the inaccuracy in  $\gamma$ , its sign and magnitude are consistent with theory.<sup>7,16</sup>

We also measured the quadratic dispersion term  $\beta$  of a Martinez type<sup>8,9</sup> grating pair aligned to have nominally zero dispersion. Such a grating pair can be made into a

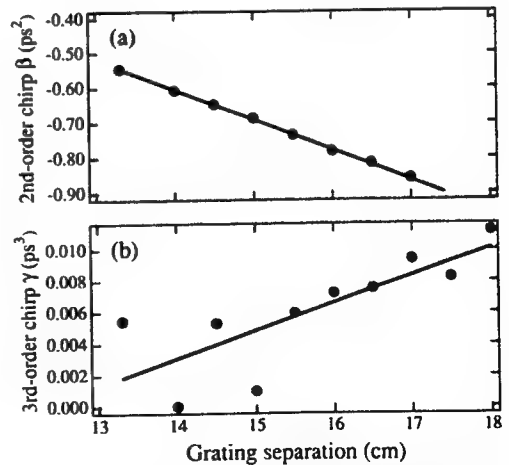


FIG. 3. (a) The quadratic dispersion parameter  $\beta$ , and (b) the cubic dispersion parameter  $\gamma$  of the grating pair as a function of the separation  $L$  between the two gratings.

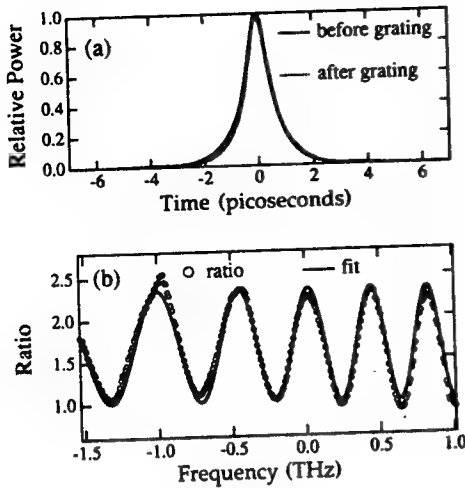


FIG. 4. Measurement of the dispersion parameter of a Martinez-type grating pair arranged for zero dispersion. (a) Second harmonic generation autocorrelation traces of pulses before and after going through the grating pair. Notice that the two traces appear almost identical (b) Spectral interferometric pattern. A chirp (variation in periodicity) is clearly seen. A curve fit yields a dispersion of  $\beta=0.043 \text{ ps}^2$ .

pulse shaping apparatus<sup>12-15</sup> by inserting a phase or an amplitude mask between the two gratings. First, we tried to measure  $\beta$  conventionally by comparing the autocorrelation of our laser pulses before and after the grating pair. Figure 4(a) shows that these two traces were almost identical, implying that  $\beta \approx 0$ . We then applied our spectral interferometric method using the same laser pulses; the periodicity variation of the resulting spectral interference pattern can be seen clearly in Fig. 4(b), which yields a value of  $\beta=0.043 \text{ ps}^2$ . This demonstrates that the spectral interferometric method described here is more sensitive and more accurate in characterizing a dispersive optical system than is comparing the autocorrelation shape of laser pulses before and after the system.

This method may also be applied to measure the dispersion coefficients of a laser cavity having many dispersive elements, and thus may prove useful in the design and characterization of ultrashort pulse systems. In principle, high-order dispersion terms can be measured if the spectral width of the light source is sufficiently broad.

In conclusion, we have demonstrated an in-line method to measure the dispersion coefficients of a grating pair (or other optical system). This method is direct, accurate, and relatively easy in comparison with other methods.<sup>4-6</sup>

This work supported by Contract F49620-91-C-0028 of the Joint Services Electronics Program and by Contract No. F49620-92-J-0022 of the Air Force Office of Scientific Research.

- <sup>1</sup>H. T. Shang, Electron. Lett. **17**, 603 (1981).
- <sup>2</sup>J. Stone and D. Marcuse, Electron. Lett. **20**, 751 (1984).
- <sup>3</sup>P. Merritt, R. P. Tatam, and D. A. Jackson, J. Lightwave Technol. **7**, 703 (1989).
- <sup>4</sup>L. G. Cohen and J. Stone, Electron. Lett. **18**, 564 (1982).
- <sup>5</sup>W. H. Knox, N. M. Pearson, K. D. Li, and C. A. Hirliemann, Opt. Lett. **13**, 574 (1988).
- <sup>6</sup>K. Naganuma, K. Mogi, and H. Yamada, Opt. Lett. **15**, 393 (1990).
- <sup>7</sup>E. D. Treacy, IEEE J. Quantum Electron. **QE-5**, 454 (1969).
- <sup>8</sup>O. E. Martinez, J. P. Gordon, and R. L. Fork, J. Opt. Soc. Am. B **1**, 1003 (1984).
- <sup>9</sup>O. E. Martinez, IEEE J. Quantum Electron. **QE-23**, 59 (1987).
- <sup>10</sup>C. V. Shank, R. L. Fork, R. Yen, R. H. Stolen, and W. J. Tomlinson, Appl. Phys. Lett. **40**, 761 (1982).
- <sup>11</sup>B. Nikolaus and D. Grischkowsky, Appl. Phys. Lett. **42** (1983).
- <sup>12</sup>J. Agostinelli, G. Harvey, T. Stone, and C. Gabel, Appl. Opt. **18**, 2500 (1979).
- <sup>13</sup>A. M. Weiner, J. P. Heritage, and E. M. Kirschner, J. Opt. Soc. Am. B **5**, 1563 (1988).
- <sup>14</sup>A. M. Weiner, D. E. Leaird, J. S. Patel, and J. R. Wullert, Opt. Lett. **15**, 326 (1990).
- <sup>15</sup>A. M. Weiner, J. P. Heritage, and J. A. Salehi, Opt. Lett. **13**, 300 (1988).
- <sup>16</sup>A. Frenkel, J. P. Heritage, and M. Stern, IEEE J. Quantum Electron. **25**, 1981 (1989).

# Photorefractive pulse coupling in the frequency domain

X. Steve Yao and Jack Feinberg

Departments of Electrical Engineering and Physics, University of Southern California, Los Angeles, California 90089-0484

Received August 18, 1992

We performed experiments to verify the theory of photorefractive pulse coupling in the frequency domain. In particular, we confirm that the phase added to the diffracted pulse depends quadratically on the relative delay between the two input pulses.

A theory to describe the coupling of trains of picosecond pulses in a photorefractive crystal was recently published,<sup>1</sup> and a test of this theory was performed in the time domain.<sup>2</sup> Although these temporal measurements showed good agreement with theory, a more definitive test can be performed in the frequency domain. In particular, one can drop the assumptions of Ref. 1 that all the optical pulses have the same amplitude and that the phase fluctuations of the pulses have a particular (Gaussian) form. Here we compare theory and experiment by measuring the frequency spectrum of optical pulses before and after coupling in a photorefractive crystal. In particular, we confirm the peculiar prediction<sup>1</sup> that the phase of the diffracted pulse depends quadratically on the relative delay between the incoming pump and signal pulses.

After a beam of weak signal pulses intersects with a beam of strong pump pulses in a photorefractive crystal, the field amplitude of the signal pulses is<sup>1</sup>

$$E_{\text{shaped}}(t) = E_{\text{signal}}(t) + G(\tau)[\exp(\eta L) - 1]E_{\text{pump}}(t), \quad (1)$$

where  $\eta$  is the two-beam coupling coefficient,  $L$  is the interaction length of the two beams,  $E_{\text{shaped}}(t)$  is the field amplitude of the shaped signal pulse after the crystal, and  $E_{\text{signal}}(t)$  and  $E_{\text{pump}}(t)$  are the amplitudes of the signal pulse and the pump pulse before the crystal, respectively. In Eq. (1), the complex correlation function  $G(\tau)$  is

$$G(\tau) = \int_{-\infty}^{\infty} \overline{E_{\text{signal}}(t)E_{\text{pump}}^*(t - \tau)} dt / I_0 \\ = |G(\tau)| \exp[i\phi_{\text{diff}}(\tau)]. \quad (2)$$

In Eq. (2),  $I_0$  is proportional to the total intensity in the crystal and is a constant both in time and in space. We take the ensemble average (denoted by the overbar) because the laser pulses are not identical and the crystal's response time is much longer than the time between pulses.

In Eq. (1), the second term is the diffracted portion of the pump pulse, which is added to the signal pulse (the first term) to alter the temporal shape of the signal pulse. Because  $G(\tau)$  is complex, the diffracted portion of the pump pulse receives an additional phase  $\phi_{\text{diff}}(\tau)$  before it is added to the signal pulse.

In order to verify Eq. (1), we need to compare the theoretical value of the phase  $\phi_{\text{diff}}(\tau)$  with the experimentally measured value, and this is difficult to do in the time domain. However, we can accurately determine  $\phi_{\text{diff}}(\tau)$  from the measured frequency spectrum of the shaped signal pulses as follows.

The field envelopes  $E_{\text{shaped}}(t)$ ,  $E_{\text{signal}}(t)$ , and  $E_{\text{pump}}(t)$  can be expressed in the frequency domain by taking a Fourier transform:

$$E(t) = \frac{1}{2\pi} \int_{-\infty}^{\infty} F(\omega) \exp(-i\omega t) d\omega, \quad (3)$$

where  $F(\omega)$  is the complex spectral amplitude of a pulse. Substituting Eq. (3) into Eq. (1), we obtain the spectral power gain of the signal beam:

$$\frac{|F_{\text{shaped}}(\omega)|^2}{|F_{\text{signal}}(\omega)|^2} \\ = a(\tau) \{ 1 + b(\tau) \cos[\phi_{\text{diff}}(\tau) - \tau\omega - \beta\omega^2] \}, \quad (4)$$

where<sup>3</sup>

$$\phi_{\text{diff}}(\tau) = \frac{1}{2} \tan^{-1} \frac{\beta}{\alpha} - \frac{\beta}{4(\alpha^2 + \beta^2)} \tau^2. \quad (5)$$

In deriving Eq. (4), we assume that the signal pulse is derived from the pump pulse by sending the pump pulse through a Treacy grating pair,<sup>4</sup> so that  $F_{\text{signal}}(\omega) = A_1 F_{\text{pump}}(\omega) \exp(i\beta\omega^2)$ , where  $\beta$  is the chirp parameter of the grating pair. We also assume that the laser pulses have a Gaussian frequency spectrum with a spectral width parameter  $\alpha$ :  $|F_{\text{pump}}(\omega)|^2 = A_2 \exp(-\alpha\omega^2)$ . Here  $A_1$  and  $A_2$  are real constants.

In Eq. (4),  $a(\tau)$  and  $b(\tau)$  are real functions of the relative delay  $\tau$  and the coupling gain coefficient  $\eta$ .  $b(\tau)$  is positive when the crystal is oriented so that the signal beam gains energy and negative when the signal beam loses energy. The value of  $a(\tau)$  is always positive. Their exact values are not of interest here.

If the theory of photorefractive pulse coupling is correct, then a plot of the measured spectral power gain versus frequency should fit to Eq. (4). Namely, the spectral power gain should be a sinusoidal function of frequency with a varying periodicity, its periodicity should increase linearly with the relative delay of the two beams, and the variation in the periodicity should depend on the chirp parameter  $\beta$ . Most importantly, the previously elusive phase

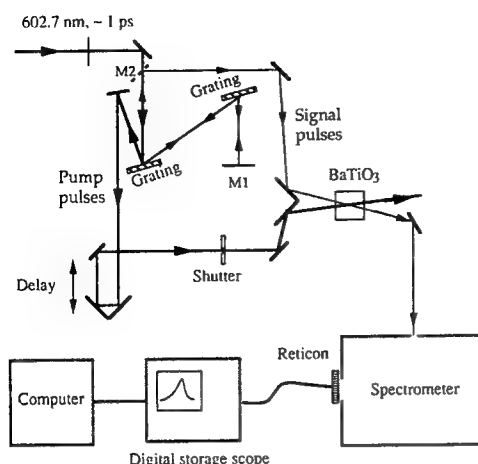


Fig. 1. Experimental setup for measuring the change in the optical spectrum of the signal pulses that is due to photorefractive pulse coupling. The grating pair chirps the signal pulses before they intersect with the pump pulses in the  $\text{BaTiO}_3$  crystal. Mirror M1 is tilted downward a bit so that the backward-going beam could be picked off by mirror M2, which lies below the incident beam in the plane of the figure. By opening and closing the shutter, we measure the spectra of the signal beam with and without beam coupling. The pump laser is not transform limited; it has a frequency-time product of  $\Delta\nu\Delta\tau = 1$ .

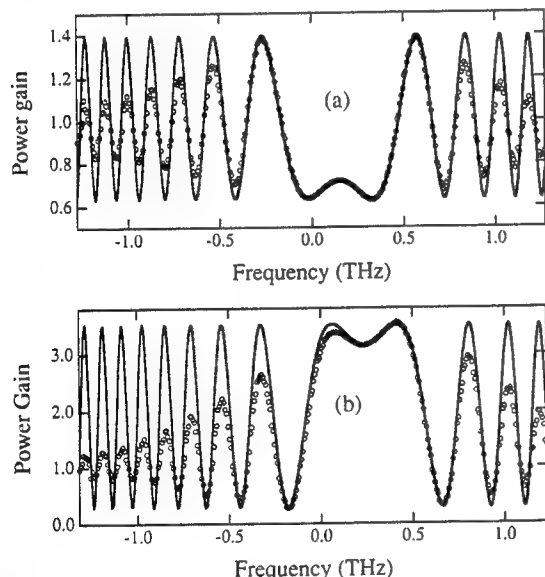


Fig. 2. Power gain of the signal pulse as a function of optical frequency. (a) The crystal is oriented so that the signal beam loses energy, (b) the crystal is rotated 180° so that the signal pulse now gains energy. As predicted, the gain of the signal beam is a sinusoidal function of frequency with a varying periodicity. The solid curve is a fit to the data (circles). The roll-off in the wings is discussed in the text.

$\phi_{\text{diff}}(\tau)$  can now be determined, and, according to Eq. (5), this phase should vary quadratically with the delay time  $\tau$  between the two beams.

Figure 1 shows how double passing a Treacy grating pair<sup>4</sup> imparted a linear frequency chirp to the signal beam's pulses and so broadened their temporal profile without changing their frequency spectrum.

The signal beam intersected with an unaltered pump beam in the photorefractive  $\text{BaTiO}_3$  crystal at a full exterior crossing angle of 14°. After the two beams coupled in the crystal, the frequency spectrum of the signal beam was analyzed and stored by a 1-cm<sup>-1</sup> resolution spectrometer system. By either blocking or unblocking the pump beam, we could measure the spectra of the signal beam without and with photorefractive coupling. The ratio of these two measurements is the normalized spectral power gain of Eq. (4).

Figure 2 shows typical experimental spectral power gain curves and their theoretical fits for the cases in which the  $\text{BaTiO}_3$  crystal was oriented to make the signal beam gain energy [Fig. 2(a)] or lose energy [Fig. 2(b)]. Zero frequency in these figures corresponds to the center frequency of the laser pulses, which was arbitrarily chosen to be at the peak of the laser power spectrum. As predicted by Eq. (4), the spectral gain curves are sinusoidal functions of frequency with a changing periodicity. The reason that the amplitudes of the measured curves diminish in the wings of the graph while the theoretical curves do not is that the theory of Ref. 1 assumed that the photorefractive gratings written by the various frequency components were indistinguishable and that all frequency components of a pulse were perfectly phase matched to the photorefractive grating. However, in our experiment, the spectral width of the pulses was sufficiently wide to violate these condi-

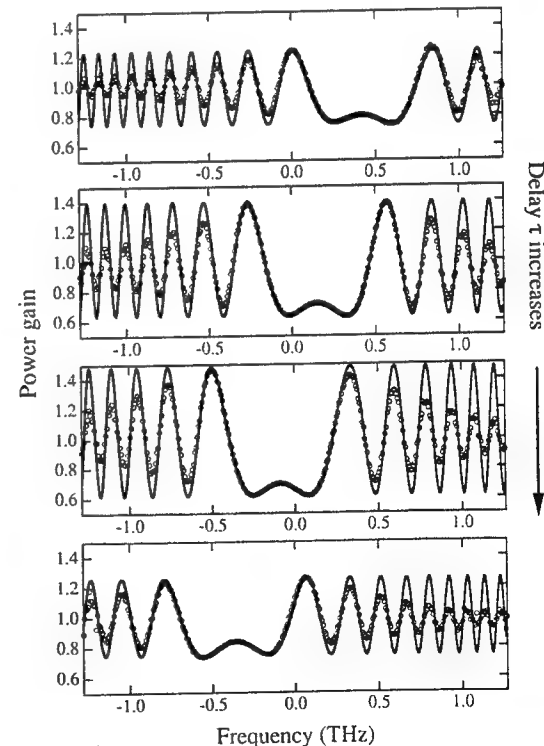


Fig. 3. Spectral gain curve as a function of the relative delay  $\tau$  between the pump and the signal pulses. Here the crystal is oriented so that the signal beam loses energy. The value of  $\phi_{\text{diff}}(\tau)$  determines the position of the center lobe of each gain curve. We obtain a value of  $\phi_{\text{diff}}(\tau)$  for each delay  $\tau$  by curve fitting the corresponding gain curves.

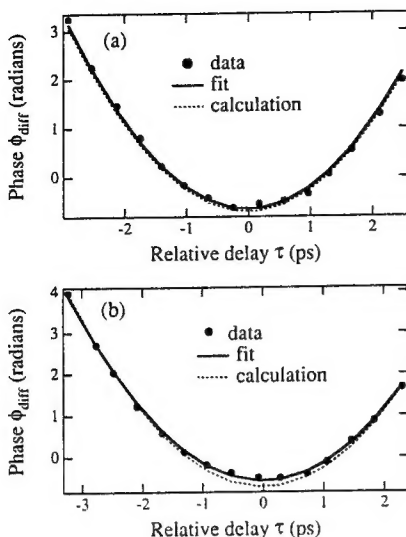


Fig. 4. Phase  $\phi_{\text{diff}}(\tau)$  of the spectral gain as a function of delay  $\tau$ , as determined by curve fits such as shown in Fig. 3. The crystal is oriented for the signal pulse (a) to gain energy and (b) to lose energy. The data (filled circles) are fitted to a quadratic function of the delay (solid curve). Both the data and the fits are in good agreement with the theoretical calculations (dotted curve).

tions. Nevertheless, the parameters that we obtain from the curve fitting, namely the delay  $\tau$  (which determines the periodicity), the chirp parameter  $\beta$  (which determines the periodicity variation), and the phase of the cosine function (which determines the center of the curve), are all insensitive to the amplitude of the cosine wave. Therefore, despite the fall-off in amplitude, we could accurately fit these three parameters.

We measured a series of spectral gain curves for different time delays and fit each curve to theory. Figure 3 is an example for the case in which the crystal was oriented to make the signal beam lose energy. To analyze our data, we first used a spectral interferometric method<sup>5</sup> to measure independently the chirp parameter  $\beta$  of the grating pair. Namely, we replaced the BaTiO<sub>3</sub> crystal with a beam splitter and obtained  $\beta$  from curve fitting the spectral interference pattern of the chirped and unchirped pulses.<sup>5</sup> The value of  $\beta$  that we obtained was  $-0.54 \text{ ps}^2$ . We found that the chirp parameter  $\beta$  of the grating pair obtained from each curve fit in Fig. 3 was identical to that obtained by the spectral interferometric method and that the phase  $\phi_{\text{diff}}(\tau)$  of the curves indeed had a quadratic dependence on the delay, as shown in Fig. 4. The phases obtained by curve fitting were  $\phi_{\text{diff}}(\tau) = -0.58 + 0.43\tau^2$  for the case when the signal beam gained energy and  $\phi_{\text{diff}}(\tau) = -0.66 + 0.45\tau^2$  for the case when the signal beam lost energy, where  $\tau$  is in picoseconds. For comparison, the phase calculated from Eq. (5) was  $\phi_{\text{diff}}(\tau) = -0.72 + 0.45\tau^2$

for both cases. We used an  $\alpha$  coefficient of 0.069 and  $0.076 \text{ ps}^2$  in the calculation for the two cases, respectively, which we obtained by measuring the widths of the laser power spectra in the corresponding experiments. From Fig. 4 one can see that the quadratic coefficients predicted by the theory of Ref. 1 are close to those obtained from curve fitting.

On the other hand, the constant term in the expressions for  $\phi_{\text{diff}}(\tau)$  obtained theoretically and from the data are not in as good agreement. This is because in deriving Eq. (5) we assume that the power spectrum of the laser is a Gaussian function of frequency, which makes it symmetric and gives it a well-defined center. However, the actual measured spectra are asymmetric and have a poorly defined center frequency (or zero frequency).

The quadratic phase dependence of the diffracted field on the relative delay is a direct confirmation that the average power gain of the signal beam is proportional to the magnitude squared of the second-order field correlation function, as predicted by Ref. 1. A different theory,<sup>6</sup> which predicts that the average power gain of the signal beam is proportional to the fourth-order field correlation function, cannot provide any phase information and so cannot predict the observed dependence of  $\phi_{\text{diff}}(\tau)$  on  $\tau$ .

In summary, we have experimentally confirmed the predictions of Ref. 1 that describe the interaction of short optical pulses in a photorefractive crystal. We expect that this theory can prove useful for analyzing photorefractive effects and their applications with short optical pulses.

We gratefully acknowledge support from the Joint Services Electronics Program and U.S. Air Force Office of Scientific Research contract F49620-92-J-0022. We thank V. Dominic for his legendary expertise.

## References

1. X. S. Yao, V. G. Dominic, and J. Feinberg, *J. Opt. Soc. Am. B* **7**, 1295 (1990).
2. X. S. Yao and J. Feinberg, "Temporal shaping of optical pulses by beam coupling in a photorefractive crystal," *Opt. Lett.* (to be published).
3. X. S. Yao, "Optical pulse coupling in a photorefractive crystal, propagation of encoded pulses in an optical fiber, and phase conjugate optical interconnections," Ph.D. dissertation (University of Southern California, Los Angeles, Calif., 1992).
4. E. D. Treacy, *IEEE J. Quantum Electron.* **QE-5**, 454 (1969).
5. X. S. Yao and J. Feinberg, "A simple, in-line method to measure the dispersion of an optical system," *Appl. Phys. Lett.* (to be published).
6. R. Trebino, C. C. Hayden, A. M. Johnson, W. M. Simpson, and A. M. Levine, *Opt. Lett.* **15**, 1079 (1990).

# Temporal shaping of optical pulses using beam coupling in a photorefractive crystal

X. Steve Yao\* and Jack Feinberg

Departments of Physics and Electrical Engineering, University of Southern California, Los Angeles, California 90089-0484

Received August 31, 1992

We coupled trains of subpicosecond laser pulses in a photorefractive crystal to confirm that such coupling alters the temporal shapes of the optical pulses. Our measured pulse shapes are in good agreement with theory.

Photorefractive crystals are candidates for measuring,<sup>1,2</sup> shaping,<sup>3</sup> and storing<sup>4</sup> ultrashort optical pulses. When two optical pulses couple in a photorefractive crystal, their temporal shapes are altered. In a previous paper we predicted the expected change in the temporal shape of a weak signal pulse,<sup>3</sup> and in this Letter we experimentally measure such pulse-shape changes. In particular, we consider the case in which the two interacting pulses have the same frequency spectrum but quite different temporal widths. If the photorefractive crystal is oriented so that the signal beam gains energy from two-beam coupling in the crystal, then our calculations predict (and our experiments here confirm) that a sharp spike is added onto the signal pulse's envelope. If the crystal is instead oriented so that the signal beam loses energy, then a hole appears in the wide temporal envelope of the signal pulse.

In our experiments we derive both the pump and the signal pulses from a Kiton-red dye laser ( $\lambda = 603$  nm) that is synchronously pumped by a mode-locked and frequency-doubled cw Nd:YAG laser at a repetition rate of 76 MHz. A Treacy grating pair<sup>5</sup> stretches the signal pulses in time, as shown in Fig. 1. The beam reflected from the first grating (i.e., the zero-order diffraction) serves as the pump beam. Because the pump beam's pulses are simply reflected from the grating, they have the same temporal shape as the dye-laser's pulses. These pump pulses travel through a delay line to intersect the signal pulses in a photorefractive BaTiO<sub>3</sub> crystal.

We allow many ( $10^9$ ) pairs of laser pulses from the pump beam and the signal beam to slowly build a photorefractive grating in the crystal. (It takes approximately 15 s.) The total average optical power entering the crystal is  $\sim 15$  mW, and the beam diameter is 1 mm, which yields a fluence of  $\sim 20$  nJ/cm<sup>2</sup>. At this fluence any free-carrier gratings in the photorefractive crystal can be safely neglected.<sup>6</sup>

The BaTiO<sub>3</sub> crystal named "Swiss" is oriented so that its surface normal makes an angle of 36° with the bisector of the two incident light beams, with the pump beam lying nearer to the surface normal. The polarizations of the two beams are extraordinary, and their full crossing angle is 14° outside the crystal. The coupling coefficient for the signal beam can be switched from positive (gain) to negative (loss) by

rotating the crystal by 180° about a vertical axis. The measured intensity gain of the signal beam in the crystal is typically 16. We use a vibrating motor mounted beneath the BaTiO<sub>3</sub> crystal to conveniently switch the beam coupling on or off; turning on the motor vibrates the crystal sufficiently to eliminate all beam coupling.

We measure the temporal shapes of our beams using an intensity cross-correlation method<sup>7</sup> in a second-harmonic-generating (SHG) crystal. For convenience we use the pump pulse transmitted through the BaTiO<sub>3</sub> crystal as the short reference pulse of our cross correlator.

Figure 2 shows the measured pulse shapes of the signal beam after the BaTiO<sub>3</sub> crystal. In these plots the crystal is oriented so that the signal beam gains energy. For each successive plot in Fig. 2 the pump beam's delay is increased by 1.32 ps with respect to the signal beam. One can see that a sharp spike is added onto the signal pulse and that the spike's

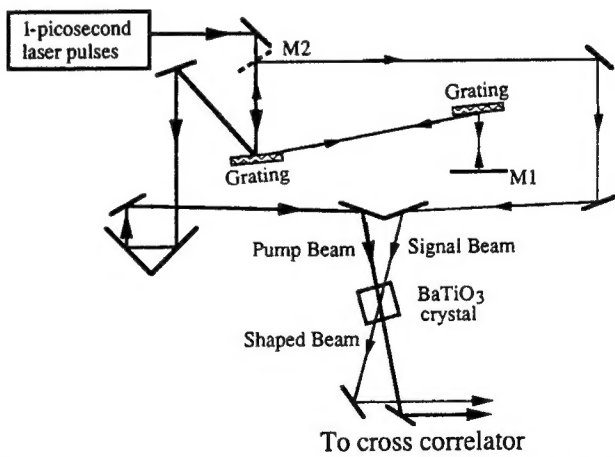


Fig. 1. Experimental setup for measuring pulse-shape changes caused by two-beam coupling in a photorefractive crystal. The signal pulse was first broadened by a factor of 12 using a grating pair and then made to intersect a strong pump pulse in a BaTiO<sub>3</sub> crystal. Mirror M1 was tilted slightly downward to deflect the backward-going beam slightly below the forward-going beam, where it could be picked off by mirror M2. The shape of the signal pulse was measured by using cross correlation in a second-harmonic-generating crystal.

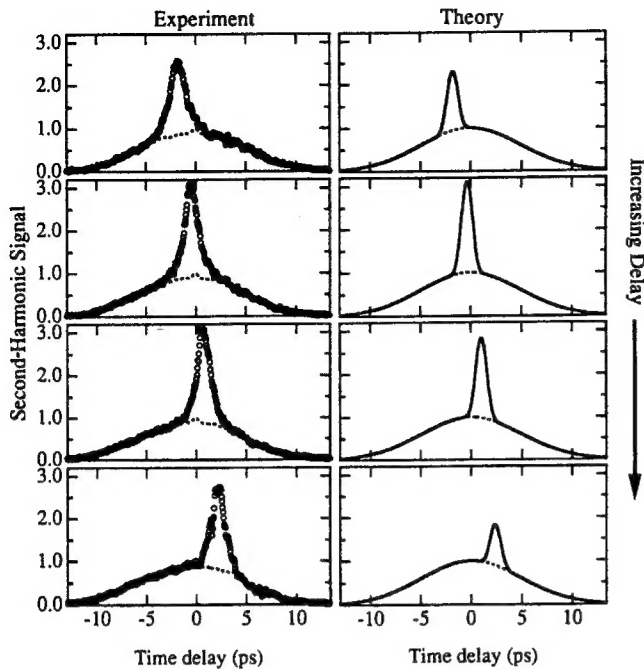


Fig. 2. Pulse shaping using beam coupling in a BaTiO<sub>3</sub> crystal. The crystal is oriented so that the signal beam gains energy from the pump beam. Before entering the crystal, the signal pulses had been temporally stretched by a factor of 12 by a Treacy grating pair. Left column, experimental data: The dashed curve is the temporal profile of the original signal pulses (actually the cross correlation of the signal and the pump). The circles are the shaped signal pulses after the crystal. The BaTiO<sub>3</sub> crystal added a sharp spike (corresponding to the sharp pump pulse) onto the signal pulse. The pump beam's delay was increased by 1.32 ps for each successive graph, and the position of the spike moved accordingly. Right column, theoretical curves: The dashed curve is the calculated temporal profile (cross correlation of the signal and the pump) of the original signal pulses. The solid curve is the temporal profile of the shaped pulses.

location changes as the relative delay between the two beams changes.

In Fig. 3 we rotate the BaTiO<sub>3</sub> crystal by 180°, so that the signal beam now loses energy to the pump beam by two-wave mixing. As expected, a dip is now carved out of the wider pulse wherever the short pump pulse overlaps it.

In the experiments above we measure not the actual temporal profile of the shaped pulse but the average intensity cross correlation of the shaped pulse and the pump pulse after the photorefractive crystal<sup>8</sup>:

$$I^{2\omega}(\tau) \propto \overline{\int_{-\infty}^{\infty} |E_{\text{shaped}}(t)|^2 |E_{\text{sharp}}(t - \tau)|^2 dt}, \quad (1)$$

where  $I^{2\omega}(\tau)$  is the second-harmonic signal from the SHG crystal and  $E_{\text{shaped}}(t)$  and  $E_{\text{sharp}}(t)$  are the optical electric-field envelopes of the shaped and the sharp pulses incident upon the SHG crystal. The overbar in relation (1) denotes an ensemble average, which is required because the speed of our detector is much slower than the pulse repetition rate and because our laser pulses are not identical. Although in general

laser pulses may fluctuate both in amplitude and in phase, here we choose (as in Ref. 3) to model our laser pulses as having deterministic amplitudes but randomly varying phases. We express<sup>3,9</sup> the optical electrical field as  $E_{\text{sharp}}(t) = E_0 T_{\text{sharp}}(t) u_{\text{sharp}}(t)$ , where  $E_0$  is the real peak field amplitude of a pump pulse,  $T_{\text{sharp}}(t)$  is the complex normalized deterministic field envelope of a pump pulse, and  $u_{\text{sharp}}(t)$  represents the phase fluctuations of a pump pulse. For the pulse considered here, the envelope of the short pump pulse is relatively unchanged by its passage through the photorefractive crystal, so that  $T_{\text{sharp}}(t) \approx T_{\text{pump}}(t)$ , where  $T_{\text{pump}}(t)$  is the normalized field envelope of the pump pulse incident upon the photorefractive crystal.

Reference 3 provides the following equation for the remaining factor  $E_{\text{shaped}}$  in relation (1):

$$|E_{\text{shaped}}(t)|^2 = A |T_{\text{wide}}(t) + g_{\text{eff}}(\tau) T_{\text{sharp}}(t - \tau)|^2, \quad (2)$$

where  $T_{\text{wide}}(t)$  is the deterministic normalized amplitude of the wide signal pulse incident upon the photorefractive crystal and  $A$  is a real constant. In Eq. (2), the first term on right-hand side is the deterministic field envelope of the transmitted signal beam and the second term is the diffracted field envelope from the pump beam. The effective complex field gain parameter  $g_{\text{eff}}(\tau)$  in Eq. (2) is defined as

$$g_{\text{eff}}(\tau) = (\langle |T_{\text{wide}}|^2 \rangle^{1/2} / \langle |T_{\text{sharp}}|^2 \rangle^{1/2}) \times [\exp(\eta L) - 1] \gamma_{12}^D(\tau) |\gamma_{12}^R(\tau)|, \quad (3)$$

where  $L$  is the crystal length and  $\eta$  is the two-beam field coupling gain per unit length. The angle

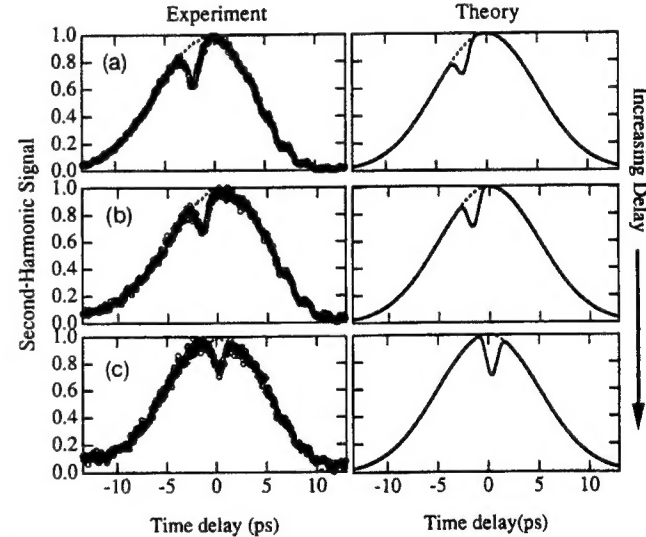


Fig. 3. Similar to Fig. 2, except that here the BaTiO<sub>3</sub> crystal had been rotated by 180° to make the signal beam lose energy to the pump beam through two-beam coupling. A dip was carved out of the wider signal pulse whenever the sharp pump pulse overlapped it, and the position of this dip changed according to the relative delay between the pump beam and the signal beam. From (a) to (b) this delay was changed by 0.68 ps, and from (b) to (c) the delay was changed by an additional 1.16 ps. For the corresponding theoretical calculations we used the same experimentally determined parameters as in Fig. 2, except now  $\eta L = -1.38$  (corresponding to the signal beam's losing energy to the pump beam).

brackets stand for a time average. In Eq. (3),  $\gamma_{12}^D(\tau)$  is the deterministic envelope correlation function, which is set by the overlap of the two pulses, and  $\gamma_{12}^R(\tau)$  is the mutual coherence function,<sup>10</sup> which takes into account the effect of random phase fluctuations of the optical field from pulse to pulse. These two functions are defined as

$$\gamma_{12}^D(\tau) = \langle T_{\text{wide}}(t)T_{\text{sharp}}^*(t-\tau) \rangle / [\langle |T_{\text{wide}}(t)|^2 \rangle \times \langle |T_{\text{sharp}}(t)|^2 \rangle]^{1/2}, \quad (4)$$

$$\gamma_{12}^R(\tau) = \frac{u_{\text{wide}}(t)u_{\text{sharp}}^*(t-\tau)}{u_{\text{wide}}(t)u_{\text{sharp}}^*(t)}, \quad (5)$$

To calculate  $|E_{\text{shaped}}(t)|^2$ , the incoming laser pulse's deterministic amplitude  $T_{\text{sharp}}(t)$  and phase fluctuations must first be determined. We measured the spectral width of our dye laser pulses to be  $\Delta\nu = 1.75$  THz, and their temporal width to be  $\tau_p = 1$  ps. (The large value of the product  $\tau_p\Delta\nu = 1.75$  indicates that the dye-laser pulses had either chirp or phase fluctuations, or both.) For simplicity, we assume that  $T_{\text{sharp}}(t)$  is a chirped Gaussian:  $T_{\text{sharp}}(t) = \exp[-a(1 + i\chi)t^2]$ , where  $\chi$  accounts for any chirp present on the sharp laser pulses and  $a = 2 \ln 2/\tau_p^2$ .

We use an in-line method<sup>11</sup> to measure the dispersion parameter  $\beta$  of the Treacy grating pair: We interfere, in a 1-m grating spectrometer, the stretched signal beam with an unstretched beam, and then curve fit the resulting spectral interference pattern. We obtain  $\beta = -0.54$  ps<sup>2</sup>. We then calculate the chirp parameter  $\chi$  by measuring the stretching ratio  $q$  of the pulses before and after the grating pair and comparing the measured value  $q = 12$  with the theoretical value<sup>12</sup>  $q = [1 + 2\chi(4\alpha\beta) + (4\alpha\beta)^2(1 + \chi^2)]^{1/2}$  to obtain  $\chi = -3.4$ .  $T_{\text{wide}}(t)$  is then calculated from  $T_{\text{sharp}}(t)$  and  $\beta$ .<sup>12</sup>

The phase fluctuations of the pulses are characterized by a phase coherence time  $\tau_s$  defined by Eq. (31) of Ref. 3. We determine  $\tau_s$  for our pulses by measuring their spectral widths and comparing them with the theoretical value<sup>12</sup>  $\Delta\nu = (2 \ln 2/\pi\tau_p)[1 + \chi^2 + (\tau_p/\tau_s)^2]^{1/2}$  to obtain  $\tau_s = 0.55$  ps. The mutual coherence function  $\gamma_{12}^R(\tau)$  is then calculated<sup>12</sup> from  $\tau_s$ .

Finally, using relations (1) and (2) and our experimentally determined parameters  $\tau_p = 1$  ps,  $\tau_s = 0.55$  ps,  $\chi = -3.37$ ,  $\beta = -0.54$  ps<sup>2</sup>, and  $|\eta L| = 1.38$ , we obtain the theoretical curves shown in Figs. 2 and 3. These curves have no free parameters, yet they agree reasonably well with our experimental curves. However, for large delay  $|\tau|$ , the height of the spike and the depth of the dip in the theoretical curves decrease slightly faster than those of the corresponding experimental curves, probably because the temporal shapes of the signal and pump pulses are not truly Gaussian.

Note that the dips in the experimental curves in Fig. 3 are not so deep as previously predicted.<sup>3</sup>

When calculating the curves in Ref. 3, we assumed that the pulses from the laser were transform limited, i.e., that the laser pulses had no phase fluctuations ( $\tau_s = \infty$ ) and no chirp ( $\chi = 0$ ). However, in our actual experiments the dye-laser pulses had both phase fluctuations and chirp. Our analysis<sup>12</sup> shows that in order for the pulse-shaping technique to be most effective, the initial laser pulses should be transform limited.

Photorefractive pulse shaping can be used to generate dark optical pulses. However, photorefractive pulse shaping is not so flexible as the method proposed by Weiner *et al.*<sup>13</sup> for generating arbitrarily shaped pulses.

In summary, we have demonstrated temporal pulse shaping using two-beam coupling in a photorefractive crystal. We have measured the temporal shape of a temporally stretched pulse after it coupled with a strong, nonstretched pulse in a photorefractive BaTiO<sub>3</sub> crystal and found good agreement with theory.

This research is supported by contract F49620-92-J-0022 of the Air Force Office of Scientific Research and by the Joint Services Electronics Program. We thank A. M. Johnson for helpful discussions.

\*Present address, Jet Propulsion Laboratory, Mail Stop 298-100, 4800 Oak Grove Drive, Pasadena, California 91109.

## References

1. R. Trebino, C. C. Hayden, A. M. Johnson, W. M. Simpson, and A. M. Levine, *Opt. Lett.* **15**, 1079 (1990).
2. V. Dominic, X. S. Yao, R. M. Pierce, and J. Feinberg, *Appl. Phys. Lett.* **56**, 521 (1990).
3. X. S. Yao, V. Dominic, and J. Feinberg, *J. Opt. Soc. Am. B* **7**, 2347 (1990).
4. L. H. Acioli, M. Ulman, E. P. Ippen, and J. G. Fujimoto, *Opt. Lett.* **16**, 1984 (1991).
5. E. D. Treacy, *IEEE J. Quantum Electron.* **QE-5**, 454 (1969).
6. A. L. Smirl, K. Bohnert, G. C. Valley, R. A. Mullen, and T. F. Boggess, *J. Opt. Soc. Am. B* **6**, 606 (1989).
7. E. P. Ippen and C. V. Shank, *Appl. Phys. Lett.* **27**, 488 (1975).
8. E. W. Van Stryland, *Opt. Commun.* **31**, 93 (1979).
9. R. Trebino, E. K. Gustafson, and A. E. Siegman, *J. Opt. Soc. Am. B* **3**, 1295 (1986).
10. M. Born and E. Wolf, *Principles of Optics*, 6th ed. (Pergamon, Oxford, 1980), Chap. 10, pp. 491–518.
11. X. S. Yao and J. Feinberg, *Appl. Phys. Lett.* **62**, 811 (1993).
12. X. S. Yao, Ph.D. dissertation (University of Southern California, Los Angeles, Calif., 1992).
13. A. M. Weiner, J. P. Heritage, and E. M. Kirschner, *J. Opt. Soc. Am. B* **5**, 1563 (1988).